Mix, A.C., Tiedemann, R., Blum, P., et al., 2003
Proceedings of the Ocean Drilling Program, Initial Reports Volume 202

10. Site 1239[1]

Shipboard Scientific Party[2]

INTRODUCTION

Site 1239 (proposed Site CAR-1C) is located at 0°40.32′S, 82°4.86′W, ~120 km off the coast of Ecuador (Fig. F1). Near the eastern crest of Carnegie Ridge at 1414 m water depth, the site is situated roughly in the middle of a bench that slopes gently to the south (Fig. F2). Just to the east, Carnegie Ridge slopes downward into the Peru-Chile Trench, where subduction is consuming the volcanic seamounts produced by the Galapagos hotspot. Basement at Site 1239 likely consists of basalt formed at the Galapagos hotspot ~11–13 m.y. ago (Lonsdale and Klitgord, 1978). From the southwest, where Site 1238 is found on a sedimented ramp near 2200 m depth, the seafloor steps up a basement scarp of Carnegie Ridge to another gently sloping platform on which Site 1239 is located. Farther to the north, the basement rises again to a series of partially eroded seamounts with peaks from 500 to 1000 m below sea level. These bathymetric highs may have been above sea level early in their history as part of an archipelago similar to the modern Galapagos Islands.

The region of Site 1239 is heavily sedimented, with likely pelagic sediments of variable thickness covering rough basement topography. Seismic profiles (Fig. F3) reveal stratified reflective sediments that drape the underlying bathymetry and fill basement lows. Dominant sediments in the region are foraminifer-bearing diatom nannofossil ooze, with some intervals of diatom ooze (Kemp et al., 1995) and occasional ash layers (Ledbetter, 1985). The steep basaltic flanks of Carnegie Ridge are mostly bare rock, so some downslope transport of sediment is possible (Fig. F2).

A tectonic backtrack path on the Nazca plate (Pisias et al., 1995) moves Site 1239 about 600 km westward and slightly to the south relative to a fixed South America (and probably to shallower depths, which would account for the possible erosion features on the volcanic highs)

F1. Sites 1238–1242 and regional bathymetry, p. 26.

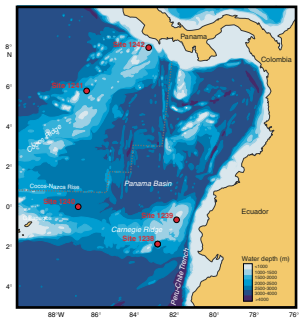

F2. High-resolution swath bathymetry, p. 27.

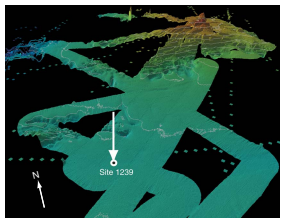

F3. Seismic profile at Site 1239, p. 28.

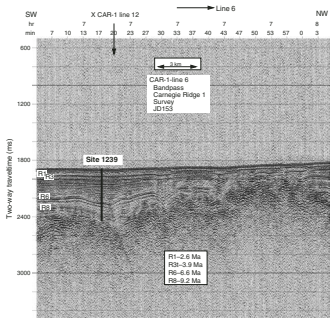

[1]Examples of how to reference the whole or part of this volume.
[2]Shipboard Scientific Party addresses.

Ms 202IR-110

(Fig. F2) to a position southeast of the Galapagos hotspot about 12 m.y. ago (Fig. F4).

Today, Site 1239 is situated under the eastern reaches of the equatorial cool tongue, in an open-ocean upwelling system near the equator (Fig. F5). The site is close to the equatorial front that separates cool, relatively high salinity surface waters south of the equator from the warm, low-salinity waters of Panama Basin (Strub et al., 1998). Nutrient-rich waters of the Equatorial Undercurrent (EUC) surface here and along the coast of Peru and Ecuador (Levitus et al., 1993), but nitrate and phosphate are not fully utilized by the phytoplankton in spite of high production (Fig. F6). Here, a limited supply of micronutrients such as iron, for which the EUC is a major source, may play an important role as a regulator of production (Murray et al., 1994).

Site 1239 is likely to record changes in upwelling and biological production, as well as long-term changes in upper-ocean temperature and pycnocline depth. The surface-ocean properties of the eastern equatorial Pacific are sensitive to interannual to decadal oscillations such as those of the well-known El Niño Southern Oscillations (ENSO) (Cane, 1986) as well as during the Pleistocene ice ages (Pisias and Mix, 1997; Mix et al., 1999; Lea et al., 2000; Beaufort et al., 2001).

Plate tectonic backtrack locations can be used to predict general features of oceanographic change at Site 1239, under the assumptions that overall conditions in the region remain constant and that the only change in the system is drift of the site location relative to this fixed oceanographic background (Fig. F7). In this analysis we ignore changes in the position of the continental margin through time, which may be significant in the region of northern South America and the Central American Isthmus. Sampling of modern oceanographic atlas values at the paleosite locations suggests that from 3 to 4 Ma, sea-surface temperatures at Site 1238 may have been slightly (~1°C) cooler than today. At greater ages, the site was within the core of the South Equatorial Current (SEC), where temperatures are roughly constant along the backtrack path. Salinities increase slightly at greater ages, as the site backtracks gradually away from the equator and the eastern boundary. Pycnocline depth is stable along the backtrack path, at values of 20 m. Sea-surface nutrient concentrations of silicate, phosphate, and nitrate all increase significantly from 2 to 4 Ma, likely because utilization of nutrients is greater in the equatorial band, where the EUC surfaces and supplies micronutrients such as iron. Nutrients are relatively stable on the Site 1239 backtrack path prior to 4 Ma. In contrast to nutrients, primary productivity is predicted to be highest from 4 to 6 Ma, when the site was under the modern edge of the SEC. Productivity declines gradually at greater ages as the site backtracks away from the eastern margin. In the absence of other regional changes in ocean circulation or tectonics, we would expect that biogenic sediment accumulation rates at Site 1239 would be relatively high from 4 to 6 Ma, when the site was under the modern zone of highest production, but that terrigenous sediment accumulation rates associated with continental runoff would be higher at younger ages, when the site was located closer to both the eastern boundary and the equator, although eolian sediment components may be more prevalent at greater ages, when Site 1239 backtracks across the northern edge of the Atacama dust plume (Molina-Cruz, 1977). Significant deviations from these general trends, if detected in the sediment cores, would imply changes in regional oceanographic or climatic conditions, or errors in the tectonic backtrack model.

F4. Tectonic backtrack of Site 1239, p. 29.

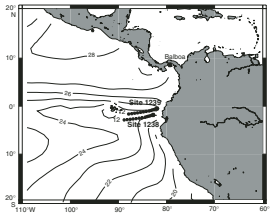

F5. Upper-ocean features off Peru and northern Chile, p. 30.

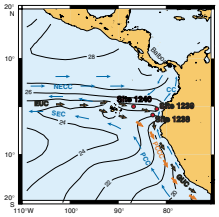

F6. Chlorophyll distributions in surface waters, p. 31.

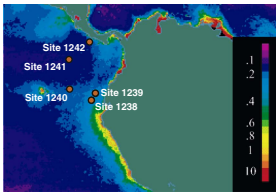

F7. Modern ocean properties at backtrack locations of Site 1239, p. 32.

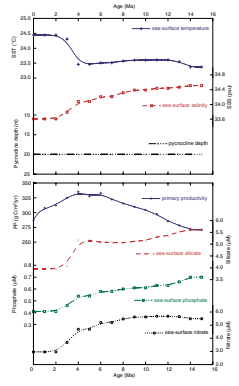

The modern water depth of Site 1239 is within the range of Pacific Central Water (PCW) south of Carnegie Ridge, but shallow enough that some mixing with remnants of Antarctic Intermediate Water (AAIW) can be detected here, especially by its relatively low salinities (Tsuchiya and Talley, 1998). AAIW is not easily detected with water column oxygen data because of the high rates of biological productivity in the region and the accompanying organic rain that consumes oxygen in the upper water column (Fig. F8). However, the comparison between a benthic foraminiferal $\delta^{13}C$ record from the top of the Carnegie Ridge (~1400 m) with records from deeper water depths (~3100 m) indicates a stronger glacial difference in nutrient concentrations than during interglacials, suggesting some change in ventilation of shallow subsurface water masses at least for the last 400 k.y. (Mix et al., 1991). North Pacific Intermediate Waters are limited to the Northern Hemisphere and are not detected in the modern water column at Site 1239.

The primary objectives at Site 1239 were to provide a continuous sedimentary sequence of Neogene age (as old as 11–12 Ma) to

1. Assess the history of near-surface water masses, including the eastern reaches of the equatorial cold tongue, upwelling, and paleoproductivity off Ecuador;
2. Monitor temporal and vertical fluctuations of subsurface water masses near 1400 m depth; and
3. Monitor changes in the occurrence and frequency of volcanic ashes, which might be associated with major uplift phases of the northern Andes.

F8. Meridional cross section of water masses, p. 33.

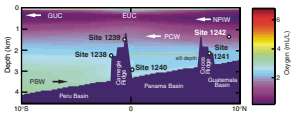

OPERATIONS

The 83-nmi transit to Site 1239 (proposed Site CAR-1C) required 7.5 hr at an average speed of 11.1 kt. The 3.5-kHz precision depth recorder (PDR) profiler was used to check the site characteristics by comparison with precruise survey data. The vessel was positioning on the site coordinates by 1945 hr on 10 May, and a beacon was deployed at 2005 hr.

Hole 1239A

After the bottom-hole assembly was made up and the drill string deployed to a depth of 1412 meters below rig floor (mbrf), the top drive was picked up and spaced out to a depth of 1420 mbrf. Hole 1239A was initiated with the advanced piston corer (APC) at 0115 hr on 11 May. The seafloor depth that was estimated by the amount of recovery of the first core was 1426.1 mbrf, 2.3 m shallower than the corrected PDR depth of 1428.4 mbrf. Piston coring advanced to 88.9 meters below seafloor (mbsf). Core barrels (Cores 10H through 12H) required drilling over to free them from the sediment. The barrels with Cores 13H through 16H (107.9–145.9 mbsf) did not need to be drilled over. The next two piston cores (17H and 18H; 145.9–164.9 mbsf) had to be drilled over. Piston coring in the hole was terminated when the last core (19H; 164.9–174.4 mbsf) did not achieve a full stroke and was recovered with a bent barrel and twisted piston rods. The APC cored 174.4 m and recovered 182.5 m (recovery = 105%).

The nonmagnetic core barrel was deployed on even-numbered cores up to and including Core 12H (Table T1). The nonmagnetic core barrel was not used after this to prevent possible damage to hardware as a con-

T1. Operations summary, Site 1239, p. 69.

sequence of the drilling-over process. The piston cores were oriented starting with Core 3H. Downhole temperature measurements were taken with the APC temperature (APCT) tool as listed in Table T1. Most of the cores were odoriferous (H_2S) and were stored on the catwalk rack after splitting to allow degassing and to reduce the smell in the laboratory stack. Headspace measurements on the cores yielded moderate amounts of methane (<60,000 ppm) and slight amounts of ethane (<20 ppm). Traces of C_3–C_5 (<3 ppm) were measured. No higher molecular weight hydrocarbon compounds were detected.

The hole was deepened with the extended core barrel (XCB) from 174.4 to 515.4 mbsf (341.0 m cored interval) with an excellent 97.5% average recovery. XCB refusal was encountered at 515.4 mbsf when the last core (55X) contacted acoustic basement. The average rate of penetration of the XCB section was ~50 m/hr. The total recovery of the hole was 515.1 m, representing 99.9% of the cored interval (Table T1).

Logging

To prepare the hole for logging, the hole was flushed with 30 bbl of sepiolite mud and then displaced with 242 bbl of 8.9-lb/gal sepiolite mud. Downhole logging operations began at 1530 hr on 12 May. The bit was placed at the logging depth of 95.5 mbsf. The triple combination (triple combo) tool string with the Lamont-Doherty Earth Observatory (LDEO) Multi-Sensor Spectral Gamma Ray Tool (MGT) on top was deployed first followed by the Formation MicroScanner (FMS)-sonic tool string. Hole 1239B was another unusually smooth hole for the Ocean Drilling Program (ODP). Data quality was excellent, similar to that from Hole 1238A. One pass with the triple combo tool string was conducted from total depth (517 mbsf) to the mudline, followed by one full pass from 517 mbsf to the bit and one repeat pass from 155 mbsf to the bit with the LDEO MGT. Two subsequent passes with the FMS-sonic tool string also reached the bottom of the hole. The hole diameter ranged from ~11.5 to 15 in, allowing good pad contact. Hole deviation increased with depth, reaching 7.5° at the bottom. Logging operations were completed by 0800 hr on 13 May, and the bit was pulled free of the seafloor at 0910 hr on 13 May.

Hole 1239B

The vessel was offset 20 m west of Hole 1239A. Prior to coring, a bottom water temperature measurement was obtained with the APCT tool with the bit positioned just above the seafloor. From this and the downhole temperatures measured in Hole 1239A, a temperature gradient of 9.4°C/100 m was calculated. To obtain the desired stratigraphic overlap with the first hole, the bit was then placed at 1423.0 mbrf and Hole 1239B was initiated with the APC at 1055 hr. The seafloor depth calculated from the recovery of the first core was 1424.7 mbrf. Piston coring combined with a 2-m drilled interval (102.8–104.8 mbsf) deepened the hole to 171.3 mbsf. The cored interval was 169.3 m with 177.34 m recovered (recovery = 104.7%).

The nonmagnetic core barrel was deployed on odd-numbered cores up to and including Core 15H. Three core barrels were drilled over in this hole (Cores 16H, 17H, and 18H). The cores were oriented starting with Core 3H.

XCB operations extended the total depth of this hole to 398.7 mbsf. The XCB cored 227.4 m with an average recovery of 101.2%. The total

cored interval in Hole 1239B was 396.7 m, with 407.4 m recovered (recovery = 102.7%) (Table T1). The bit was pulled free of the seafloor at 1315 hr on 14 May.

Hole 1239C

The vessel was moved 20 m west of Hole 1239B. Hole 1239C was initiated with the APC at 1420 hr on 14 May. The bit was positioned at a depth of 1426.0 mbrf or 1.3 mbsf above the calculated mudline depth of Hole 1239B (1424.7 mbrf). Piston coring deepened the hole to 117.3 mbsf to ensure complete stratigraphic recovery to a depth of 170 mbsf. Two intervals were drilled to maintain the proper overlap with the data from the previous two holes (0.0–1.3 and 39.3–41.3 mbsf). The cored interval was 114.0 m, with 119.7 m recovered (Table T1). The nonmagnetic core barrel was deployed on even-numbered cores. No core barrels were drilled over. Cores were oriented starting with Core 3H.

The total cored interval at Site 1239 was 1026.1 m, with 1042.1 m recovered, representing an average recovery of 101.6%. The vessel was secured and departed for Site 1240 at 0218 hr on 15 May.

COMPOSITE SECTION

We built a meters composite depth (mcd) scale to Section 202-1239A-54X-7, 40 cm (0.00–556.82 mcd) and a splice (as defined in "Composite Section," p. 4, in the "Explanatory Notes" chapter) that documents complete recovery for the upper 188.85 mcd. The splice ranges from the top of Core 202-1239A-1H to the bottom of Section 202-1239A-19H-7 (0.00–188.85 mcd) (see Tables T2, T3). All APC cores can be correlated to the splice at Site 1239.

The mcd scale and the splice are based on the correlation of whole-core Oregon State University Fast Track magnetic susceptibility (OSUS-MS) measurements collected at 5-cm intervals (Fig. F9; Tables T4, T5, T6). Tie points (Table T3) were used to construct a representative spliced record for multisensor track magnetic susceptibility (MST-MS), gamma ray attenuation (GRA) bulk density, and natural gamma radiation (NGR) data (Fig. F10), and color reflectance (L*, a*, and b*) data (Fig. F11). Magnetic susceptibility was the most useful tool for stratigraphic correlation at Site 1239.

We assumed that the uppermost sediment (the "mudline") in Core 202-1239A-1H was the sediment/water interface. Core 202-1239A-1H, the "anchor" in the composite depth scale, is the only core with depths that are the same on the mbsf and mcd scales. From this anchor, we worked downhole, correlating records on a core-by-core basis. Core 202-1239B-1H was assigned a negative offset because the uppermost few centimeters of sediment in this core has unrealistically high magnetic susceptibility that indicates possible contamination. Core 202-1239C-1H, even though it has a –0.95 m negative offset relative to Core 202-1239A-1H, is not the anchor in the splice because Cores 202-1239A-1H and 202-1239B-1H both clearly recover sediment from above the top of Core 202-1239C-1H. This negative offset is related to the general uncertainty in drillers depth estimates.

The mcd scale is on average 8% longer than the mbsf scale (Fig. F12). Given that the growth factor of 1.08 in the APC section was inferred to be constant and that no obvious lithologic changes occur in the recovered section, we placed the XCB cores on an approximate mcd scale us-

T2. Composite depth scale, p. 71.

T3. Splice tie points, p. 73.

F9. Magnetic susceptibility vs. mcd, p. 34.

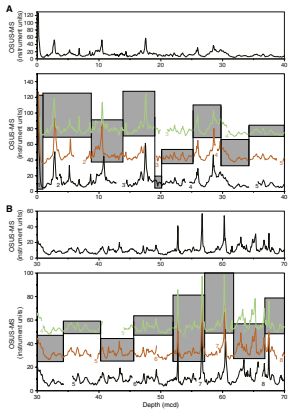

T4. OSUS-MS measurements, Hole 1239A, p. 74.

T5. OSUS-MS measurements, Hole 1239B, p. 75.

T6. OSUS-MS measurements, Hole 1239C, p. 76.

F10. Spliced records of NGR, GRA density, and MS, p. 41.

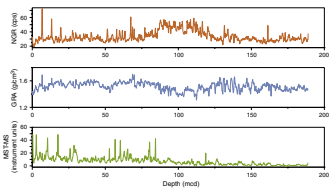

F11. Spliced records of L*, a*, and b*, p. 42.

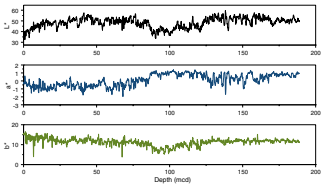

ing the observed expansion in the APC section. Thus, the 1.08% growth factor was applied to the XCB cores from Site 1239 (Fig. F12).

To facilitate the calculation of mass accumulation rates (MARs), we provide corrected meters composite depth (cmcd) in Table T2 and in Table T3 for depths within the splice.

Downhole logging operations at Site 1239 produced records of borehole density and NGR that could be correlated to GRA density and NGR measurements in sediments from Hole 1239A (Fig. F13). An estimated log depth (eld) scale was produced using these correlations (see "Core-Log Integration," p. 6, in "Composite Section" in the "Explanatory Notes" chapter). This eld scale accounts for differential stretching and squeezing within cores as well as for the gaps between cores and is the most accurate depth scale for sediments below the spliced section. The Site 1239 eld file (see the "Supplementary Material" contents list) allows the application of the eld depth scale to sample depths in either the mbsf or mcd scale using the "Sagan" software package available from the Borehole Research Group at LDEO.

LITHOSTRATIGRAPHY

A 512.3-m-thick (557.5 mcd) sediment sequence dating back to the middle Miocene (~14.6 Ma) was recovered from three holes at Site 1239. One lithologic unit (Unit I) was defined at Site 1239 (Fig. F14). The recovered sediments are dominated by foraminifer (0 to ~25 mcd) and nannofossil oozes with varying amounts of clay, diatoms, and micrite. Biogenic constituents vary in abundance and consist primarily of nannofossils with less abundant diatoms, foraminifers, radiolarians, silicoflagellates, and spicules (Fig. F15). Siliciclastic components include clay minerals and lesser amounts of feldspars and biotite. The sediments contain varying amounts of authigenic pyrite and micrite throughout. Interbedded minor lithologies include volcanic ash layers and mafic sand layers.

The lithologies at this site reflect a moderate- to high-productivity pelagic setting. Evidence from total organic carbon (TOC) (in weight percent) measurements, mass accumulation estimates, and the increased occurrence of organic pigments indicates an interval of relatively high productivity from ~1.8 to 3 Ma (90–200 mcd) as compared to the Pleistocene interval. Magnetic susceptibility remains relatively constant and low below ~150 mcd, indicating minimal terrigenous input. A gradual increase accompanied by higher-amplitude variability in the uppermost ~150 mcd may be linked to the intensification of Pliocene–Pleistocene glaciations. Rhythmic meter-scale light/dark color changes are present throughout and are interpreted to reflect changes in the relative proportions of biogenic components ($CaCO_3$ vs. biogenic opal) possibly as a response to orbital climate forcing. Twenty-four ash layers are present within the sequence.

Description of Lithologic Unit

Unit I

Intervals: Cores 202-1239A-1H through 55X; Cores 202-1239B-1H through 42X; and Cores 202-1239C-1H through 12H
Depths: 0–557.5 mcd; Hole 1239A: 0.0–512.3 mbsf; Hole 1239B: 0.0–398.1 mbsf; and Hole 1239C: 1.30–117.7 mbsf

F12. A comparison of the mbsf and mcd scales, p. 43.

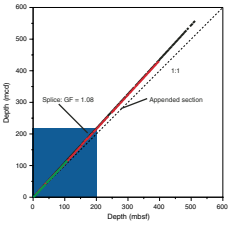

F13. A comparison of core and log gamma ray and density, p. 44.

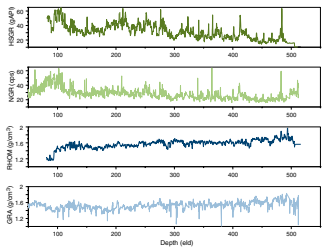

F14. Lithostratigraphic summary, p. 45.

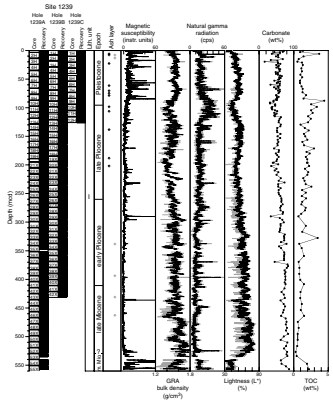

F15. Major components in smear slides, p. 46.

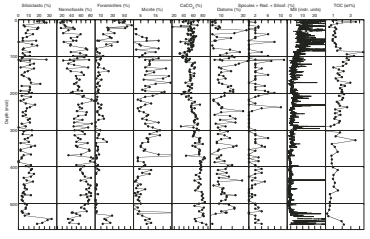

Age: Pleistocene to middle Miocene (~0–14.6 Ma) (see **"Biostratigraphy,"** p. 10)

We distinguished one lithologic unit at Site 1239 (Unit I) (Table **T7;** Fig. **F14**) on the basis of visual core description, smear slide analysis, thin section examination, color reflectance, and NGR, moisture and density (MAD), and GRA bulk density measurements. The dominant lithology defining Unit I is nannofossil ooze with varying diatom and clay abundance (i.e., clay-bearing nannofossil ooze and clay diatom-bearing nannofossil ooze). Transitions between nannofossil ooze and diatom-bearing nannofossil ooze are present on a meter to decimeter scale. Foraminifer ooze is present in the upper 24.6 mcd. Minor components include radiolarians, silicoflagellates, micrite, and pyrite. Sediment colors include light olive gray, olive gray, dark olive gray, olive, and olive brown in the upper 230 mcd and pale olive, light gray, and pale yellow below that interval. High-frequency (meter scale) dark and light color variability is present throughout the sedimentary sequence, reflecting the transitions between light nannofossil-rich and dark diatom-rich sediment. These meter-scale color changes are all subtle and gradational. Similarly, physical properties measurements within these intervals show parallel meter-scale changes. Bioturbation is common to pervasive throughout the sediments recovered at Site 1239 (Fig. **F16**). Mottles, *Zoophycos* traces, and horizontal and vertical burrows are commonly surrounded by diagenetic halos. Burrow fill is often coarser or finer than the surrounding material, suggesting some centimeter-scale sediment redistribution. Hydrogen sulfide gas was released when the cores were split. Small horizontal fissures caused by degassing are present throughout the three holes. Several ash layers are present throughout the unit (Table **T8;** Fig. **F14**).

Nannofossil abundance increases from the top (~20%) to ~50%–70% near 100 mcd. Farther downhole, nannofossil contents fluctuate, with average values gradually increasing downhole to values of ~80% at ~500 mcd. Below that level, nannofossils decrease again toward the base of the sequence (Fig. **F15**). Average calcium carbonate concentrations gradually increase below 100 mcd, reflecting the observed trend in nannofossils (Fig. **F15**). Foraminifers are most abundant in the upper ~85 mcd, approaching maximum values of >60%. Below ~85 mcd, foraminifer abundance remains between 0% and 10% down to 500 mcd. Diatom abundances are variable and range from ~0% to 30% throughout. Diatoms are absent or rare below 530 mcd. The foraminifer and nannofossil oozes in Unit I contain variable minor amounts of radiolarians, silicoflagellates, spicules, micrite, and siliciclastic components. The combined abundance of radiolarians, spicules, and silicoflagellates are quite variable throughout the sequence with pronounced minima at ~85 mcd and from 250 to 290 mcd (Fig. **F15**).

Clay minerals constitute ~90%–100% of the siliciclastic component with minor contributions from feldspars, amphiboles, micas, and pyroxenes. Siliciclastic content is highly variable with low mean values (~10%) throughout (Fig. **F15**). In the top ~10 mcd and bottom ~50 mcd of the sequence, siliciclastics are more abundant.

Unit I also contains the authigenic components micrite and pyrite. Micrite is absent to rare in the upper 40 mcd, increases to ~25% at 180 mcd, and then fluctuates between 0% and 15% downhole. Micrite content is highly variable between 40 and 400 mcd. Micrite-rich intervals are often associated with lower nannofossil abundance (Fig. **F15**). From 400 to 500 mcd, the micrite content decreases gradually, and below 510

T7. Lithologic Unit I, p. 77.

F16. Bioturbated intervals with mottles, burrows, and *Zoophycos,* p. 47.

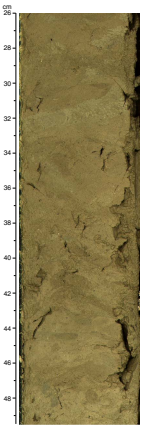

T8. Ash layers, p. 78.

mcd it increases toward the base of the sequence. Pyrite is finely dispersed (0%–2%) throughout and concentrated as framboids in biogenic material such as diatoms and foraminifers. Black sand-sized mafic grains are sparse in the sediments below ~400 mcd, increasing in size and abundance downhole. Below 519 mcd (Cores 202-1239A-52X through 55X), several black mafic sand layers and lithified black sand patches are present.

Twenty-four ash layers are present in Unit I, thirteen of which correlate among Holes 1239A, 1239B, and 1239C (Table T8). The ash layers range in thickness from 1 to 18 cm and are typically light to dark gray with sharp or bioturbated basal contacts and gradational, often bioturbated, upper contacts (Fig. F17). The ash is composed mainly of silt- to sand-sized clear volcanic glass shards, including unaltered platey and vesicular glass, and, less commonly, palagonite. The most common associated mineralogical components include feldspars, biotite, hornblende, pyroxenes, and pyrite.

All physical properties at Site 1239 show depth variability patterns that are generally similar to the ones observed at Site 1238 (Fig. F14) (see "Lithostratigraphy," p. 6, in the "Site 1238" chapter). Magnetic susceptibility is moderately high with superimposed high-amplitude variability in the top 100 mcd and decreases to low values (generally <15 instrument units) between 100 and 150 mcd. From 150 to 300 mcd, the values are generally low, with pronounced spikes interspersed throughout. Below 300 mcd, a further decrease to <10 instrument units occurs. From 520 to 558 mcd, magnetic susceptibility increases again to moderately high values (10–80 instrument units).

GRA and MAD bulk density correlate well (r^2 = 0.8) (Fig. F18). Bulk density increases in the upper ~25 m of the sequence related to compaction and dewatering (Fig. F18). Although bulk density seems to vary with depth similar to carbonate content, the correlation between the two is poor (r^2 = 0.3) (Fig. F18).

In the a*-b* color space, all color measurements at Site 1239 plot in the "yellow" domain (Fig. F19). Although L* seems to vary with depth similar to the carbonate content, the correlation between the two is weak (r^2 < 0.5). Predictive relationships between reflectance and carbonate and TOC via a multiple linear regression are also weak (i.e., r^2 = ~0.6 for both components), reflecting the complexity of the sediment matrix that includes opaline silica and other chromophores.

Organic pigment absorption features are detectable at 410, 510, 560, and 650 nm in reflectance spectra measured in sediment at Site 1239 (Fig. F20). The strongest absorption feature at 650 nm that persists throughout the sediment column is due to chlorins (i.e., chlorophyll-related pigments) and is most pronounced between ~90 and 230 mcd.

Interpretation and Depositional History

Site 1239 is primarily characterized by rapidly (~5–10 cm/k.y.) accumulating pelagic foraminifer and nannofossil oozes. Sites 1238 and 1239 are both located in a similar setting in which changes in the supply of nutrients in the active equatorial upwelling zone are reflected in the varying amounts of siliceous or calcareous primary producers throughout their sequences. The largest shifts in microfossils at Site 1239 roughly coincides with the Pliocene/Pleistocene boundary (~100 mcd), where foraminifers become more abundant and nannofossil abundance decreases. Diatoms also generally becomes less abundant above this horizon. These changes take place within the context of a

F17. Ash layers, p. 48.

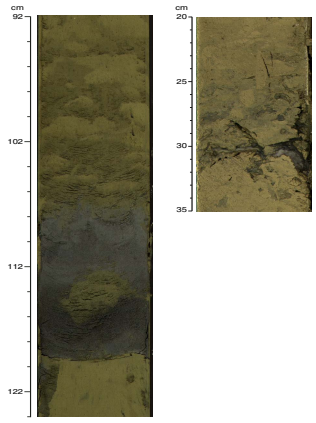

F18. Physical properties measurements, p. 49.

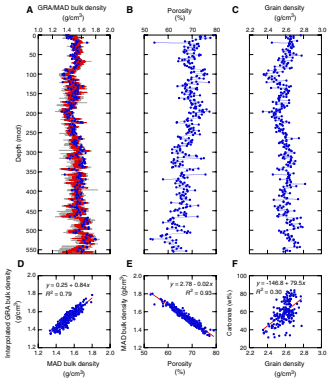

F19. Color measurements, p. 50.

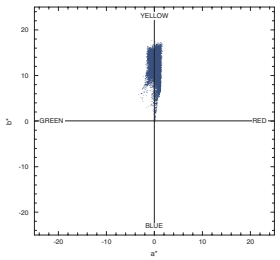

F20. Reflectance data, p. 51.

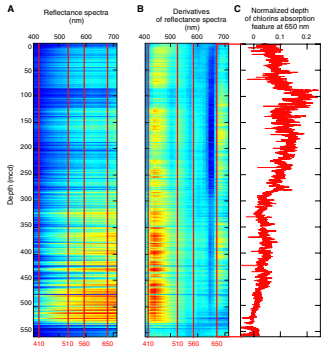

setting that remained relatively productive. The increase in TOC from 550 to 90 mcd (upper Miocene–lower Pleistocene) parallels a similar increase in U (see "Downhole Measurements," p. 20), both of which can be indicators of either a gradual increase in productivity with time or a gradual increase in degradation of organic matter (see "Geochemistry," p. 16). Nevertheless, the increased presence of chlorins, higher MARs (see "Age Model and Mass Accumulation Rates," p. 22), and a maximum in TOC from ~90 to 200 mcd suggest high productivity within this interval (~1.8–3 Ma) compared to the Pleistocene.

The cyclic pattern of light/dark color changes observed throughout Unit I was also observed at Site 1238. Preliminary spectral analyses of the magnetic susceptibility, GRA density, and lightness measurements between 0.0 and 58.2 mcd of the sequence at Site 1238 have significant concentration of power within orbital frequency bands associated with eccentricity, obliquity, and precession.

The observed susceptibility values in the upper 150 mcd of Unit I are most easily explained by generally higher, more variable input of fine-grained magnetic minerals associated with a terrigenous component because small changes in terrigenous content would be proportionally significant in the biogenically dominated sediment of Unit I. The increase in magnetic susceptibility is paralleled by a decrease in sedimentation rate (see "Biostratigraphy," p. 10), possibly associated with a decrease in biogenic components. Hence, less dilution may result in higher siliciclastic concentrations and thus in higher magnetic susceptibility values. On the other hand, diagenetic dissolution of magnetic minerals might have contributed to the low magnetic susceptibility values farther downhole (see discussion in "Lithostratigraphy," p. 6, in the "Site 1238" chapter). Variability in NGR is probably controlled by U concentration in sediments (see "Downhole Measurements," p. 20); the average counts are higher than those at Site 1238. Grain densities are very similar at Sites 1238 and 1239, but average bulk density is higher at Site 1239, probably as a result of lower concentrations of biogenic silica. However, owing to their increased biogenic silica content (e.g., Silva et al., 1976), both Sites 1238 and 1239 have significantly higher porosities than the more southern Sites 1236 and 1237. Lithification-related general decreases in porosity and associated increases in bulk density are apparent in the lower half of the sequence (Fig. F18).

Volcanic ash deposition at Site 1239 began in the late Miocene to early Pliocene, increasing in frequency between the middle–late Pliocene and early Pleistocene. The accessory mineral composition of ashes at Site 1239 suggests an andesitic volcanic source, most likely from explosive eruptions in northern South America, Central America, and southern Mexico (Ledbetter, 1985). Based on sedimentation rate estimates of ~5 to 6 cm/k.y. (late Pleistocene) for Site 1239 (see "Age Model and Mass Accumulation Rates," p. 22), ash layer L (230 ka) (Bowles et al., 1973; Ninkovich and Shackleton, 1975) is present at 13.31 mcd in this sequence (Table T8). Based on its distribution in eastern tropical Pacific marine sediments, Ninkovich and Shackleton (1975) hypothesized the existence of a volcanic source in northern South America for this ash layer. Ash layer L is observed in sediment from Holes 1239B and 1239C (the corresponding interval in Hole 1239A spans a core gap). Unlike at Site 1238, where ash layer L was consistently 15–20 cm thick, ash layer L at Site 1239 is between 5 and 8 cm thick.

The shallowest occurrence of mafic sand-sized grains at Site 1239 is at ~400 mcd (~5 Ma). The downhole increase in abundance of these

grains below 400 mcd and the presence of lithified sand layers toward the base of the sequence are consistent with a paleoposition of Site 1239 that is closer to the Galapagos hotspot than the modern position of Site 1239.

A 6.8-m.y. hiatus is identified between Sections 202-1239A-51X-CC (7.8 Ma) and 52X-CC (14.6 Ma) based on biostratigraphic datums (see "Biostratigraphy," p. 10). Although less well defined, a similar hiatus was found at Site 1238, spanning >12 to ~8 Ma. However, a major difference between the two sites concerns the formation of chalk and chert. Despite penetrating 512 m at Site 1239, no chalk or chert layers were observed, even though they were recovered at a shallower depth at Site 1238 (430 mcd). Pore water geochemical evidence suggests that the lack of chert formation at Site 1239 is most likely related to its lower thermal gradient relative to that at Site 1238 (see "Geochemistry," p. 16).

BIOSTRATIGRAPHY

The sedimentary sequence recovered from the three holes cored at Site 1239 consists of a 560-m-thick interval of Quaternary–middle Miocene sediments. A relatively well constrained biostratigraphy is provided by all three microfossil groups (Table T9). The biostratigraphic sequence is similar to that at Site 1238, except that a major hiatus was clearly identified by three different microfossil groups between Samples 202-1239A-51X-CC (519.3 mcd) and 52X-CC (527.7 mcd) (Fig. F37). The time interval of the hiatus is tentatively estimated by the calcareous nannofossil biostratigraphy as ~7.8–13.6 Ma. The presence of the middle Miocene planktonic foraminifer index species *Globorotalia peripheroronda* and *Globorotalia praemenardii* in Sample 202-1239X-55X-CC suggests that the basal age at Site 1239 is between 14.6 and 14.9 Ma.

The abundance and preservation of calcareous microfossils at Site 1239 are similar to those at Site 1238 (Fig. F21). Calcareous nannofossils are abundant and well preserved within the top ~100 mcd, but both abundance and preservation decline slightly below this horizon. Planktonic foraminifers are common within the top ~100 mcd but decrease rapidly at greater depths. Benthic foraminifers, which are common to abundant below ~100 mcd, generally indicate high carbon fluxes at the seafloor, probably derived at this location from upwelling driven productivity. Diatoms are also present throughout the sedimentary section, although their abundance is relatively low in the Holocene–mid-Pleistocene and lower Pliocene–uppermost Miocene intervals in comparison to Site 1238.

Calcareous Nannofossils

As at Site 1238, Site 1239 yielded abundant and well to moderately preserved calcareous nannofossils in all samples examined (Table T10). Because of the high abundance of siliceous microfossils, which indicates eutrophic conditions in most of the sequence, some traditional index nannofossil species, particularly some discoaster and amaurolith species, are rare or absent. Persistent reworking of nannofossils in the upper upper Miocene–lower Pliocene is suggested by the presence of older species in demonstrably younger sediments. This hampered the stratigraphic resolution to some extent. Nevertheless, a moderate-resolution nannofossil biostratigraphy has been established, which sug-

T9. Age-depth control points, p. 79.

F21. Calcareous nannofossils and foraminifer abundance, Hole 1239A, p. 52.

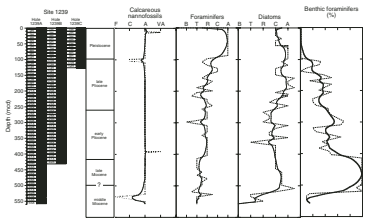

T10. Distribution of calcareous nannofossils, p. 81.

gests a relatively complete section for the top ~450 mcd (0–8 Ma), a major hiatus encompassing the ~8- to 13-Ma interval, and a basal sediment age of ~15 Ma at the site.

Virtually, all the well-known Pleistocene nannofossil events have been located within an uncertainty of about 1.5 m, allowing a relatively high resolution biostratigraphy for the Pleistocene. The nannofossil events recognized are the beginning of the acme of *Emiliania huxleyi* (0.08 Ma) between Samples 202-1239A-1H-2, 75 cm (2.26 mcd), and 1H-3, 40 cm (2.92 mcd); the first occurrence (FO) of *E. huxleyi* (0.26 Ma) between Samples 2H-3, 75 cm (7.3 mcd), and 2H-4, 75 cm (8.8 mcd); the last occurrence (LO) of *Pseudoemiliania lacunosa* (0.46 Ma) between Samples 3H-1, 75 cm (15.05 mcd), and 3H-2, 75 cm (16.56 mcd); the LO of *Reticulofenestra asanoi* (0.88 Ma) between Samples 5H-1, 75 cm (36.4 mcd), and 5H-2, 75 cm (37.9 mcd); the reentry of medium *Gephyrocapsa* spp. (1.02 Ma) between Samples 6H-5, 75 cm (52.77 mcd), and 6H-6, 75 cm (54.27 mcd); the FO of *R. asanoi* (1.08 Ma) between Samples 6H-7, 40 cm (55.42 mcd), and 6H-CC, 35 cm (56.1 mcd); the LO of large *Gephyrocapsa* spp. (1.24 Ma) between Samples 7H-4, 75 cm (61.4 mcd), and 7H-5, 75 cm (62.9 mcd); the FO of large *Gephyrocapsa* spp. (1.45 Ma) between Samples 8H-CC, 31 cm (76.41 mcd), and 9H-1, 75 cm (77.95 mcd); the LO of *Calcidiscus macintyrei* (1.59 Ma) between Samples 9H-7, 40 cm (86.66 mcd), and 9H-CC (87.26 mcd); and the FO of medium *Gephyrocapsa* spp. (1.67 Ma) between Samples 9H-CC (87.26 mcd), and 10H-1, 75 cm (87.95 mcd).

The youngest Pliocene nannofossil datum, the LO of *Discoaster brouweri* (1.96 Ma), placed between Samples 202-1239A-11H-2, 75 cm (100.1 mcd), and 11H-3, 75 cm (101.6 mcd), may not be very reliable because of some reworking of nannofossils in this interval. The next three older discoaster datums of the late Pliocene (the LOs of *Discoaster pentaradiatus, Discoaster surculus,* and *Discoaster tamalis*) were not recognized because of the rare abundance or absence of those species. Rare to few *Reticulofenestra pseudoumbilicus* and *Sphenolithus* spp. were found from Cores 202-1239A-16H through 29X, but considerable stratigraphic overlap occurs with *P. lacunosa,* indicating that all these specimens of *R. pseudoumbilicus* and *Sphenolithus* spp. are reworked. The first common occurrences of the two taxa were found in Sample 202-1239A-30X-CC, 1 cm (298 mcd), downhole, and thus, the LOs of *Sphenolithus* spp. (3.65 Ma) and *R. pseudoumbilicus* (3.8 Ma) are placed between Samples 29X-CC (288.09 mcd) and 30X-CC, 1 cm (297.99 mcd).

As at Site 1238, the youngest Miocene datum, the LO of *Discoaster quinqueramus* (5.56 Ma), could not be used at this site because of persistent reworking of nannofossils in the upper upper Miocene (Table **T10**). However, two first occurrence datums have been reasonably well determined in this interval: the FO of *Ceratolithus cristatus* (5.04 Ma) between Samples 202-1239A-38X-2, 75 cm (375.3 mcd), and 38X-3, 75 cm (376.8 mcd), and the FO of *Ceratolithus armatus* (= *Ceratolithus acutus*) (5.34 Ma) between Samples 41X-CC (414.4 mcd) and 42X-1, 75 cm (415.8 mcd).

A usually reliable late Miocene datum, the top of the *R. pseudoumbilicus* (>7 µm) absence interval (6.8 Ma), is located between Samples 202-1239A-47X-6, 75 cm (475.7 mcd), and 47X-7, 40 cm (476.8 mcd). A major hiatus was identified between Samples 202-1239A-51X-CC (519.3 mcd) and 52X-CC (527.7 mcd), as the upper sample contains *D. surculus* and *D. loeblichii* but no *R. pseudoumbilicus* and thus has an age of 6.8–7.8 Ma, whereas the lower sample contains *Sphenolithus heteromorphus* and *Cyclicargolithus floridanus* and thus has an age of 13.6–18.2 Ma.

The next several samples to the deepest sample from the hole—Sample 202-1239A-55X-CC (557 mcd)—all contain the same assemblage with the presence of *S. heteromorphus* and thus all have the same age range of 13.6–18.2 Ma.

Planktonic Foraminifers

Planktonic foraminifers are abundant and well preserved in sediment from the upper part of Hole 1239A (mudline to Sample 202-1239A-10H-CC; 0–97.2 mcd). Between Cores 202-1239A-11H and 40X (107.7–404.0 mcd), abundance and preservation vary markedly, and the relative proportion of radiolarians and benthic foraminifers in the residue generally increases downhole (Table **T11;** Fig. **F21**). Between Cores 202-1239A-41X and 51X (414.4–519.3 mcd), radiolarians are generally abundant, and planktonic foraminifers are extremely rare, representing ~1% or less of total foraminifers. Abundance increases slightly in the lowermost samples (Cores 202-1239A-52X through 55X; 527.7–557.0 mcd); however, preservation deteriorates significantly within this interval and recrystallized overgrowths frequently obscure test features.

T11. Distribution of planktonic foraminifers, p. 84.

Diversity is overall quite low, and assemblages tend to be dominated by upwelling taxa such as *Neogloboquadrina dutertrei* or *Neogloboquadrina pachyderma*. Standard marker species are present in samples from throughout the upper part of Hole 1239A and can be used to establish a preliminary biostratigraphy for the Pleistocene to upper Pliocene interval (Cores 202-1239A-1H through 12H; 3.4–13.0 mcd). However, few datums are available between Cores 202-1239A-13H and 51X (128.7–519.3 mcd) to interpret and constrain the biostratigraphy of lower Pliocene to upper Miocene sediments. The foraminiferal assemblage within this interval contains a significant proportion of blackened tests with mud infills that indicate some reworking. The presence of middle Miocene index species in the lowermost samples (Samples 202-1239A-52X-CC through 55X-CC (527.7–557.0 mcd) indicates a major hiatus between Samples 51X-CC and 52X-CC (519.3–527.7 mcd). An age between 14.6 and 14.9 Ma is attributed to the base of Hole 1239A.

The well-preserved Pleistocene to late Pliocene planktonic foraminiferal assemblage includes *Globigerina bulloides, Globigerina quinqueloba, Globigerinita glutinata, Globigerinoides ruber, Globorotalia menardii, Globorotalia scitula, Globorotalia tumida, N. dutertrei, N. pachyderma, Orbulina universa,* and *Sphaeroidinella dehiscens*. The LO of *G. ruber* pink (0.12 Ma) is placed between Samples 202-1239A-1H-CC and 2H-CC (3.4–13.0 mcd), and the overlying section can be assigned to the upper Pleistocene Subzone Pt1b of Berggren et al. (1995) (Fig. **F12,** p. 63, in the **"Explanatory Notes"** chapter). The FO of *G. ruber* pink (0.40 Ma) is recognized between Samples 202-1239A-2H-CC and 3H-CC (13.0–24.3 mcd).

The boundary between upper Pleistocene Subzone Pt1b and lower Pleistocene Subzone Pt1a is marked by the LO of *Globorotalia tosaensis* (0.65 Ma; Zone Pl5), which can be placed between Samples 202-1239A-4H-CC and 5H-CC (34.6–45.7 mcd). The LO of representatives of the benthic genus *Stilostomella,* which occurred at ~0.65 Ma (Hayward, 2001), provides an additional datum to approximate this boundary between Samples 202-1239A-4H-CC and 5H-CC (34.6–45.7 mcd). The LO of *Neogloboquadrina acostaensis* (1.58 Ma), which can be identified between Samples 202-1239A-8H-CC and 9H-CC (76.4–87.3 mcd), indicates Subzone Pt1a.

The Pliocene/Pleistocene boundary could not be recognized, due to the absence of the standard zonal markers. However, the LO of *Globorotalia exilis* (2.15 Ma) between Samples 202-1239A-11H-CC and 12H-CC (107.7–118.3 mcd) indicates upper Pliocene Zone Pl6, and the LO of *Globorotalia limbata* (2.38 Ma) between Samples 11H-CC and 12H-CC (107.7–118.3 mcd) identifies Zone Pl5. The LO of *Globorotalia margaritae* (3.58 Ma) between Samples 202-1239A-20X-CC and 21X-CC (199.4–205.0 mcd) marks the base of upper Pliocene Zone Pl3. Two useful markers for lower Pliocene Zone Pl2 are the LO of *Pulleniatina primalis* (3.65 Ma) and the LO of *G. margaritae* common (3.96 Ma) between Samples 202-1239A-26H-CC and 27H-CC (257.3-267.4 mcd) and Samples 27H-CC and 28H-CC (267.4–277.8 mcd), respectively. The FO of *Globorotalia puncticulata* (4.50 Ma), identified between Samples 202-1239A-34X-CC and 35X-CC (340.9–347.6 mcd), and the LO of *Globoquadrina dehiscens* (5.49 Ma), placed between Samples 39X-CC and 40X-CC (391.3–404.0 mcd), indicate Subzones Pl1b and Pl1a, respectively.

The Pliocene/Miocene boundary is marked by the FO of *G. tumida* (5.82 Ma) between Samples 202-1239A-40X-CC and 41X-CC. The FO of *G. margaritae* (6.09 Ma), which corresponds to uppermost Miocene Zone M14, can be placed between Samples 202-1239A-46H-CC and 47H-CC (466.70–477.23 mcd). The FO of *Globorotalia conglobatus* (6.20 Ma) between Samples 202-1239A-48X-CC and 49X-CC (487.7–498.2 mcd) identifies the upper Miocene Subzone M13b. Several datums provide useful age control for the lower part of Hole 1239A, indicating a major hiatus (~4 m.y.) followed by much lower sedimentation rates during the late middle Miocene. The LO and FO of *Globorotalia fohsi* s.l. (11.68 and 13.42 Ma, respectively), which occur between Samples 202-1239A-51X-CC and 52X-CC (519.29–527.69 mcd) and between Samples 52X-CC and 53X-CC (527.7–534.9 mcd), respectively, mark the base and top of middle Miocene Zone M9. The LO of *G. peripheroronda* (14.6 Ma) between Samples 202-1239A-52X-CC and 53X-CC (527.7–534.9 mcd) corresponds to Zone M7. The base of this zone is identified by the FO of *Globorotalia peripheroacuta* (14.8 Ma). This species is present in Samples 202-1239A-53X-CC and 54X-CC (534.9–549.10 mcd). However, it was not possible to ascertain its FO from the low-resolution shipboard study because of the poor preservation and scarcity of foraminifers in the samples investigated. The FO of *G. praemenardii* (14.9 Ma), present in Sample 202-1239A-55X-CC (557.0 mcd), is not determined, as it is present below the lowermost core catcher sample from Hole 1239A.

Benthic Foraminifers

The abundance and preservation of benthic foraminifers vary markedly in Hole 1239A (Fig. **F21**). The percentage of benthic foraminifers relative to total foraminifers is initially low (1% or less), and preservation is good between the mudline and Sample 202-1239A-10H-CC (0–97.2 mcd). Between Cores 202-1239A-11H and 40X (107.7–404.0 mcd), the proportion of benthic foraminifers fluctuates between 10% and 65% of the total assemblage, except in Sample 202-1239A-14H-CC, which contains ~1% benthic foraminifers. Benthic foraminifers dominate in Cores 202-1239A-41X to 51X (414.4–519.3 mcd), representing ~99% of total foraminifers. Preservation is moderate overall in the interval between Cores 202-1239A-11H and 51X. Abundance decreases (10%–15%) and preservation deteriorates in the lowermost samples

(Cores 202-1239A-52X through 55X; 527.7–557.0 mcd), where recrystallized overgrowths frequently obscure test features.

The assemblage is characterized by *Bolivina seminuda, Bulimina mexicana, Cibicidoides mundulus, Globocassidulina subglobosa, Globobulimina affinis, Globobulimina pyrula, Gyroidinoides soldanii, Laticarinina pauperata, Melonis affinis, Melonis pompilioides, Oridorsalis umbonatus, Planulina wuellerstorfi, Pleurostomella brevis, Plectofrondicularia vaughani, Pullenia bulloides, Pyrgo murrhina, Pyrgo serrata,* and *Uvigerina peregrina*. The assemblage generally contains a high proportion of *Bolivina, Bulimina, Globobulimina,* and *Uvigerina,* which are indicators for high carbon fluxes at the seafloor, probably derived at this location from upwelling-driven productivity. Preliminary shipboard study of core catcher samples revealed marked fluctuations in abundance and assemblage composition, particularly in the relative proportion of high-productivity indicators. However, it was not possible to quantify such changes on the ship or to evaluate to what extent they express variability of the upwelling system and of circulation patterns or merely reflect a preservation bias.

Diatoms

All core catcher samples from Hole 1239A were analyzed as well as smear slides of some additional layers from the split cores. In contrast to Site 1238, where diatoms were generally common to abundant, diatom abundance at Site 1239 is relatively low in the Holocene to mid-Pleistocene and lower Pliocene to uppermost Miocene (Fig. **F21;** Table **T12**). Diatom abundance decreases rapidly below Sample 202-1239A-51X-CC (519.3 mcd), and Sample 55X-CC (557.0 mcd) was barren of diatoms. Diatom assemblages observed in most samples are either dominated by *Thalassiothrix* and *Thalassionema* species or by *Azpeitia nodulifer* species. Diatoms recovered from Site 1239 represent a continuous stratigraphic interval from the Holocene *Fragilariopsis doliolus* Zone through the *Nitzschia miocenica* Zone of the late Miocene in Core 202-1239A-51X (Table **T9;** Fig. **F21**). The early middle Miocene diatom species *Crucidenticula nicobarica* has been observed, without any late Miocene diatoms, within Cores 202-1239A-52X and 54X. This observation supports the existence of a hiatus within Core 202-1239A-52X, as suggested by the calcareous nannofossil and foraminiferal biostratigraphy.

T12. Distribution of diatoms, p. 86.

The generally low abundance of some index species and the frequent reworking of older diatoms into the lower Pliocene–upper Miocene sediments compromises the stratigraphic resolution to some extent and suggests the need for much more detailed shore-based work.

The mid-Pleistocene diatom datums, including the LO of *Nitzschia reinholdii* (0.62 Ma) and the LO of *Nitzschia fossilis* (0.70 Ma), are difficult to place because of the rare and sporadic presence of these species. Reliable Pleistocene diatom datums recognized included the following: the LO of *Rhizosolenia matuyamai* (1.05 Ma) between Sample 202-1239A-5H-4, 75 cm, and 5H-6, 75 cm (40.9–43.9 mcd); the FO of *R. matuyamai* (1.18 Ma) between Samples 6H-CC and 7H-1, 75 cm (56.1–56.9 mcd); and the FO of *F. doliolus* (2.00 Ma) between Samples 10H-CC and 11H-2, 75 cm (97.2–100.0 mcd). *Rhizosolenia praebergonii* var. *robusta,* which has its LO at 1.73 Ma, was not observed within the Pleistocene section at Site 1238.

The late Pliocene diatom datums recognized are the LO of *Thalassiosira convexa* s.l. (2.41 Ma) between Samples 202-1239A-14H-3, 75 cm, and 14H-4, 75 cm (132.5–134.0 mcd); the LO of *Nitzschia jouseae* (2.77

Ma) between Samples 17H-2, 75 cm, and 17H-3, 75 cm (161.2–162.7 mcd); and the FO of *R. praebergonii* s.l. (3.17 Ma) between Samples 22X-5, 75 cm, and 22X-7, 40 cm (212.6–215.2 mcd). The FO of *T. convexa* var. *convexa* (3.81 Ma) is present between Samples 202-1239A-29X-6, 40 cm, and 29X-7, 40 cm (286.5–287.5 mcd), and the FO of *N. jouseae* (5.12 Ma) is placed between Samples 36X-4, 75 cm, and 36X-5, 75 cm (357.4–358.9 mcd).

For the late Miocene, given the observed reworking, the stratigraphic model is based mainly on FO datums, but LOs have also been considered when they are in accordance with the FO definitions and have been tentatively placed as follows: the LO of *Thalassiosira miocenica* (5.84 Ma) is between Samples 202-1139A-45X-CC and 46X-CC (456.5–466.7 mcd); the FO of *T. miocenica* (6.55 Ma) is between Samples 49X-CC and 50X-CC (498.2–508.2 mcd); the FO of *T. convexa* (6.57 Ma) is between Samples 49X-CC and 50X-CC (498.2–508.2 mcd); and the FO of *N. miocenica* (7.30 Ma) is between Samples 50X-CC and 51X-CC (508.8–519.3 mcd).

Diatom abundance decreases and preservation deteriorates between the lower Pliocene and the upper Miocene section, relative to the upper Pliocene to lower Pleistocene section.

Sample 202-1239A-51X-CC (519.3 mcd) contains a monospecific diatom assemblage dominated by *Thalassiothrix* and *Thalassiosira.* The presence of *N. cylindrica* in this sample suggests that this sample is younger than the FO of this species (8.07 Ma). Middle Miocene diatoms, such as *C. nicobarica, Thalassiosira tappanae,* and *Denticulopsis hyalina,* were observed in Cores 202-1239A-52X and 53X (~520–535 mcd). The presence of these species and the absence of *Denticulopsis simonsenii* indicate an age between 13.51 and 15.0 Ma for these samples.

PALEOMAGNETISM

Natural Remanent Magnetization

The natural remanent magnetization (NRM) of archive-half sections from Holes 1239A, 1239B, and 1239C were initially measured then remeasured after alternating-field (AF) demagnetization at selected levels. XCB cores from Hole 1239B were stored as whole rounds without paleomagnetic measurements. Sections within Cores 202-1239A-1H through 6H and 202-1239B-1H through 5H were then AF demagnetized at peak alternating fields of 20 and 25 mT and measured. A few sections from Cores 202-1239A-6H and 7H were demagnetized at a peak AF of 60 mT to further evaluate the strength of the drilling overprint. Archive-half sections from Cores 202-1239A-7H through 55X, 202-1239B-6H through 18H, and all core sections from Hole 1239C were measured after demagnetization at 25 mT only.

NRM intensities prior to demagnetization averaged ~10^{-2} A/m at the top and decreased to ~10^{-3} A/m by ~100 mcd. After AF demagnetization at 25 mT, NRM intensities are generally one order of magnitude lower (Fig. **F22**). The XCB cores from Hole 1239A displayed a significantly wider range of intensities (Fig. **F22**), probably due to biscuiting and core deformation. Within the first meter (composite depth) the NRM intensity before and after demagnetization displays a large (95%) decrease (Fig. **F23**) that may reflect a redox boundary. The same pattern was noted at Site 1238 and may reflect the reducing conditions of these sediments (see **"Geochemistry,"** p. 16). Alternation of the nonmagnetic

F22. Initial and AF demagnetized NRM, p. 53.

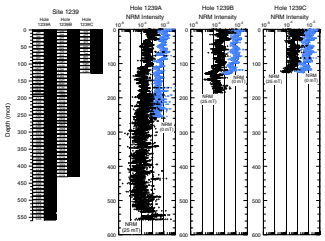

F23. NRM intensity before and after AF demagnetization, 0–10 mcd, p. 54.

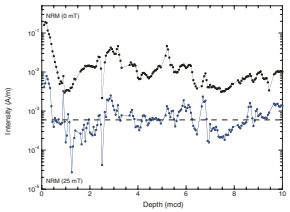

core barrel with a normal steel (magnetic) core barrel resulted in a cyclicity at the NRM intensity that reflects core-length variations resulting from the varying intensity of the magnetic overprint (Fig. F24) (see Lund et al., this volume).

Directional Variability

As observed at the previous sites, inclinations prior to AF demagnetization are steeply positive, characteristic of a drill string–induced magnetic overprint. For the uppermost 40 mcd, inclination values after 25-mT AF demagnetization are closer to the expected value for Site 1239 (–3.7°) (Fig. F25). Below 40 mcd, the sediments are strongly overprinted with steep positive inclinations even after AF demagnetization. Inclinations and declinations within the XCB-cored interval are essentially random and uninterpretable.

Declinations within individual cores of the upper 80 mcd show consistent directions, suggesting that at least some geomagnetic information is retained (Fig. F25). Declinations shifts of ~180° are observed within a few cores, which may represent polarity reversals. These declination shifts occur at ~46 ± 2 mcd in Hole 1239A, ~47 ± 2 mcd in Hole 1239C, ~55 ± 2 mcd in Hole 1239A, and ~54 ± 2 mcd in Hole 1239C, and at ~59 ± 2 mcd in Hole 1239B and 58 ± 2 mcd in Hole 1239C. However, the interpretation of these is not straightforward, as the uppermost declination shift is clearly older than the Brunhes/Matuyama boundary (0.78 Ma) (see "Biostratigraphy," p. 10). These may, therefore, represent polarity transition within the Matuyama. Additional shore-based work will be needed to take the magnetostratigraphic interpretation at Site 1239 any further.

GEOCHEMISTRY

Sediment Gases

Concentrations of headspace gases were routinely monitored in Hole 1239A sediments according to shipboard safety and pollution prevention considerations. Methane was first detected at levels above laboratory blank in a headspace gas sample at 8.1 mcd and increased to >30,000 ppmv by 112.8 mcd (Fig. F26; Table T13). Below this depth, methane concentrations remained high throughout the hole, ranging between 4200 and 66,600 ppmv. Small amounts of ethane were detected, varying between 1.2 and 19.0 ppmv. Higher molecular weight hydrocarbons such as butane were first detected by odor. Natural gas analyses confirmed that small amounts of C_3–C_5 hydrocarbons were present in the sediments, in the interval between ~231 and 451 mcd (Table T13), and determined that gas composition was dominated by CO_2 and methane.

The temperature gradient at Site 1239 is too low to allow thermogenic methane production, which can also produce heavier hydrocarbons. However, heavier hydrocarbons (at least C_2–C_4) can be microbially produced in low concentrations together with C_1 (Vogel et al., 1982; Wiesenburg et al., 1985). In addition, the high methane/ethane ratio (Fig. F26), which is representative of microbial gases, indicates that the methane is of biogenic origin. This is also supported by the disappearance of interstitial sulfate at approximately the same depth where methane content begins to increase. The presence of interstitial

F24. NRM intensity before demagnetization, p. 55.

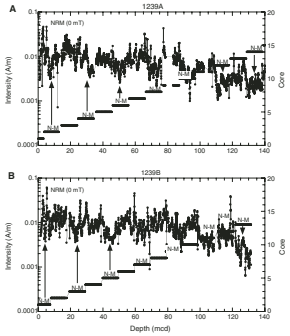

F25. NRM inclinations and declinations, p. 56.

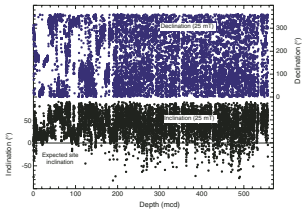

F26. Headspace methane, C_1/C_2, and CO_2, p. 57.

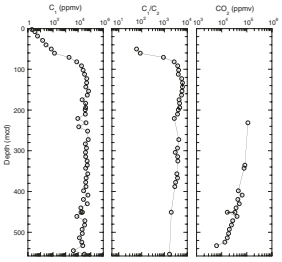

T13. Headspace gas concentrations and C_1/C_2 ratios, p. 88.

sulfate inhibits methanogenesis in marine sediments (Claypool and Kvenvolden, 1983).

Interstitial Water Geochemistry

We collected 42 interstitial water samples from Hole 1239A for shipboard analyses and an additional 31 interstitial water samples at a frequency of one per section for the upper 60 mbsf for shore-based analyses. Chemical gradients at this site (Table T14; Fig. F27) reflect the influence of organic matter oxidation, the dissolution of biogenic silica and its reprecipitation in authigenic phases, the effects of authigenic calcite precipitation, and the diffusive influence of basalt alteration processes. The depth zone of the major hiatus (519.3–527.7 mcd; see "Biostratigraphy," p. 10) is not marked by significant changes in interstitial water chemistry.

Chlorinity averages 559 mM throughout and increases from 553 mM at 1.5 mcd to >560 mM by 29.1 mcd (Fig. F27). Salinity, measured refractively as total dissolved solids, ranges from 31 to 35 (Table T14). Sodium concentrations measured by inductively coupled plasma–atomic emission spectrophotometry averaged 1.7% lower than those estimated by charge balance reported here (Table T14). Sodium concentrations parallel chlorinity, with a total range from 467 to 500 mM.

Organic matter diagenesis, driven by microbially mediated oxidation reactions, influences the interstitial water chemistry. Sulfate decreases to below the detection limit (1.0 mM) by 70.8 mcd, coincident with the increase in methane and approaching the zone of higher organic carbon contents starting at 85 mcd. Total sulfate depletion at this site is in contrast to the partial sulfate depletion seen at Site 1238, at deeper water depth. Alkalinity increases to >28 mM from 91.7 to 123.2 mcd, consistent with alkalinity generation from sulfate reduction, then declines to 3.6 mM at 553.9 mcd. Alkalinity consumption is both from authigenic mineral precipitation within the sediments and from the diffusive influence of basalt alteration reactions.

Dissolved manganese concentrations are low at this site, with values of 1.2–1.3 µM from 1.5 to 8.0 mcd, indicative of limited suboxic oxidation of organic carbon by manganese reduction, then decrease to low values, often below the detection limit (0.1 µM). Manganese increases from 0.5 µM at 513.8 mcd to 3.8 µM at 553.9 mcd from the influence of basalt alteration reactions at greater depth. Dissolved iron has a complex profile with depth, with multiple peaks >10–20 µM.

Phosphate concentrations increase from 5.5 µM at 1.5 mcd to >20 µM from 60.6 to 112.7 mcd. A sharp one-point maximum of 37 µM at 91.7 mcd is analytically robust but may be an artifact related to the acidification of the samples required to deal with the presence of hydrogen sulfide and/or the possible release of scavenged phosphate from fine particles. Ammonium concentrations increase from below the detection limit (0.2 mM) at 1.5 mcd to >6 mM from 133.2 to 377.5 mcd. The increases in phosphate and ammonium result from the oxidation of organic matter, whereas the persistence of high ammonium concentrations throughout indicates more limited sinks in authigenic phases for ammonium than for phosphate.

Dissolved silicate increases from 545 µM at 1.5 mcd to >1800 µM from 482.4 to 503.4 mcd, followed by a sharp decrease in silicate to 1319 µM at 553.9 mcd. Diatoms decrease rapidly >519.3 mcd, and the sediment is barren of diatoms in Sample 202-1239-55X-CC (see "Diatoms," p. 14, in "Biostratigraphy"). The increase in dissolved silicate

T14. Interstitial water geochemical data, p. 89.

F27. Interstitial water geochemical data, p. 58.

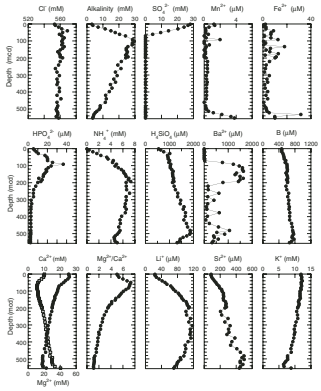

with increasing depth is consistent with temperature-controlled solubility for biogenic opal at this site (see "Operations," p. 3). Site 1238 has a larger thermal gradient (~12.7°C/100 m) than Site 1239 (~8.8°C/100 m). The silicate increase with depth for Site 1239 is less steep than that observed at Site 1238, although peak silicate values are similar and are reached at ~45°C. The increase in solubility of biogenic opal with increasing temperature appears to control the dissolved silicate concentrations until the biogenic opal supply in sediments is exhausted and precipitation of biogenic opal alteration products controls interstitial water composition, with cherts serving as the ultimate sink for dissolved silicate. However, unlike at Site 1238, no cherts were observed at Site 1239.

Barium concentrations increase steeply with the major decline in sulfate, from ≤1 µM at depths <60.6 mcd to generally >1400 µM from 102.3 to 194.0 mcd, and then decrease to 162–167 µM from 220.8 to 241.4 mcd, with continued, more minor variations downcore. Site 1239 has the highest interstitial water barium concentrations of all previous Leg 202 sites. Sites with limited or no sulfate reduction (Sites 1236, 1237, and 1238) have the lowest barium concentrations. Sites with sulfate reduction complete at shallower depths than at Site 1239 (Sites 1232, 1233, 1234, and 1235) have barium enrichments, but these are limited in depth range and maximum concentration. This indicates that the dissolution of barite, driven by decreasing sulfate, affects barium concentrations and that the depth range of sulfate reduction, along with surface productivity, affects the signal of barite remobilization in interstitial water.

Calcium concentrations decrease from 10.1 mM at 1.5 mcd to 5.5 mM from 70.8 to 81.7 mcd, just below the depth of sulfate depletion and shallower than the maximum alkalinity values, then increase to 15.3 mM at 532.9 mcd. The shallow part of this profile is controlled by authigenic calcite precipitation driven by the alkalinity increase, and the deeper portion reflects the diffusive influence of basalt alteration.

Magnesium concentrations increase slightly in the shallowest samples, probably from ion exchange with the sediments driven by the ammonium increase, decrease steeply from 51.5 mM at 18.8 mcd to 38.7 mM at 70.8 mcd, and then decrease more slowly to 17.4 mM at 532.9 mcd. Magnesium concentrations increase in the deepest two samples. Magnesium/calcium ratios increase from 5.0 at 1.5 mcd to 7.3 at 50.5 mcd then decrease to 1.1 in the deepest samples (Fig. F27). The increase in magnesium/calcium in the shallower sediments, driven by the decrease in calcium, indicates that calcite precipitation is the dominant authigenic mineralization reaction, consuming calcium and alkalinity. Below this zone, the increase in calcium from the calcium minimum at 81.7 to 532.9 mcd (~2.4 mM/100 m) is correlated to the decrease in magnesium (approximately –4.9 mM/100 m), consistent with control of these profiles by the diffusive influence of basalt alteration reactions.

Boron concentrations increase from 469 µM at 1.5 mcd to 777 µM at 532.9 mcd then have a small decline in the deepest two samples. Lithium concentrations increase from 24 µM at 1.5 mcd to >100 µM from 163.4 to 398.5 mcd then decrease to 71 µM at 553.9 mcd. The middepth maximum requires a source of lithium from the sediments, whereas basement alteration reactions at low temperatures are a sink for lithium. Strontium concentrations increase with depth from 87 µM at 1.5 mcd to 483 µM at 532.9 mcd then decline somewhat in the deepest samples. This profile does not resemble those dominated by the influence of biogenic calcite recrystallization but does indicate a source of

dissolved strontium at depth in this site. Potassium decreases with depth from 11.9 mM at 1.5 mcd to 6.6 mM at 544.9 mcd. Low-temperature basalt alteration reactions are a sink for dissolved potassium, and this profile can be explained primarily by the diffusive influence of basalt alteration reactions.

Sedimentary Inorganic Carbon, Organic Carbon, and Nitrogen Concentrations

Inorganic carbon (IC), total carbon (TC), and total nitrogen (TN) were determined on sediment samples from Hole 1239A (Table T15). Organic matter carbon/nitrogen ratios were employed to characterize the organic matter. Calcium carbonate and TOC records at Site 1239 are similar to those at deeper water Site 1238.

Calcium carbonate and TOC concentrations reflect the overall uniformity of the sediment lithology at Site 1239 (see "Lithostratigraphy," p. 6). Calcium carbonate concentrations range between 16.0 and 86.6 wt% (average = 59.0 wt%) (Table T15; Fig. F28). In the uppermost ~220 mcd, calcium carbonate contents average ~52 wt%, with large amplitude variations of >10 wt%. Calcium carbonate concentrations reach a minimum at 85.5–115.0 mcd, with values typically <50 wt% and as low as ~30 wt%. At depths >220 mcd, calcium carbonate concentrations generally increase downhole, which may result from the migration of the site toward more coastal conditions with a greater delivery of siliciclastic material that diluted the biogenic components.

TOC concentrations range between 0.3 and 4.4 wt% (average = 1.5 wt%) (Table T15; Fig. F28). In the uppermost 84.0 mcd, TOC contents average 1.3 wt%. TOC concentrations reach a maximum with values >2 wt% at 87.9–125.5 mcd. TOC concentrations generally decrease with greater depth to <0.5 wt% with amplitude variations of 0.5–2.5 wt%. Variations in TN concentrations are similar to those in TOC. The TOC and the calcium carbonate profiles are negatively correlated. For instance, the calcium carbonate minimum corresponds to the TOC maximum, possibly indicating a dilution effect between the two. However, TOC concentrations calculated on a carbonate-free basis (CFB) reflect the same variability as the TOC concentrations (Fig. F28), indicating that most of the TOC variations are not driven by changes in calcium carbonate concentrations. This is also supported by the lack of a strong linear relationship (r^2 = 0.17) between calcium carbonate and TOC concentrations (Fig. F29). The increase in biogenic opal as indicated by smear slide data and low bulk density values, together with a high organic carbon flux, may explain the observed calcium carbonate minimum.

TOC/TN ratios vary between 4.3 and 31.2 (Table T15; Fig. F28) (average = 9.6). In the uppermost 310 mcd, TOC/TN values are around a mean value of ~8.5, which is typical of marine algal material (Bordovskiy, 1965; Emerson and Hedges, 1988; Meyers, 1997). At greater depths, the TOC/TN ratios vary with high amplitudes between 4.3 and 31.2. High TOC/TN values correspond generally to higher TOC (except at 327.3 mcd) and lower TN contents. These variations are interpreted to reflect an input of terrestrial organic matter, which is able to significantly elevate TOC/TN ratios. Although the input of land-derived organic matter may have dominated the organic sedimentation in some intervals at depths >310 mcd, it always remained low, as indicated

T15. IC, $CaCO_3$, TC, TOC, TOC CFB, and TN concentrations, and TOC/TN ratios, p. 90.

F28. Calcium carbonate, TOC, TOC CFB, TN, and TOC/TN vs. depth, p. 59.

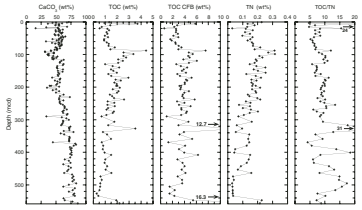

F29. $CaCO_3$ vs. TOC and TN vs. TOC, p. 60.

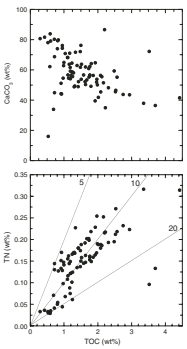

by the generally low TOC contents in that interval. These interpretations will have to be confirmed by shore-based analyses.

It seems therefore that most of the changes in sedimentary TOC and calcium carbonate contents result from a change in the trophic conditions in the overlying waters rather than from preservation. Periods of higher productivity are associated with higher TOC contents and generally correspond to increased diatom abundance (*Thalassiothrix* ooze; see "Diatoms," p. 14, in "Biostratigraphy"). This is particularly the case for the organic matter– and diatom-rich interval between ~90 and 110 mcd, which was deposited during the Pliocene–Pleistocene transition. This organic- and diatom-rich "event" was also found at Site 1238 correlating to the same period.

DOWNHOLE MEASUREMENTS

Logging Operations

Downhole logging was performed in Hole 1239A after it had been drilled to a depth of 517 mbsf with an 11.438-in APC/XCB drill bit (see "Operations," p. 3) and displaced with sepiolite mud and the pipe was set at 80 mbsf. Two tool string configurations were run, the triple combo-MGT and the FMS-sonic (see "Downhole Measurements," p. 36, in the "Explanatory Notes" chapter). No problems were encountered while logging, and all passes reached the base of the hole. Details of the intervals logged with each configuration, together with the position of the drill bit, are shown in Figure F30. The Dipole Sonic Imager (DSI) on the FMS-sonic was run in P&S (middle frequency), lower dipole (low frequency), and first motion detection (FMD) modes. Weather was excellent and the sea state was calm with peak heave <1.5 m. The wireline heave compensator was used throughout the logging operation.

Data Quality

The caliper log (Fig. F31) shows that the borehole was relatively smooth and that the diameter varied between 11.8 and 15.1 in (mean = 12.9 in; standard deviation = 0.9 in), resulting in excellent data from the density, porosity, and FMS tools that require good borehole contact. Although the hole deviation increased with depth, reaching 7.5° at the base, FMS pad contact was not affected and the images were good from the bottom of the hole to 110 mbsf, where the calipers were closed. Downhole log-derived densities mirror the downhole porosities and closely match with core measurements (Figs. F32, F33). NGR measurements are highly reproducible between tools and passes and are similar to the core-derived natural gamma record from Hole 1239A (Figs. F31, F34). Sonic velocities were low but reliable, reproduced well between passes, and are comparable to core measurements (Fig. F32). During the first pass with the MGT, a power failure occurred while logging between 489 and 479.5 mbsf and no data were acquired in this interval (Fig. F31).

Results

Overall, the physical properties at Site 1239 are relatively homogeneous, suggesting a fairly uniform lithology throughout the sequence.

F30. Logging tool string deployments, p. 61.

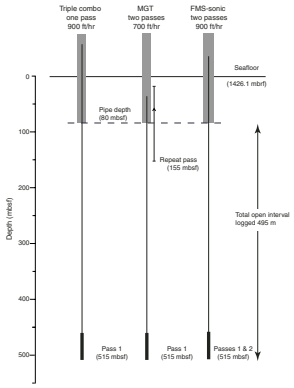

F31. Caliper, deviation, and gamma ray records, p. 62.

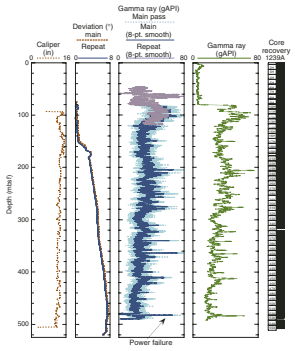

F32. Density, porosity, sonic velocity, and resistivity data, p. 63.

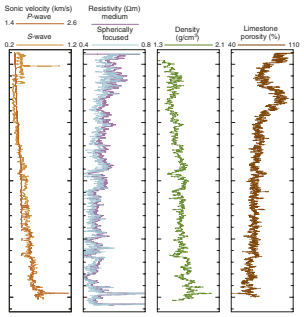

Sonic velocities and densities increase gradually with depth, whereas mean resistivity and porosity both decrease downhole. These large-scale changes in the sediment physical properties are most likely related to sediment compaction and lithification with depth. At higher frequencies, covariations in density and resistivity, similar to those observed at Site 1238, occur throughout the sequence. As at Site 1238, these meter-scale density and resistivity fluctuations are most likely related to the biogenic silica to carbonate oscillations observed in the cores (see "Lithostratigraphy," p. 6). Color banding on the FMS images occurs on the same scale as the density changes associated with the nannofossil to diatom oscillations (Fig. F35).

A pronounced spike in resistivity, sonic velocity, and density (porosity minima) occurs at ~493 mbsf, similar in magnitude to the spikes in physical properties found near the base of Hole 1238A related to well-lithified chalk beds. The spikes in physical properties occur much deeper (>100 mbsf) in the section at Site 1239 relative to Site 1238, and the well-cemented chalks and chert layers found at Site 1238 were not recovered at Site 1239. A deeper diagenetic front at Site 1239 is consistent with the offset in pore water silicate concentration profiles between the sites, suggesting that the lower thermal gradient at Site 1239 may be important in increasing the depth of chert formation at this site (see "Geochemistry," p. 16).

Natural Gamma Radiation

The NGR activity in Hole 1239A shows significant meter- and dekameter-scale variability superimposed upon a general decrease with depth (Figs. F31, F36). The spectral gamma results from the Hostile Environment Gamma Ray Sonde (HNGS) tool (Fig. F36) show low, regularly varying Th and K activity throughout the sequence. In contrast, the U activity and variability is much greater, reaching its highest values between 95 and 111 mbsf. The high overall U activity dominates the total gamma ray activity of the sediments. As at Site 1238, the U log shows a similar overall trend to the TOC measured in the cores (Fig. F36), indicating that changes in organic matter rather than terrigenous input controls sediment gamma ray activity at Site 1239 since the late Miocene. Although both the U and total counts are slightly higher at Site 1239 relative to Site 1238, the magnitude of the variability and overall trends are the similar at both sites.

Core-Log Comparisons

Log-derived density and NGR records show close agreement with core measurements from the Hole 1239A down to the meter scale (Figs. F33 and F34, respectively). On average, downhole densities are often slightly higher (~0.5 g/cm³) than core measured densities and do not show the pronounced minima (<1.2 g/cm³) evident in the raw GRA density record. The difference in mean values may be due to core expansion, whereas the frequent minima evident in GRA density may be due to the higher resolution of core measurements or erroneous values resulting from coring disturbance. However, on the meter scale, variability in core measurements closely matches downhole changes in density. Using the downhole log density and NGR records as a depth reference, the core measurements were mapped to equivalent log depths (eld) using the software program Sagan in order to more precisely identify the size and position of core breaks within the XCB sec-

F33. Log and core density vs. eld, p. 64.

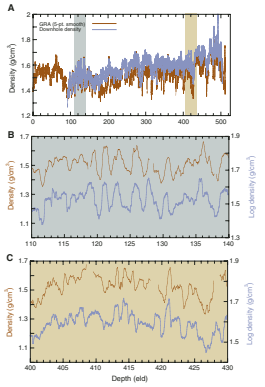

F34. Log and core natural gamma radiation vs. eld, p. 65.

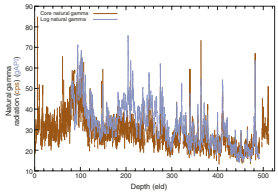

F35. FMS image of illustrating the meter-scale banding, p. 66.

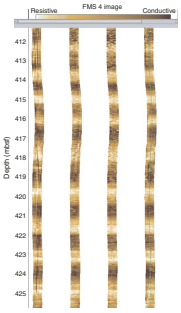

F36. Total and spectral gamma ray records, p. 67.

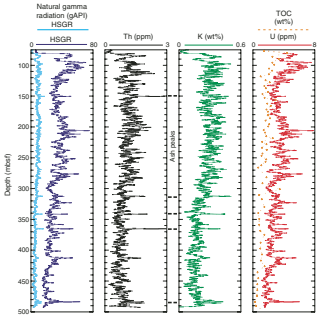

tion (see "Composite Section," p. 5). Despite the high recovery, after mapping to the logs the resulting gaps between XCB cores (1–3 m) are similar in scale to the period of many of the density and natural gamma ray fluctuations. Hence, we are able to identify a number of missed cycles in the XCB cored interval.

AGE MODEL AND MASS ACCUMULATION RATES

A 560.7-mcd-thick (515.4 mbsf) sequence of Miocene (~15 Ma) to Pleistocene pelagic sediments was recovered at Site 1239. Biostratigraphic datums (Table T9) were used to construct an age-depth model for this site (Table T16; Fig. F37). Linear sedimentation rates (LSRs), total MARs, and carbonate MARs were calculated at 1-m.y. intervals (see "Age Models and Mass Accumulation Rates," p. 41 in the "Explanatory Notes" chapter).

T16. Age-depth model, LSRs, and MARs, p. 93.

F37. Shipboard biostratigraphic and magnetostratigraphic datums and age-depth model, p. 68.

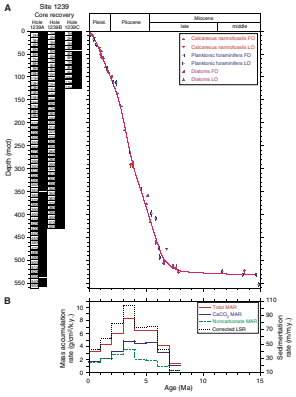

Age-Depth Model

The generation of the age-depth model for Site 1239 (Fig. F37) relied upon all available microfossil datums, which generally agree well with few outliers. A hiatus is present at ~530 mcd, spanning the interval 14.6 to ~8 Ma. Frequent and persistent reworking was noted in the upper Miocene–lower Pliocene interval (see "Biostratigraphy," p. 10)

A decision was made to use the majority of the planktonic foraminiferal and diatom datums in the interval 460–520 mcd, rather than a single calcareous nannofossil datum (the top of the *R. pseudoumbilicus* [>7 µm] absence interval) because low abundance may make this datum unbelievable. This decision resulted in relatively high LSRs (~55 to ~75 m/m.y.) and MARs (~4.5 to ~6 g/cm²/k.y.) during the interval 7 to 5 Ma.

Given the low-precision age control points, this age-depth model is not fully constrained in all the 1-m.y. intervals used for the calculation of LSRs and MARs, and this dictates caution when interpreting variations.

Linear Sedimentation and Mass Accumulation Rates

LSRs range between ~10 and 104 m/m.y, and total MARs range from ~1 to 8 g/cm²/k.y. All rates display a broad peak between 6 and 2 Ma that is driven by both carbonate and noncarbonate MARs. Maximum rates are indicated at 4–3 Ma (194–306 mcd), but the details of the broad peak are somewhat dependent on choices made in the definition of the age model and the 1-m.y. sampling of the model. If the model is sampled at 2 m.y., the maximum carbonate MAR occurs earlier, between 6 and 4 Ma. This pattern is generally consistent with trends predicted by eastward tectonic drift, which suggests relatively high production when the site was centered under the productive south equatorial current from 4 to 6 Ma (see "Introduction," p. 1). However, regional oceanographic changes and nutrient budgets may also contribute to these variations in MARs, consistent with similar peaks in carbonate MAR at other sites, although elsewhere peak MAR is older, typically occurring at 5–7 Ma (Farrell et al., 1995; Pisias et al., 1995). The relative divergence of the LSRs from the total MAR is most pronounced for that last 1 m.y. as a result of decreasing overburden and associated high porosity near the top of the record, and where all rates are at a maximum (4-3 Ma), which has no obvious lithologic explanation. The relatively

smooth trend of LSRs and MARs at Site 1239 reflects the relatively homogeneous lithology of the entire sediment sequence recovered here.

REFERENCES

Beaufort, L., Garidel-Thoron, T., Mix, A.C., and Pisias, N.G., 2001. ENSO-like forcing on oceanic primary production during the late Pleistocene. *Science,* 293:2440–2444.

Behrenfeld, M.J., Randerson, J.T., McClain, C.R., Feldman, G.C., Los, S.O., Tucker, C.J., Falkowski, P.G., Field, C.B., Frouin, R., Esaias, W.E., Kolber, D.D., and Pollack, N.H., 2001. Biospheric primary production during and ENSO transition. *Science,* 291:2594–2597.

Berggren, W.A., Kent, D.V., Swisher, C.C., III, and Aubry, M.-P., 1995. A revised Cenozoic geochronology and chronostratigraphy. *In* Berggren, W.A., Kent, D.V., Aubry, M.-P., and Hardenbol, J. (Eds.), *Geochronology, Time Scales and Global Stratigraphic Correlation*. Spec. Publ.—SEPM, 54:129–212.

Bloomer, S.F., Mayer, L.A., and Moore, T.C., Jr., 1995. Seismic stratigraphy of the eastern equatorial Pacific Ocean: paleoceanographic implications. *In* Pisias, N.G., Mayer, L.A., Janecek, T.R., Palmer-Julson, A., and van Andel, T.H. (Eds.), *Proc. ODP, Sci. Results,* 138: College Station, TX (Ocean Drilling Program), 537–553.

Bordovskiy, O.K., 1965. Accumulation and transformation of organic substances in marine sediment, 2. Sources of organic matter in marine basins. *Mar. Geol.,* 3:5–31.

Bowles, F.A., Jack, R.N., and Carmichael, I.S.E., 1973. Investigation of deep-sea volcanic ash layers from equatorial Pacific cores. *Geol. Soc. Am. Bull.,* 84:2371–2388.

Cane, M.A., 1986. El Niño. *Annu. Rev. Earth Planet. Sci.,* 14:43–70.

Claypool, G.E., and Kvenvolden, K.A., 1983. Methane and other hydrocarbon gases in marine sediment. *Annu. Rev. Earth Planet. Sci.,* 11:299–327.

Duncan, R.A., and Hargraves, R.B., 1984. Plate tectonic evolution of the Caribbean region in the mantle reference frame. *In* Bonini, W.E., Hargraves, R.B., and Shagam, R. (Eds.), *The Caribbean-South American Plate Boundary and Regional Tectonics*. Mem.—Geol. Soc. Am., 162:81–94.

Emerson, S., and Hedges, J.I., 1988. Processes controlling the organic carbon content of open ocean sediments. *Paleoceanography,* 3:621–634.

Farrell, J.W., Raffi, I., Janecek, T.C., Murray, D.W., Levitan, M., Dadey, K.A., Emeis, K.-C., Lyle, M., Flores, J.-A., and Hovan, S., 1995. Late Neogene sedimentation patterns in the eastern equatorial Pacific. *In* Pisias, N.G., Mayer, L.A., Janecek, T.R., Palmer-Julson, A., and van Andel, T.H. (Eds.), *Proc. ODP, Sci. Results,* 138: College Station, TX (Ocean Drilling Program), 717–756.

Hayward, B.W., 2001. Global deep-sea extinctions during the Pleistocene ice-ages. *Geology,* 29:599–602.

Kemp, A.E.S., Baldauf, J.G., and Pearce, R.B., 1995. Origins and paleoceanographic significance of laminated diatom ooze from the eastern equatorial Pacific Ocean. *In* Pisias, N.G., Mayer, L.A., Janecek, T.R., Palmer-Julson, A., and van Andel, T.H. (Eds.), *Proc. ODP, Sci. Results,* 138: College Station, TX (Ocean Drilling Program), 641–645.

Lea, D.W., Pak, D.K., and Spero, H.J., 2000. Climate impact of late Quaternary equatorial Pacific sea surface temperature variations. *Science,* 289:1719–1724.

Ledbetter, M.T., 1985. Tephrochronology of marine tephra adjacent to Central America. *Geol. Soc. Am. Bull.,* 96:77–82.

Levitus, S., Conkright, M.E., Reid, J.L., Najjar, R.G., and Mantyla, N.A., 1993. Distribution of nitrate, phosphate, and silicate in the world oceans. *Prog. Oceanogr.,* 31:245–273.

Lonsdale, P., and Klitgord, K.D., 1978. Structure and tectonic history of the eastern Panama Basin. *Geol. Soc. Am. Bull.,* 89:981–999.

Lyle, M., Liberty, L., Mix, A., Pisias, N., Goldfinger, C., Hulett, D., and Janik, A., 2000. *Site Survey Data Package 5: Site Surveys for ODP Leg 201 from the NEMO-3 Cruise, in Support of Proposal 465: Southeast Pacific Paleoceanographic Transects*. CGISS Tech. Rpt. 2000-06, Boise State University.

Meyers, P.A., 1997. Organic geochemical proxies of paleoceanographic, paleolimnologic, and paleoclimatic processes. *Org. Geochem.,* 27:213–250.

Mix, A.C., Morey, A.E., Pisias, N.G., and Hostetler, S., 1999. Foraminiferal faunal estimates of paleotemperatures: circumventing the no-analog problems yields cool ice-age tropics. *Paleoceanography,* 14:350–359.

Mix, A.C, Pisias, N.G., Goldfinger, C., Lyle, M., Liberty, L., Janik, A., Hebbeln, D., Wefer, G., and Lamy, F., 2000. *Southeast Pacific Paleoceanographic Transects, Site Survey Data Package 4: NEMO Expedition, Leg III, R/V* Melville, *May–June 2000:* Corvallis (Oregon State Univ.).

Mix, A.C., Pisias, N.G., Zahn, R., Rugh, W., Lopez, C., and Nelson, K., 1991. Carbon 13 in Pacific deep and intermediate waters, 0–370 ka: implications for ocean circulation and Pleistocene CO_2. *Paleoceanography,* 6:205–226.

Molina-Cruz, A., 1977. The relation of the southern trade winds to upwelling processes during the last 75,000 years. *Quat. Res.,* 8:324–339.

Murray, J.W., Barber, R.T., Roman, M.R., Bacon, M.P., Feely, R.A., 1994. Physical and biological controls on carbon cycling in the equatorial Pacific. *Science,* 266:58–65.

Ninkovich, D., and Shackleton, N.J., 1975. Distribution, stratigraphic position and age of ash layer L, in the Panama Basin region. *Earth Planet. Sci. Lett.,* 27:20–34.

Ocean Climate Laboratory, 1999. *World Ocean Atlas 1998 (WOA98)* [CD-ROM]. Available from: National Climatic Data Center, Asheville NC 28801-5001, USA.

Pisias, N.G., Mayer, L.A., and Mix, A.C., 1995. Paleoceanography of the eastern equatorial Pacific during the Neogene: synthesis of Leg 138 drilling results. *In* Pisias, N.G., Mayer, L.A., Janecek, T.R., Palmer-Julson, A., and van Andel, T.H. (Eds.), *Proc. ODP, Sci. Results,* 138: College Station, TX (Ocean Drilling Program), 5–21.

Pisias, N.G., and Mix, A.C., 1997. Spatial and temporal oceanographic variability of the eastern equatorial Pacific during the late Pleistocene: evidence from radiolaria microfossils. *Paleoceanography,* 12:381–393.

Silva, A.J., Hollister, C.D., Laine, E.P., and Beverly, B., 1976. Geotechnical properties of the northern Bermuda Rise. *Mar. Geotechnol.,* 1:195–232.

Strub, P.T., Mesias, J.M., Montecino, V., Rutllant, J., and Salinas, S., 1998. Coastal ocean circulation off western South America. *In* Robinson, A.R., and Brink, K.H. (Eds.), *The Sea* (Vol. 11): *Coastal Oceans:* New York (Wiley), 273–313.

Tsuchiya, M., and Talley, L.D., 1998. A Pacific hydrographic section at 88°W: water-property distribution. *J. Geophys. Res.,* 103:12899–12918.

Vogel, T.M., Oremland, R.S., and Kvenvolden, K.A., 1982. Low-temperature formation of hydrocarbon gases in San Francisco Bay sediment (California). *Chem. Geol.,* 37:289–298.

Wiesenburg, D.A., Brooks, J.M., and Bernard, B.B., 1985. Biogenic hydrocarbon gases and sulfate reduction in the Orca Basin brine. *Geochim. Cosmochim. Acta,* 49:2069–2080.

Figure F1. Locations of Sites 1238–1242 and regional bathymetry of Carnegie Ridge.

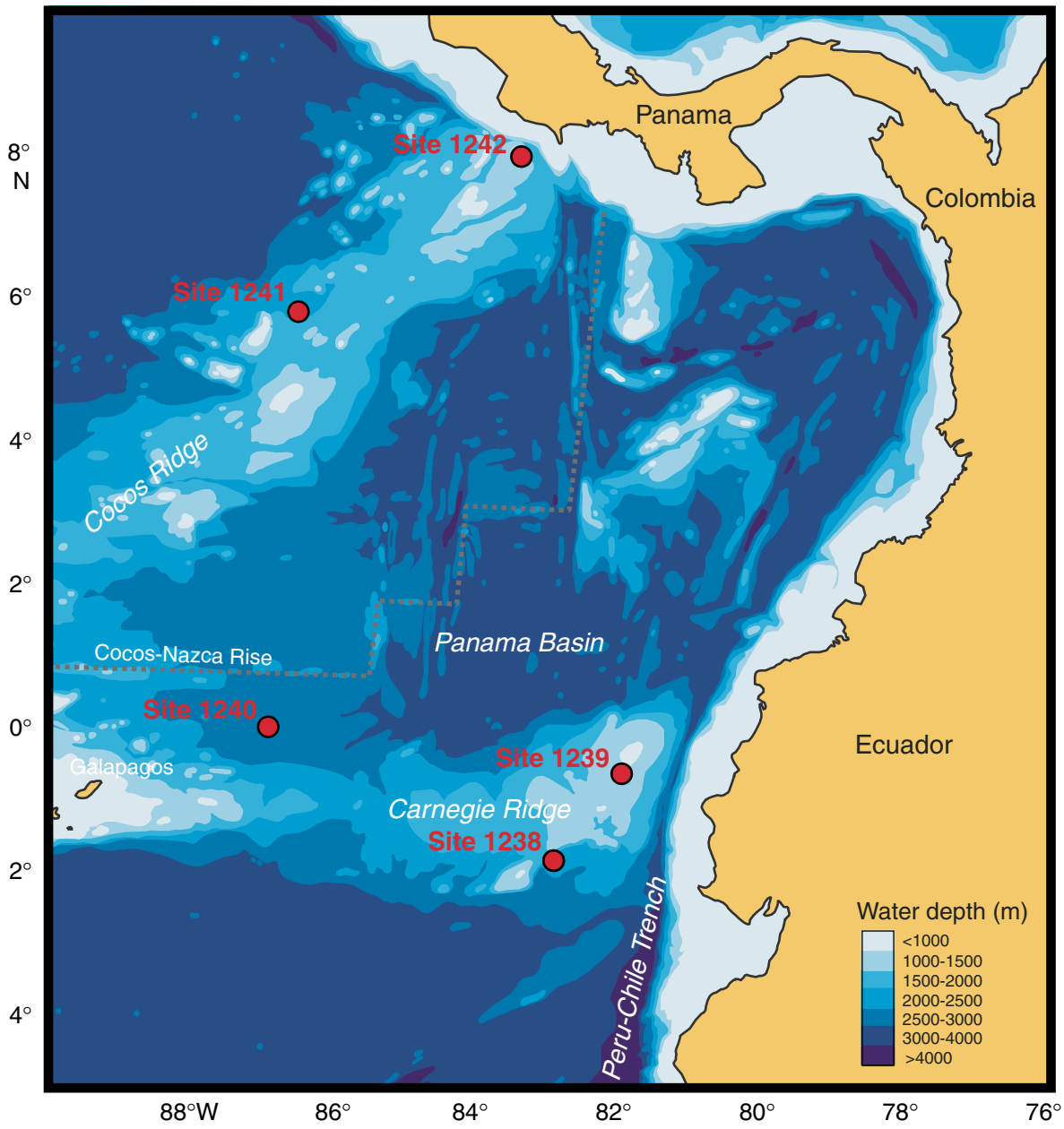

Figure F2. High-resolution swath bathymetry, illustrated in an oblique view (Mix et al., 2000). The sedimented platform covers an area of at least ~50 km (northeast-southwest) × ~30 km (northwest-southeast).

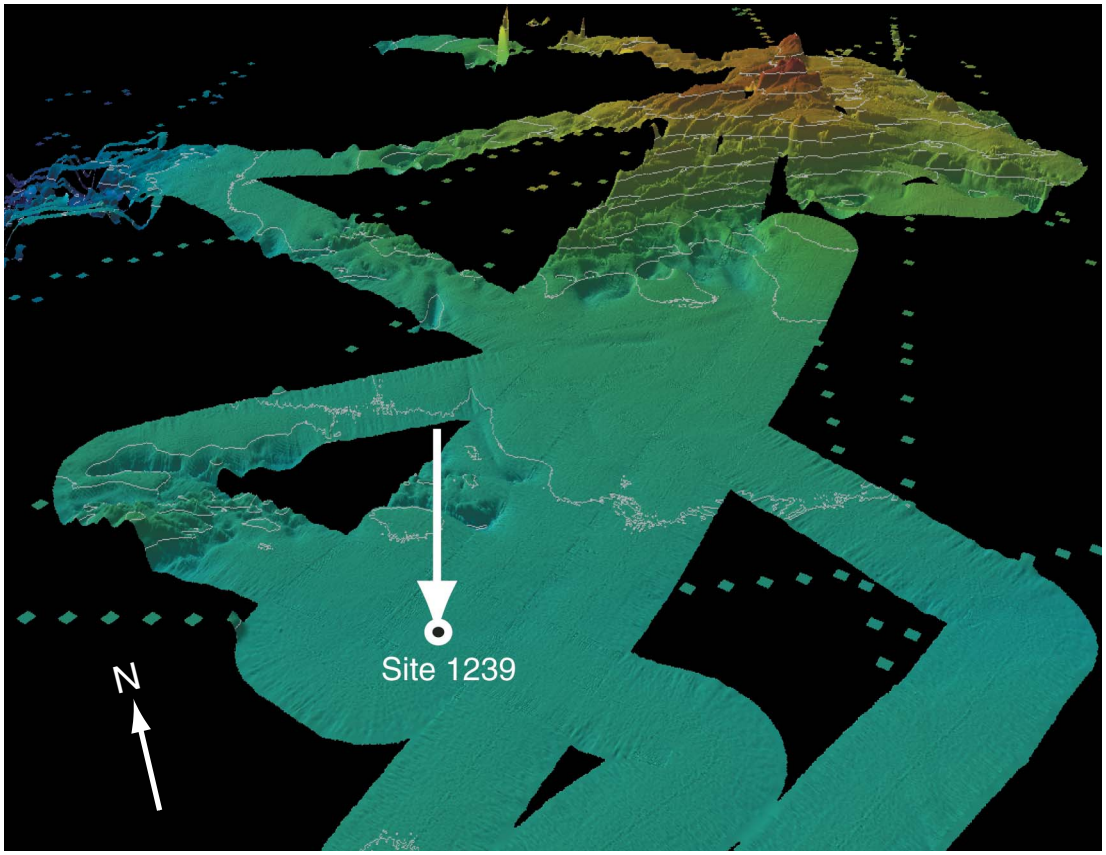

Figure F3. Seismic profile at Site 1239 (*Melville,* NEMO-3, CAR-1C, line 6, JD150, 29 May 2000; two 150-in^3 generator injector guns; Lyle et al., 2000). Identified seismic reflectors are based on correlation to dated events at ODP Site 846 (Bloomer et al., 1995).

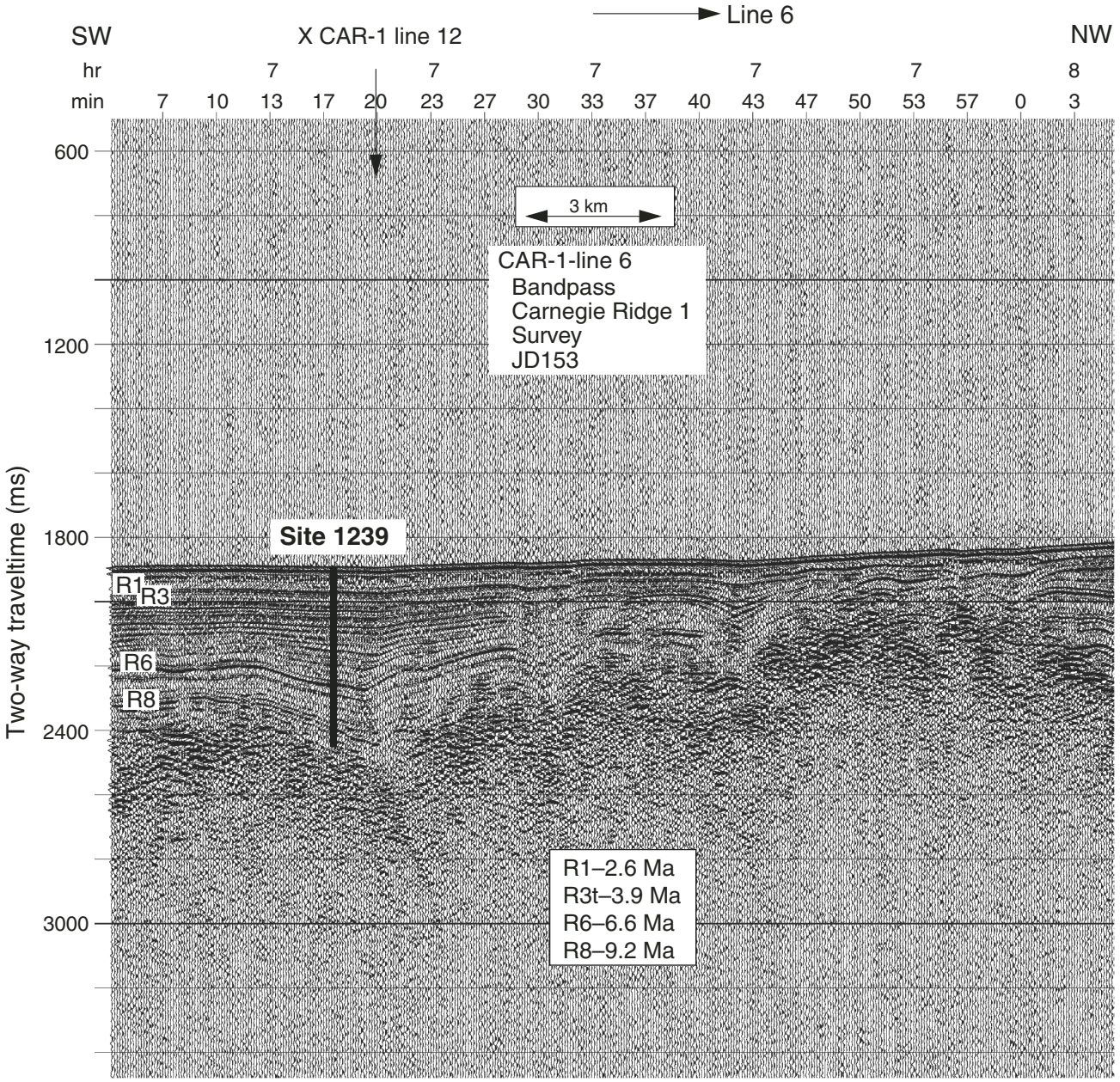

Figure F4. Tectonic backtrack of Site 1239, relative to a fixed South America. Poles of rotation are from Duncan and Hargraves (1984) and Pisias et al. (1995). The dotted path represents position of sites in million-year increments. Numbers note the age (in millions of years) of changes in rate or direction of drift. Contours of modern mean annual sea-surface temperature (in degrees Celsius) are superimposed (Ocean Climate Laboratory, 1999).

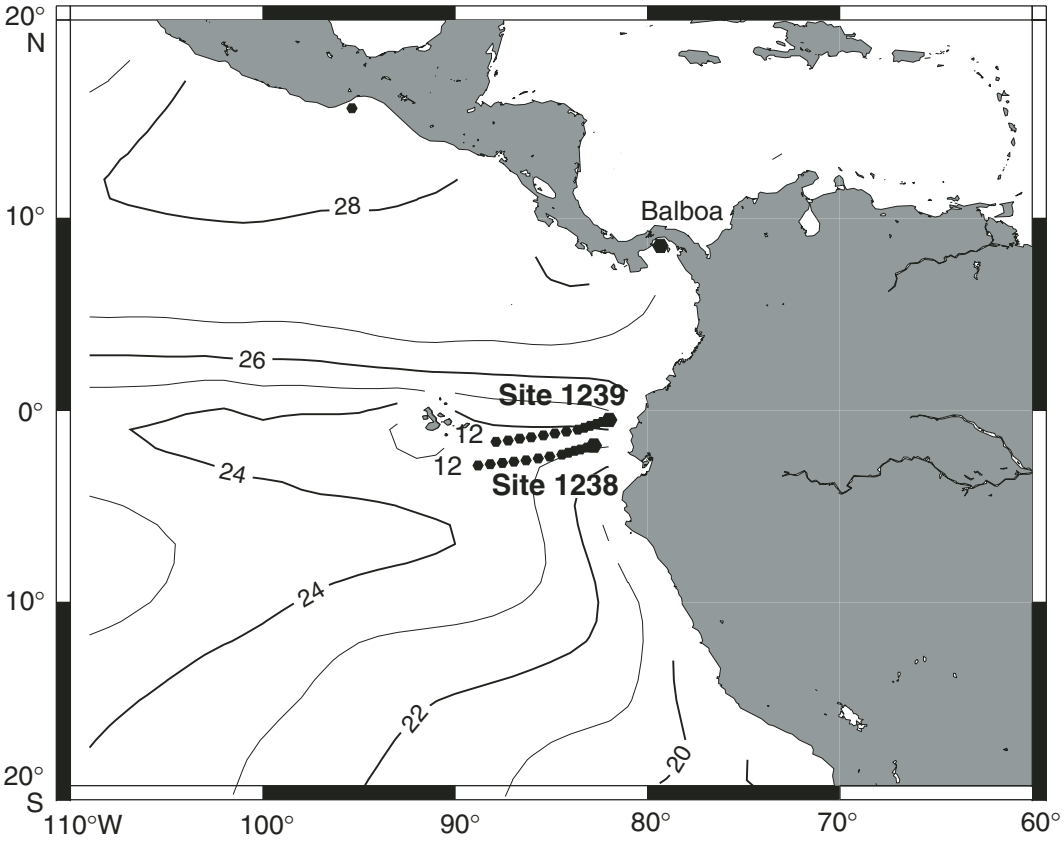

Figure F5. Upper-ocean features off Peru and northern Chile during Southern Hemisphere winter after Strub et al. (1998). SEC = South Equatorial Current, NECC = North Equatorial Countercurrent, EUC = Equatorial Undercurrent, PCC = Peru-Chile Current, PCCC = Peru-Chile Countercurrent, CC = Coastal Current, GUC = Gunther Undercurrent. Modern mean annual sea-surface temperatures (SSTs) (in degrees Celsius, after Ocean Climate Laboratory, 1999).

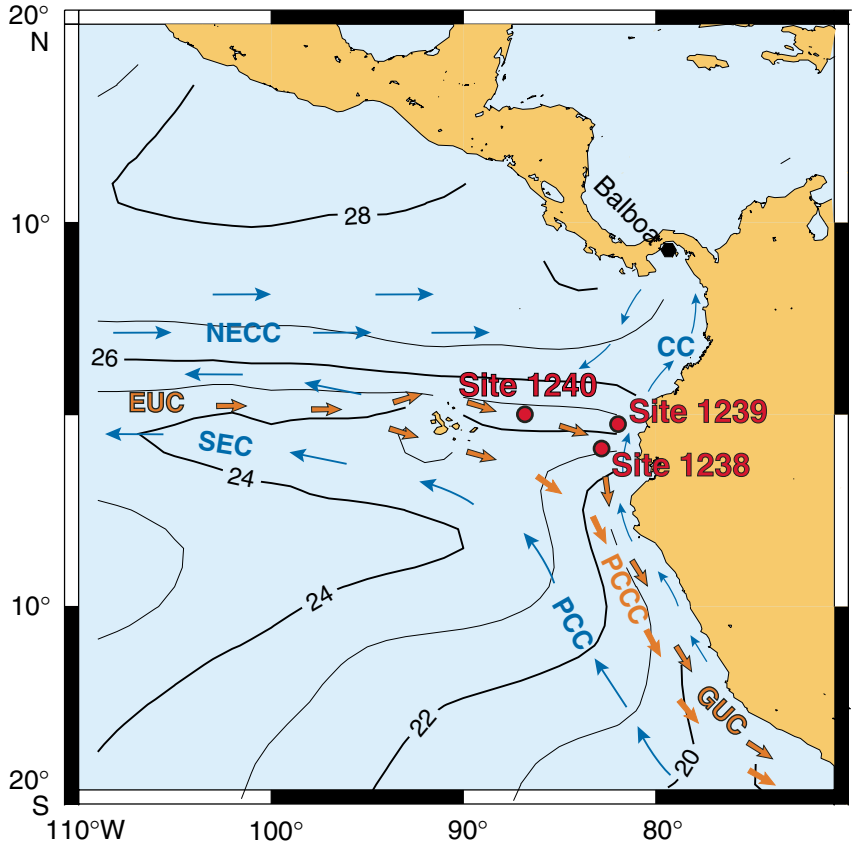

Figure F6. Chlorophyll distributions in surface waters of the equatorial Pacific, based on satellite color data, reveal that Site 1239 is now within the highly productive upwelling system off Ecuador.

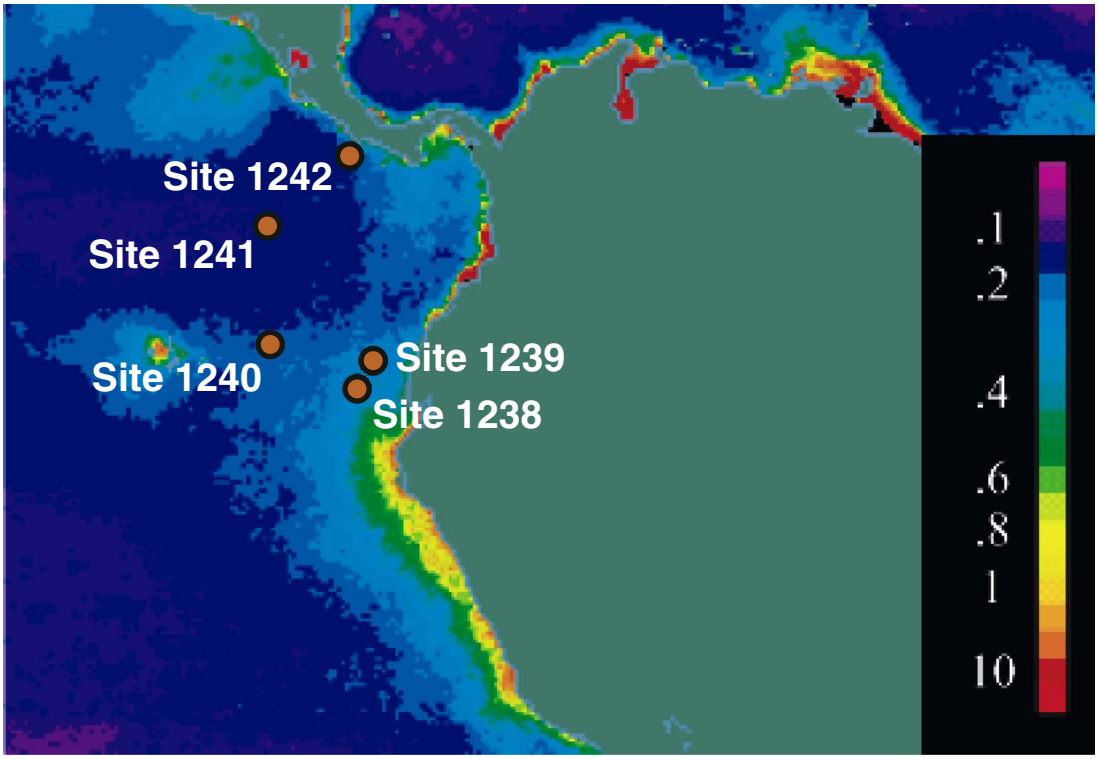

Figure F7. Modern annual-average properties of the upper ocean at paleolocations of Site 1239, based on plate tectonic backtracking and an assumption of no temporal changes in regional oceanic properties. Atlas data on physical and chemical properties are from WOA98 (Ocean Climate Laboratory, 1999). Primary productivity (PP) is from satellite measurements of sea-surface color (Behrenfeld et al., 2001). Pycnocline depth is calculated to the nearest 5 m, based on the shallowest maximum in the vertical density gradient. Symbols are average values extracted from the nearest 1° latitude-longitude box in each atlas. Lines = smoothed trends of each property along the backtrack path. SST = sea-surface temperature, SSS = sea-surface salinity.

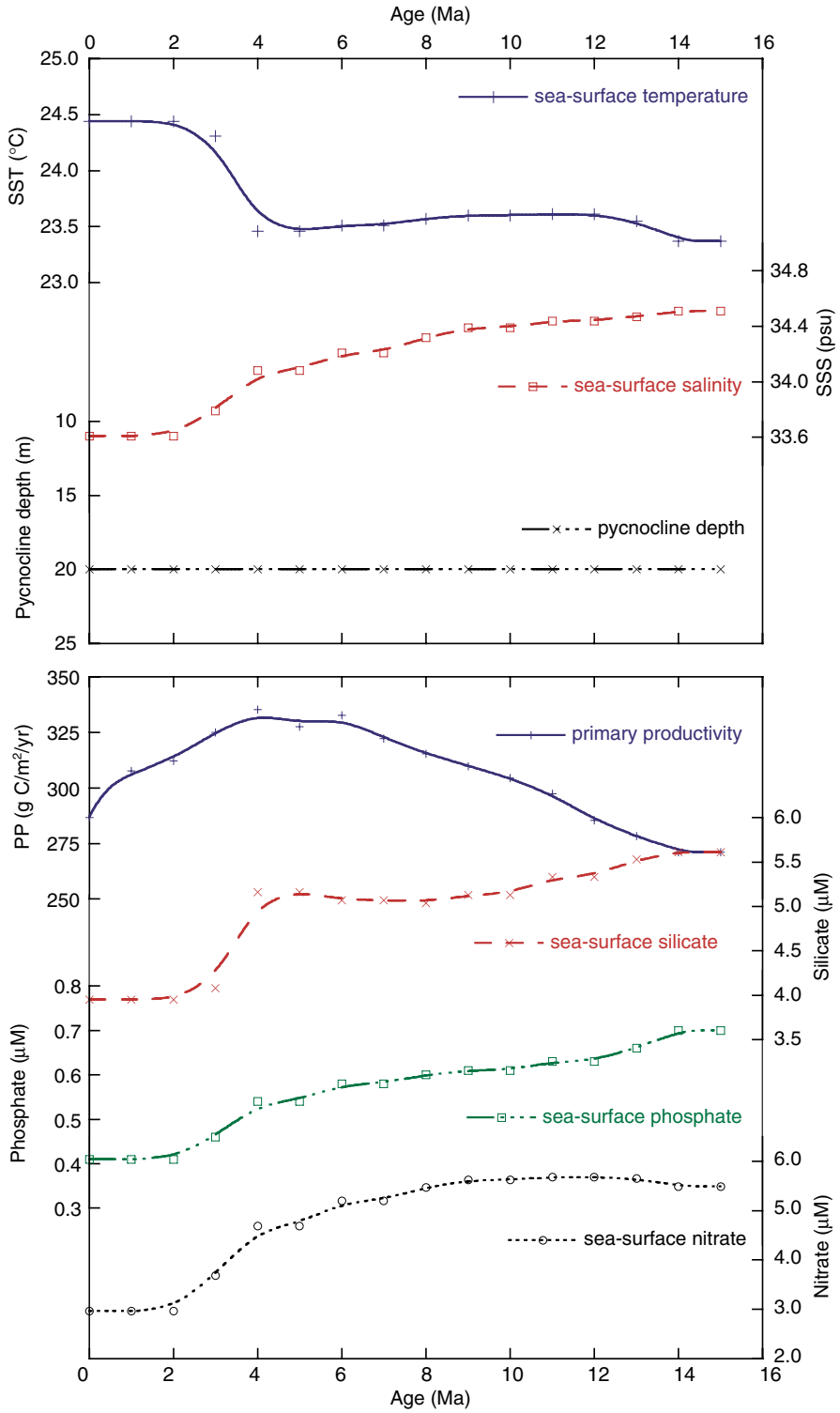

Figure F8. Meridional cross section of water masses, characterized by dissolved oxygen concentrations in the southeast Pacific (Ocean Climate Laboratory, 1999). GUC = Gunther Undercurrent, EUC = Equatorial Undercurrent, NPIW = North Pacific Intermediate Water, PCW = Pacific Central Water, PBW = Peru Basin Water.

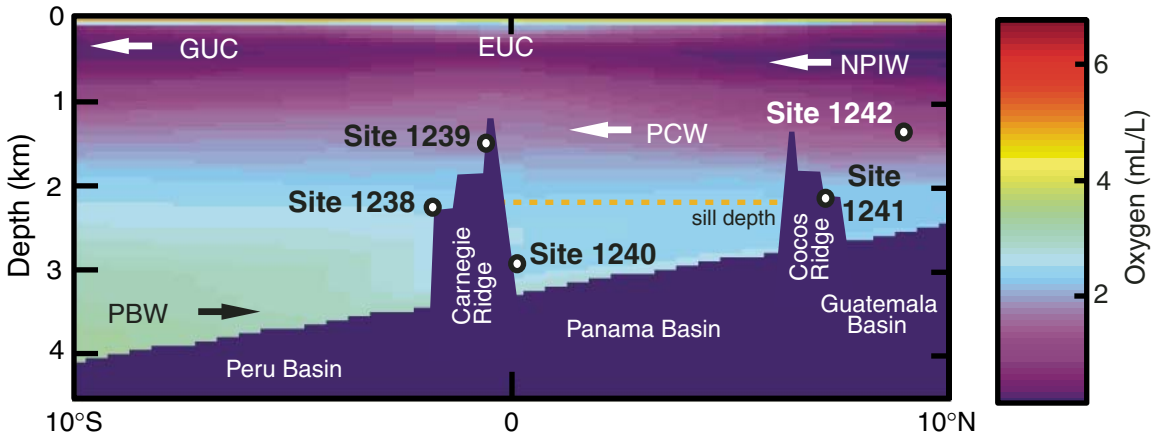

Figure F9. Magnetic susceptibility data collected with the OSU Fast Track (OSUS-MS; in the APC cores) or with the multisensor track (MST-MS; in the XCB cores) vs. mcd for the spliced record and Holes 1239A (black), 1239B (red), and 1239C (green). Gray boxes indicate the portions of cores that are in the splice. **A.** 0–40 mcd. **B.** 30–70 mcd. (Continued on next six pages.)

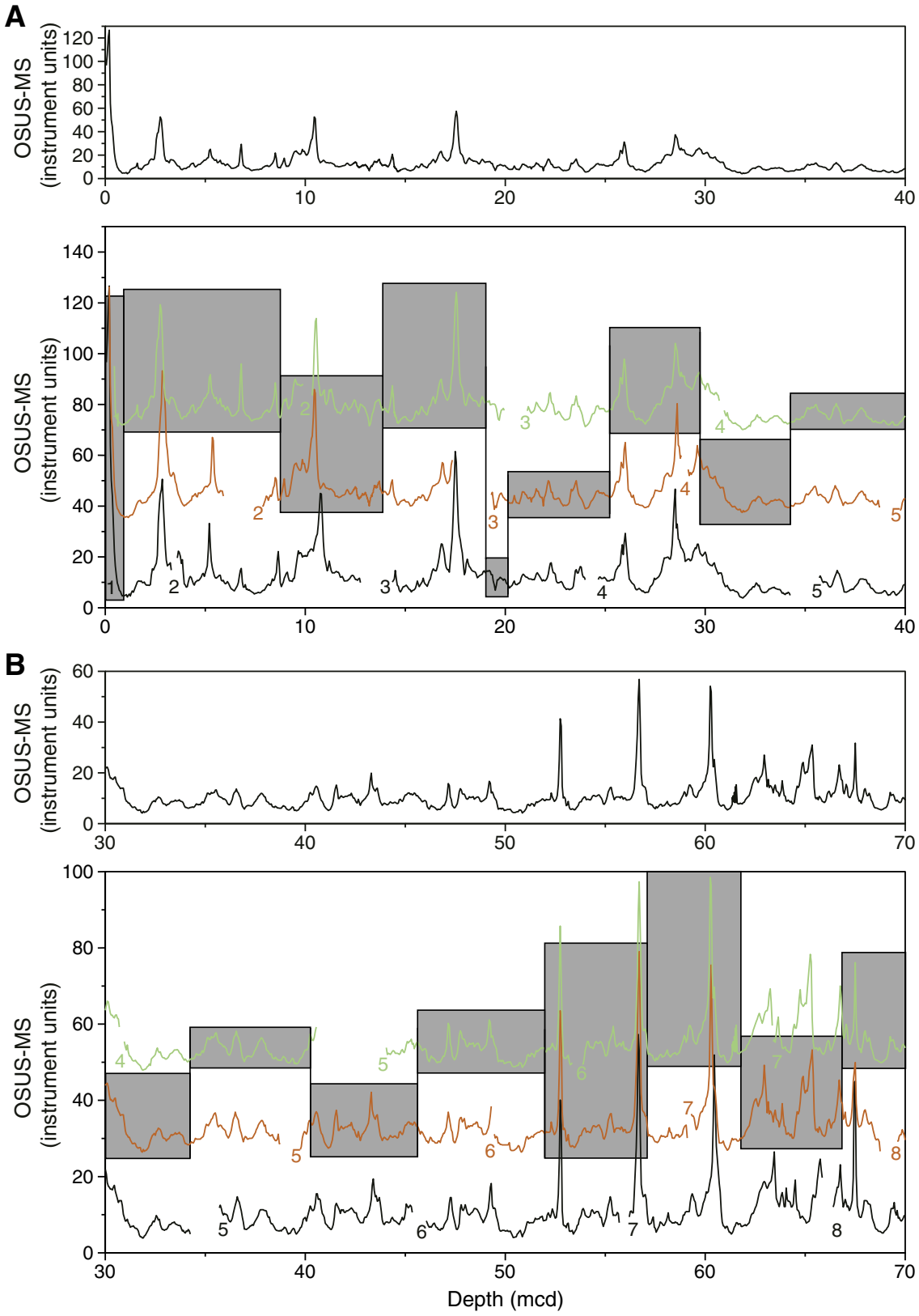

Figure F9 (continued). C. 60–100 mcd. D. 90–130 mcd.

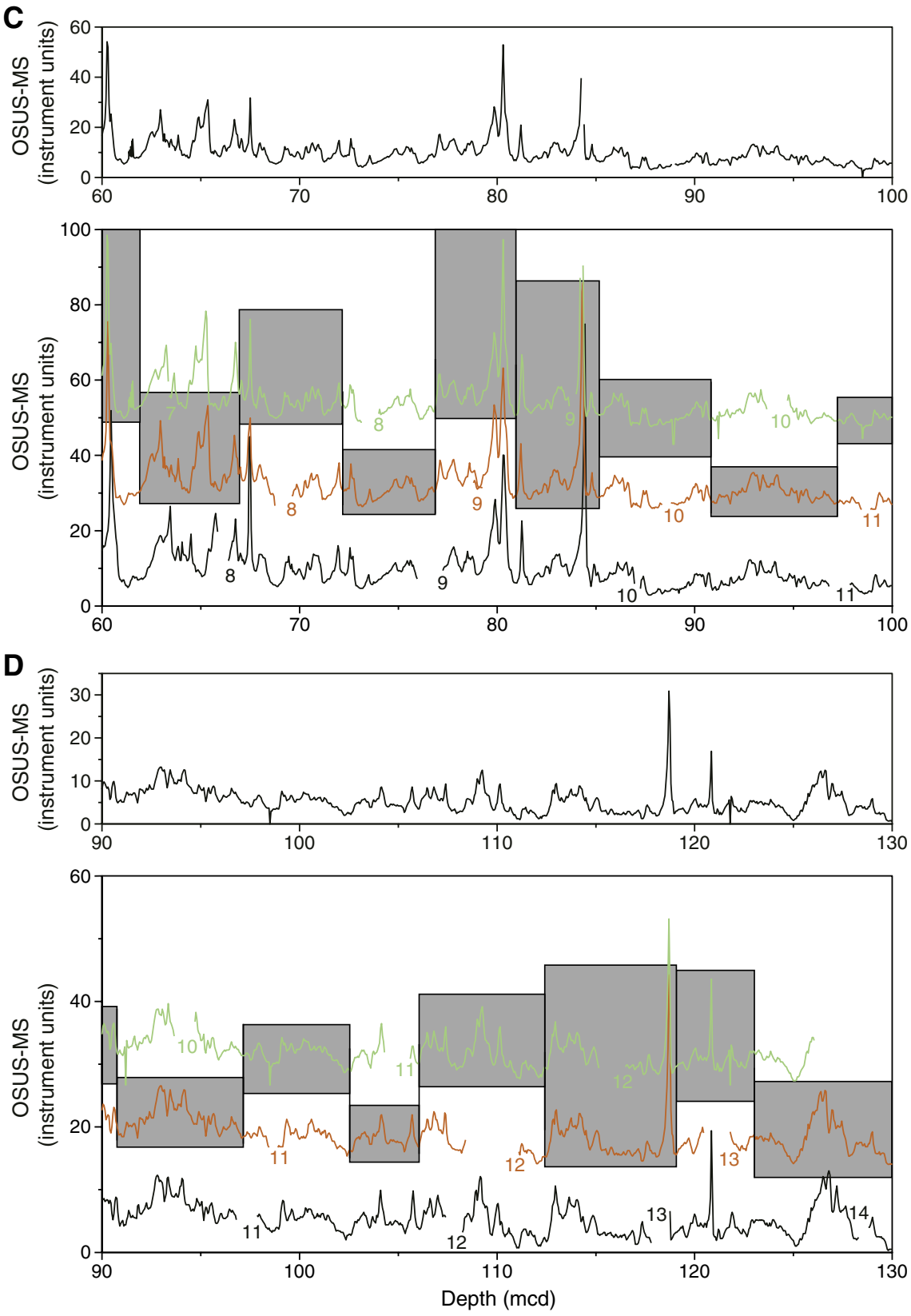

Figure F9 (continued). E. 120–160 mcd. F. 150–190 mcd.

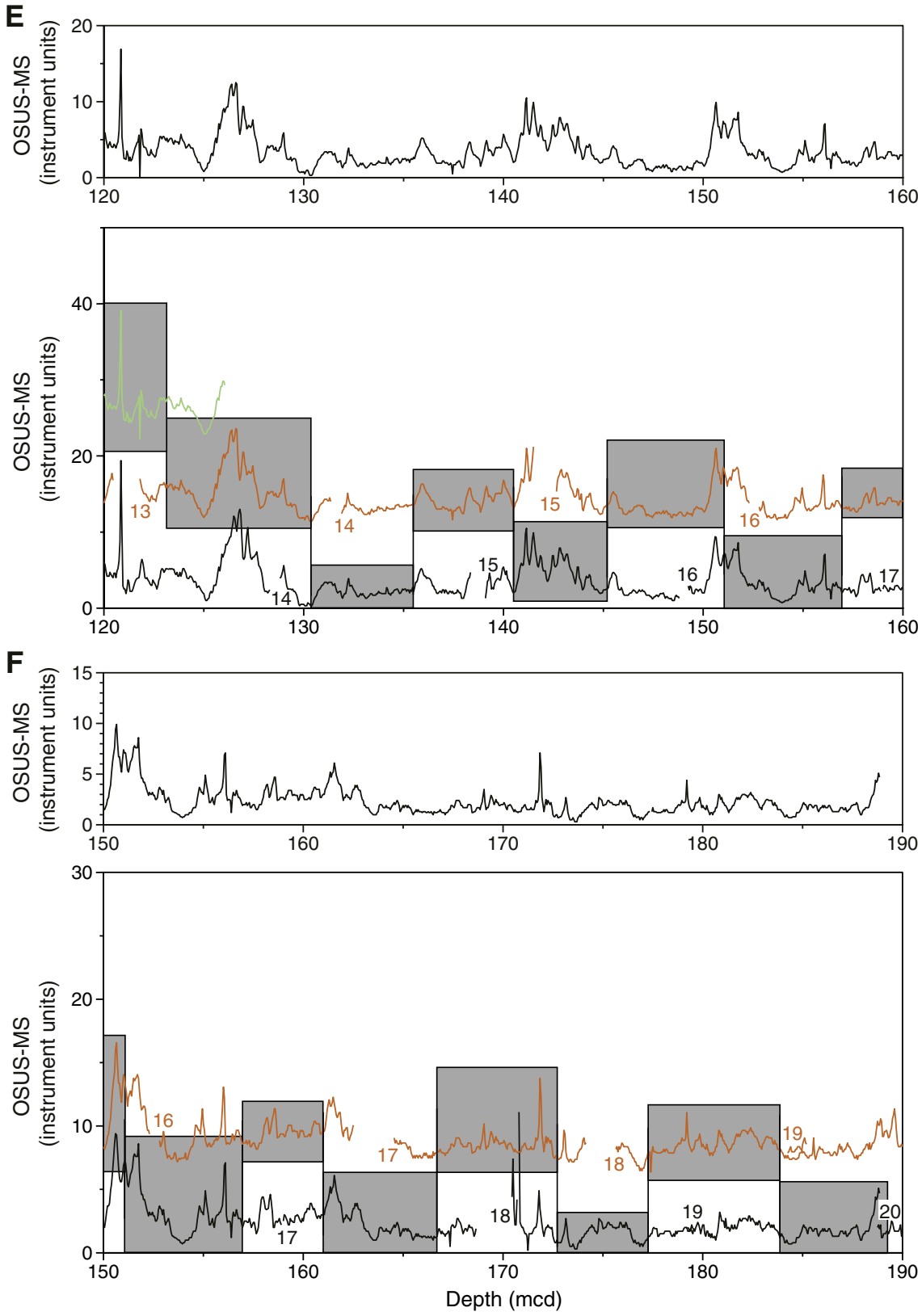

Figure F9 (continued). G. 180–220 mcd. H. 210–250 mcd. I. 240–280 mcd.

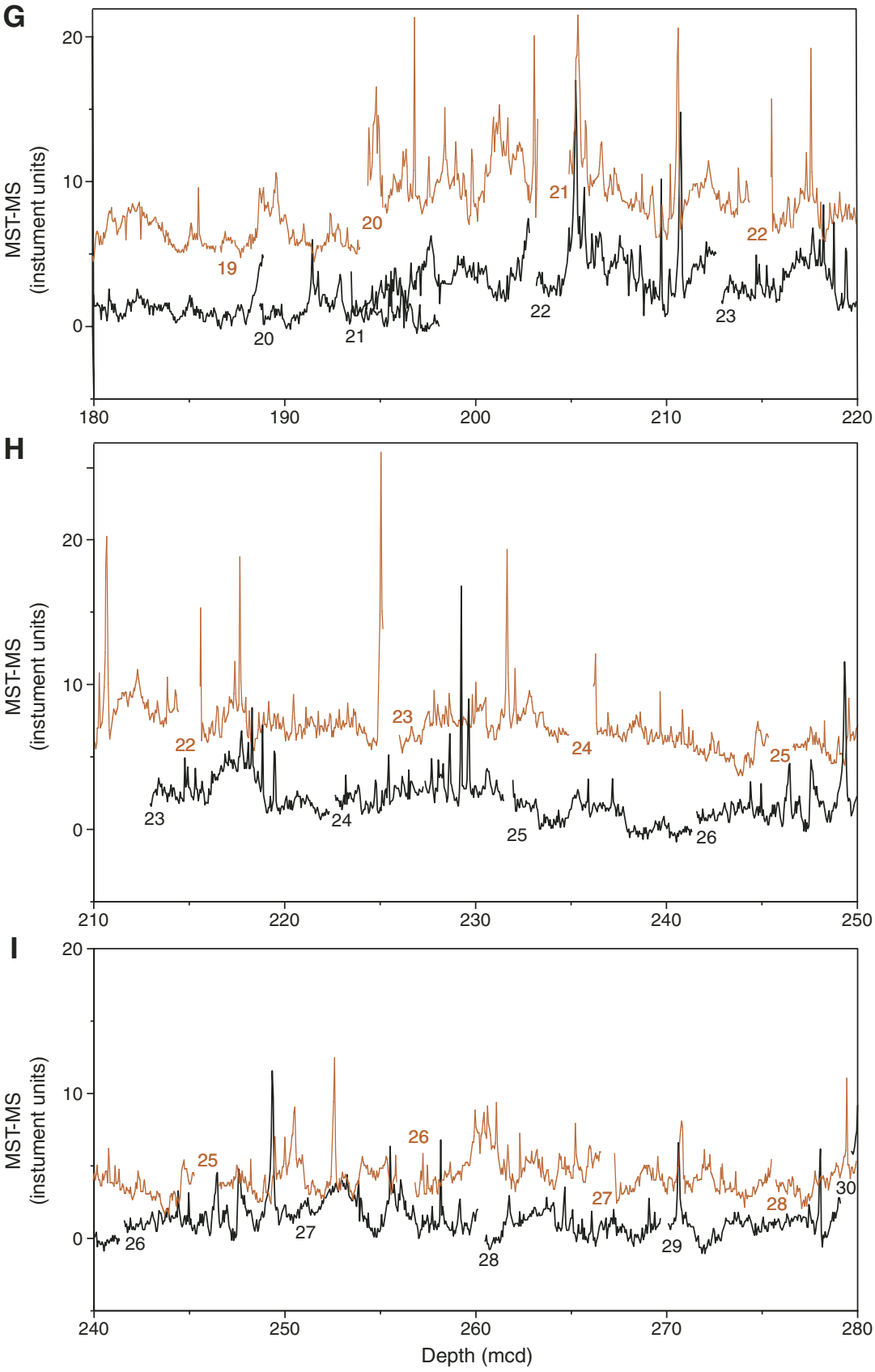

Figure F9 (continued). **J.** 270–310 mcd. **K.** 300–340 mcd. **L.** 330–370 mcd.

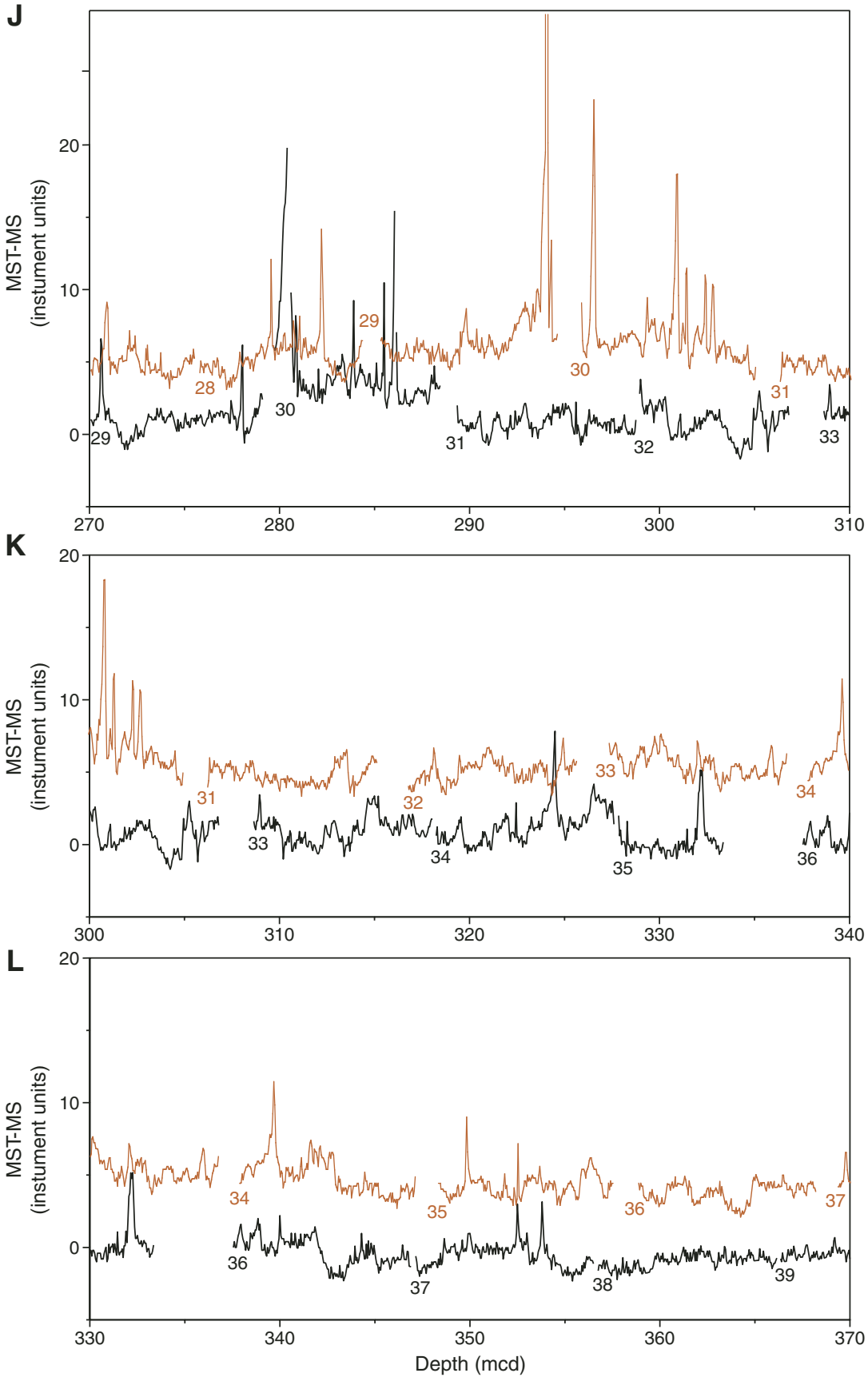

Figure F9 (continued). **M.** 360–400 mcd. **N.** 390–430 mcd. **O.** 420–460 mcd.

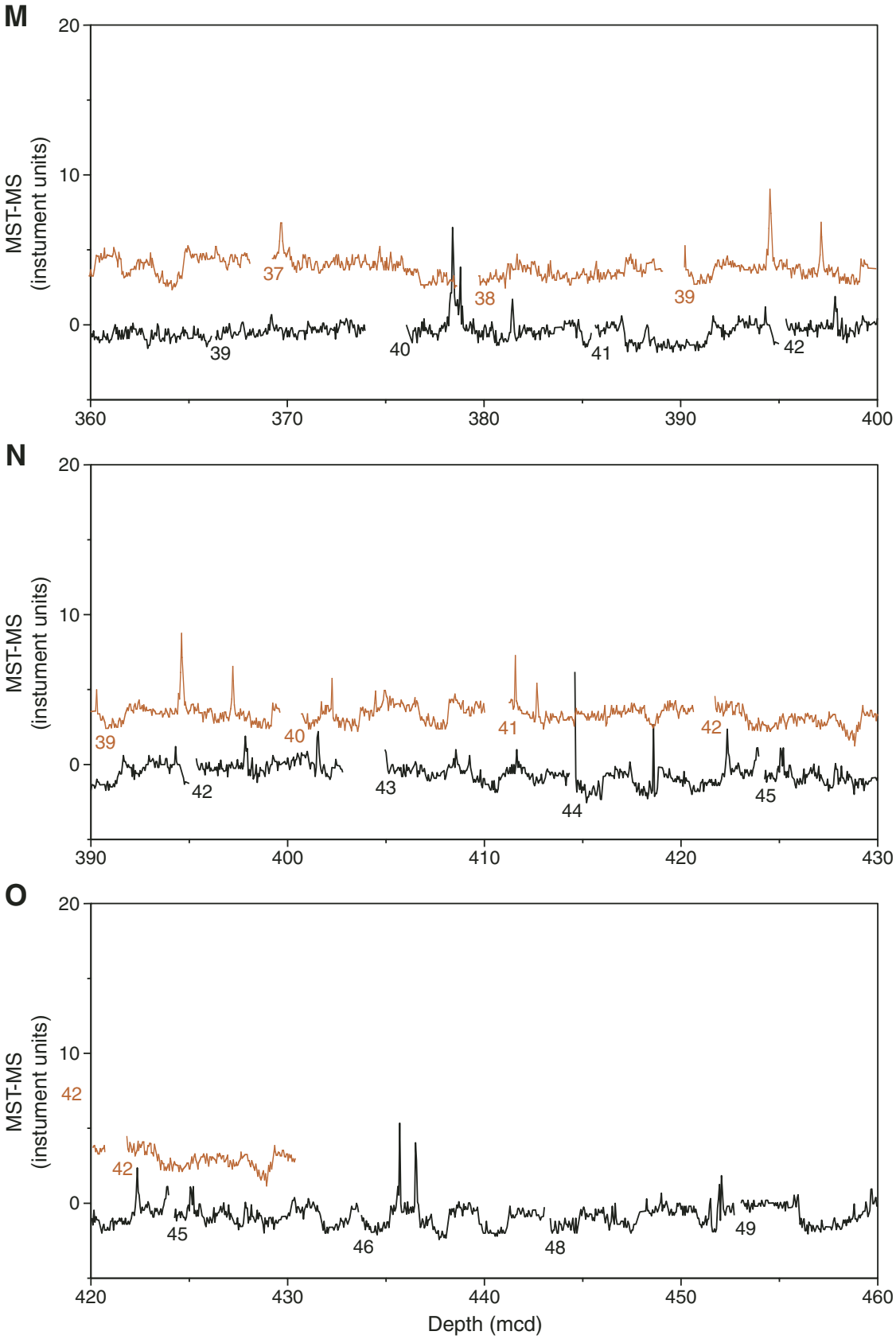

Figure F9 (continued). **P.** 450–490 mcd. **Q.** 480–520 mcd. **R.** 510–550 mcd.

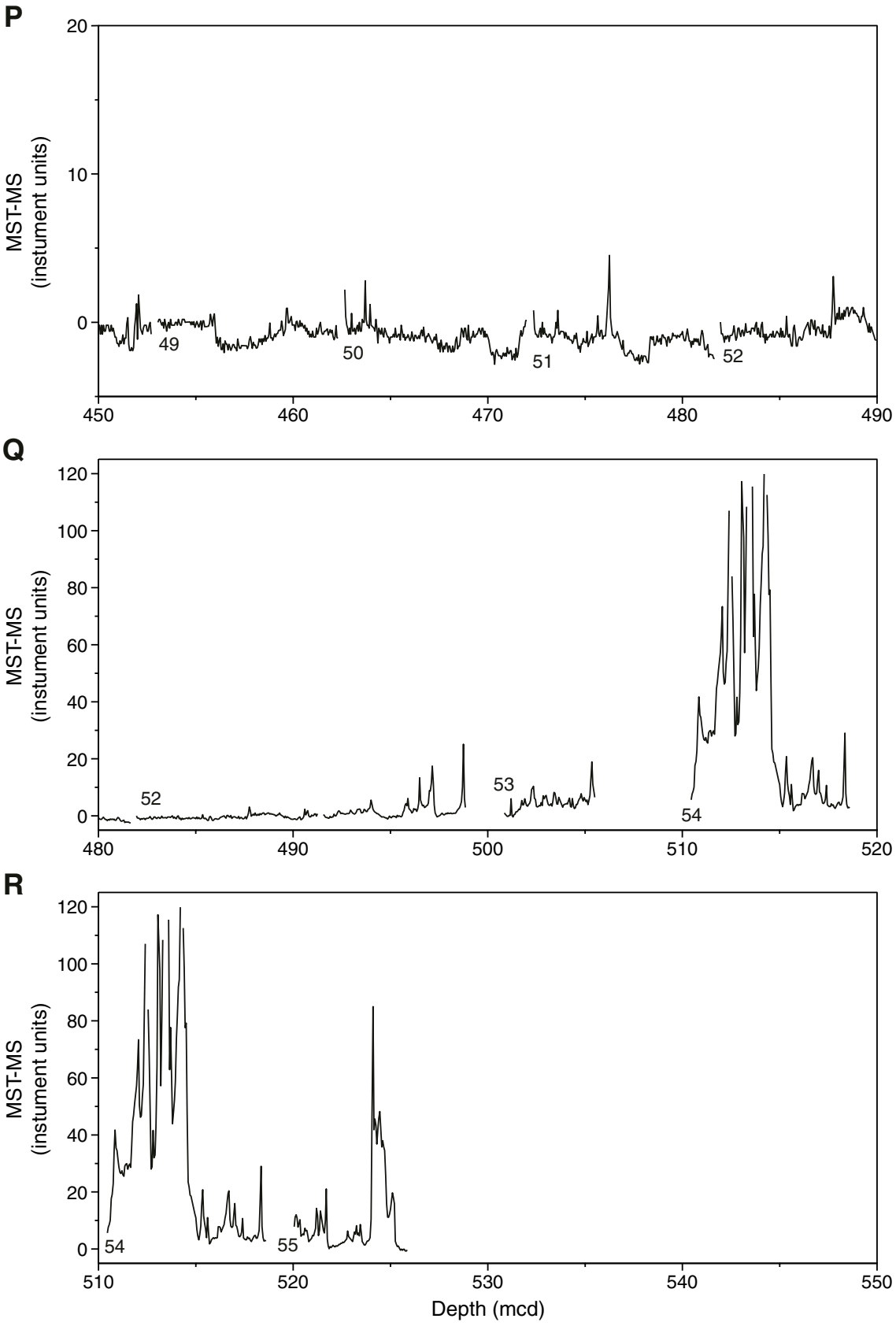

Figure F10. Spliced records of natural gamma radiation (NGR), gamma ray attenuation (GRA) bulk density, and magnetic susceptibility (MST-MS) for Site 1239.

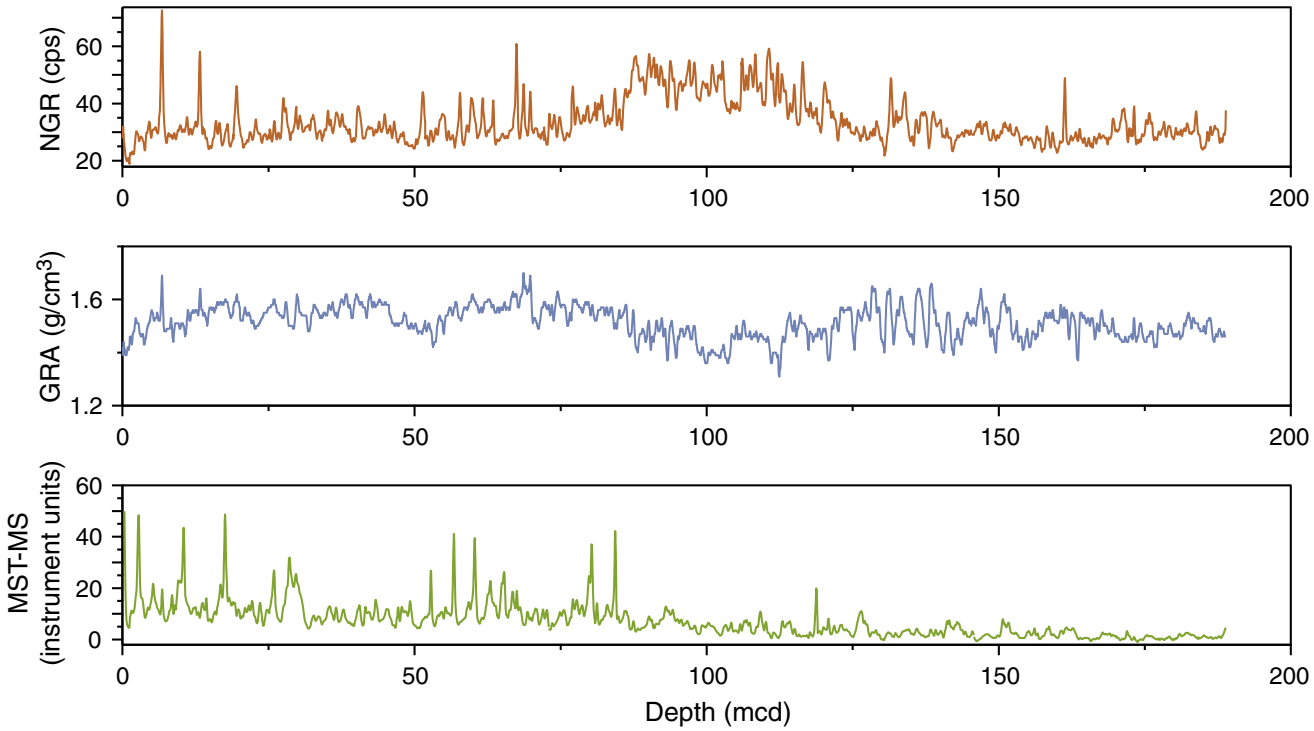

Figure F11. Spliced records of color reflectance from Site 1239: L*, a*, and b*.

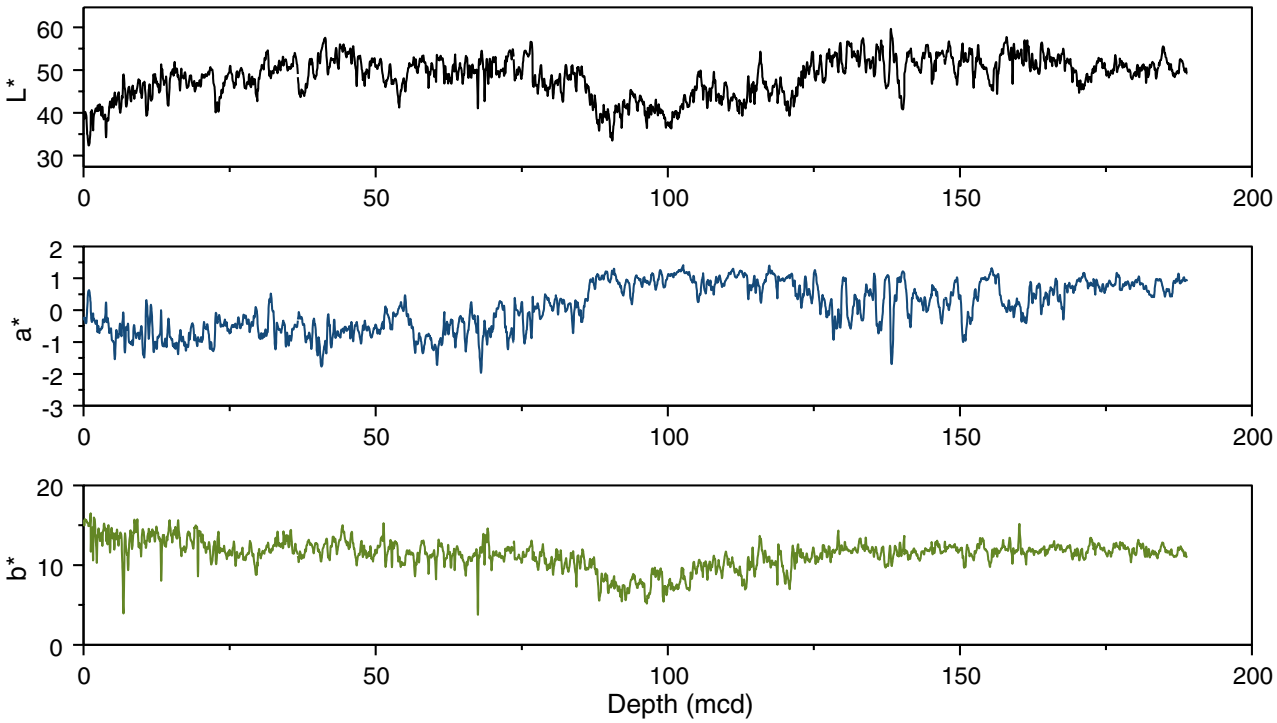

Figure F12. A comparison of the drillers depth (mbsf) and meters composite depth (mcd) scales in Holes 1239A through 1239C. On average, mcd is 8% greater than mbsf in the splice. The 1:1 (mbsf:mcd) line is also shown for comparison. GF = growth factor.

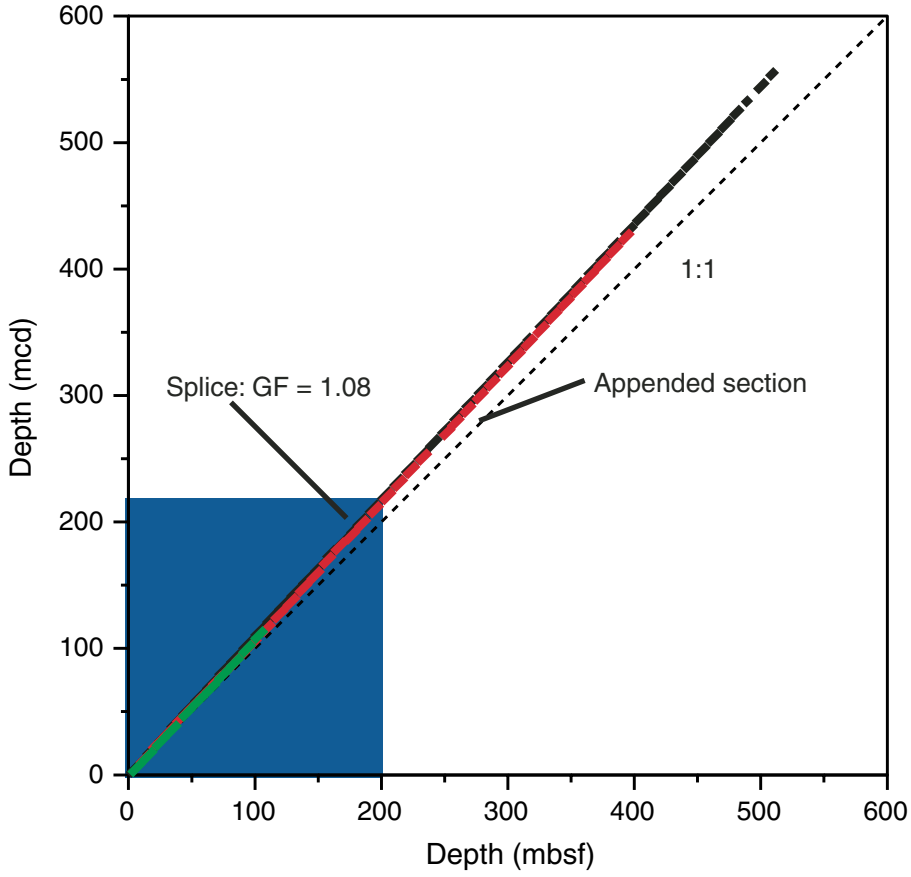

Figure F13. A comparison in Hole 1239A of downhole natural gamma radiation (HSGR) with whole-core natural gamma radiation (NGR) and of downhole log bulk density (RHOM) with whole-core gamma ray attenuation (GRA) bulk density. Log and core data are placed on the estimated log depth (eld) scale for comparison.

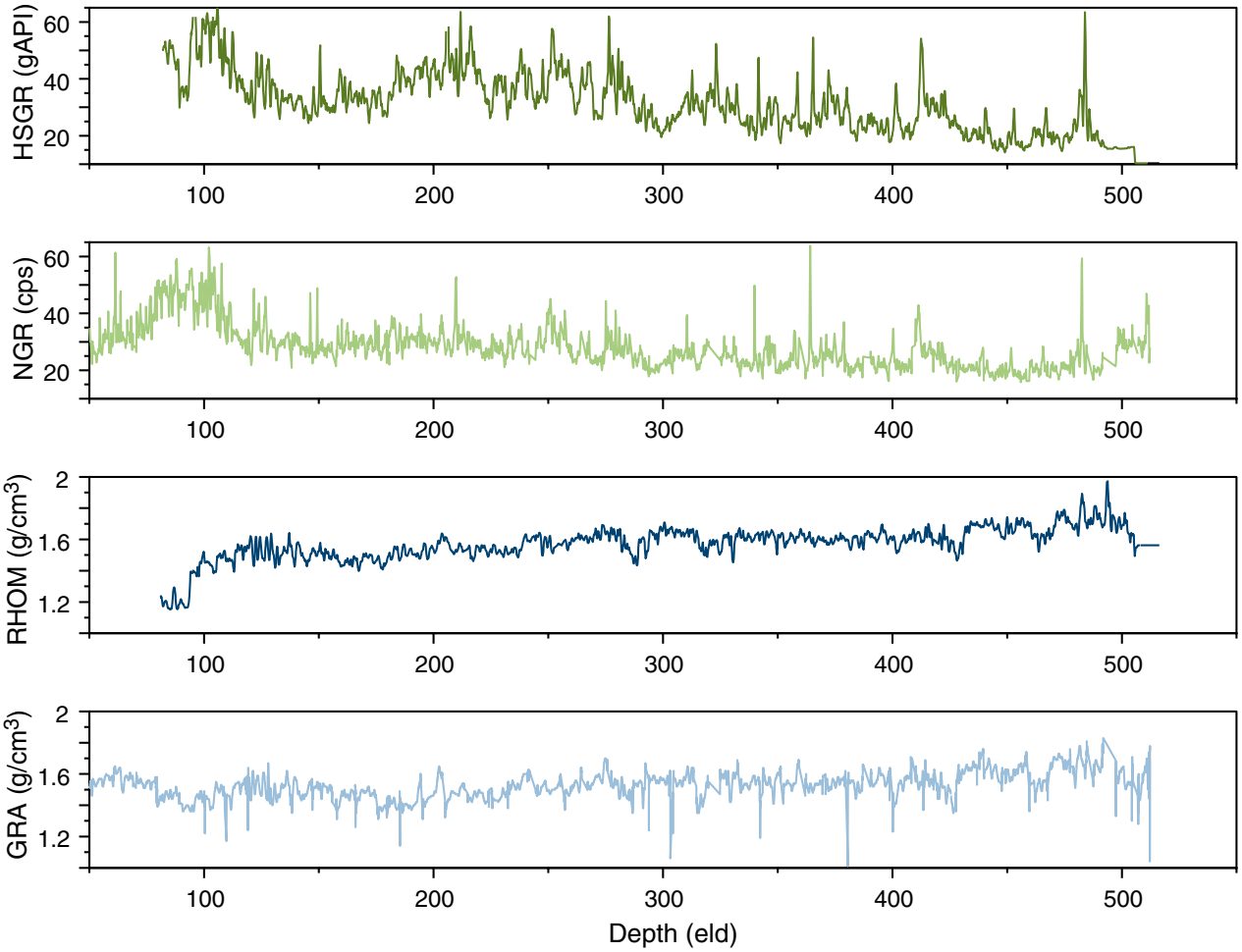

Figure F14. Core recovery, lithostratigraphic unit, age, ash layers, magnetic susceptibility, gamma ray attenuation (GRA) bulk density, natural gamma radiation, color reflectance (L*), calcium carbonate, and total organic carbon (TOC) of recovered sediments from Site 1239. Gray lines show the original data, and black lines are 50-point smoothing averages of the original data. Gray diamonds = ash layer presence, black diamonds = ash layers correlative between Holes 1239A, 1239B, and 1239C.

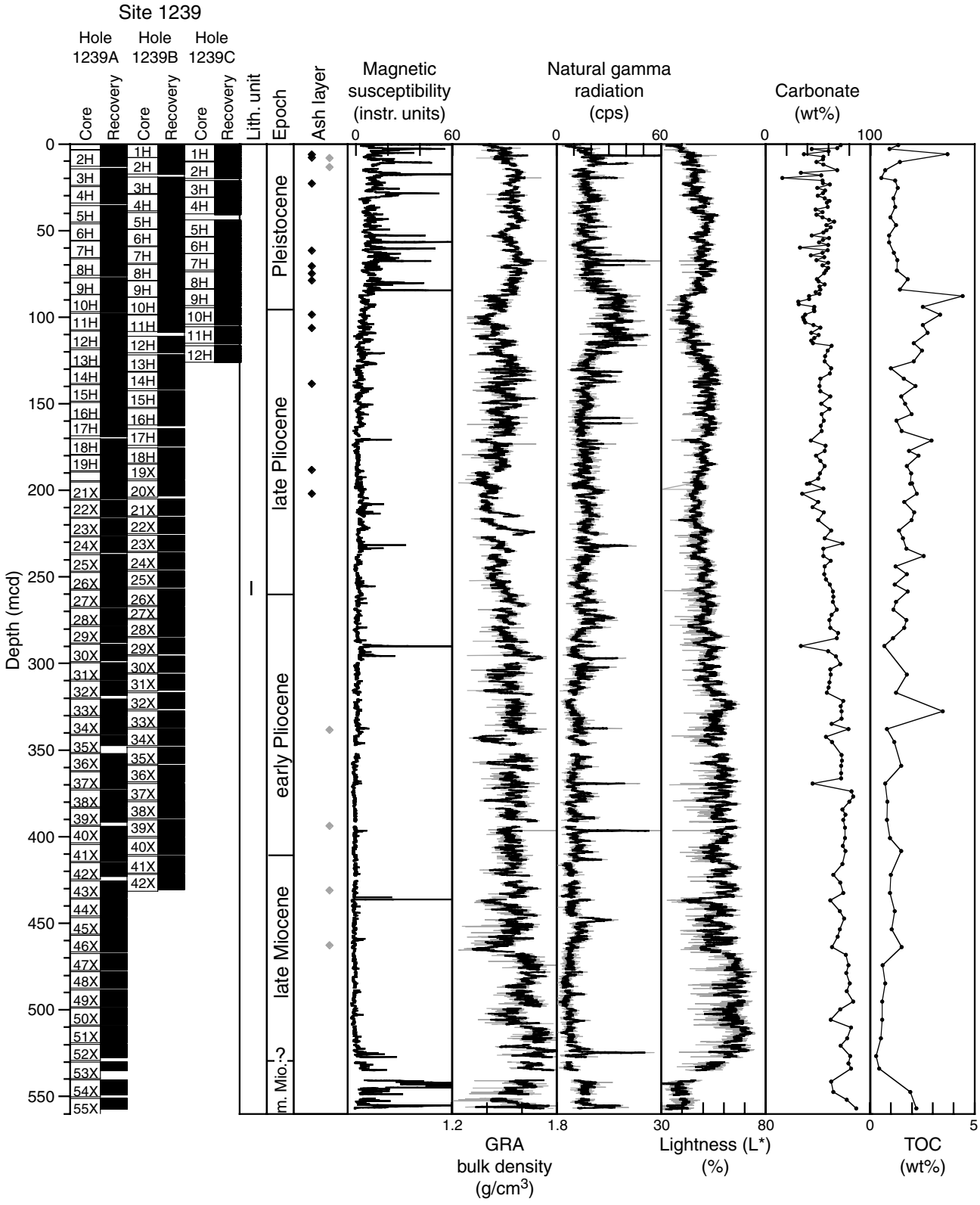

Figure F15. Major components observed in Hole 1239A smear slides. Rad. = radiolarians, Silicof. = silicoflagellates. MS = magnetic susceptibility. TOC = total organic carbon.

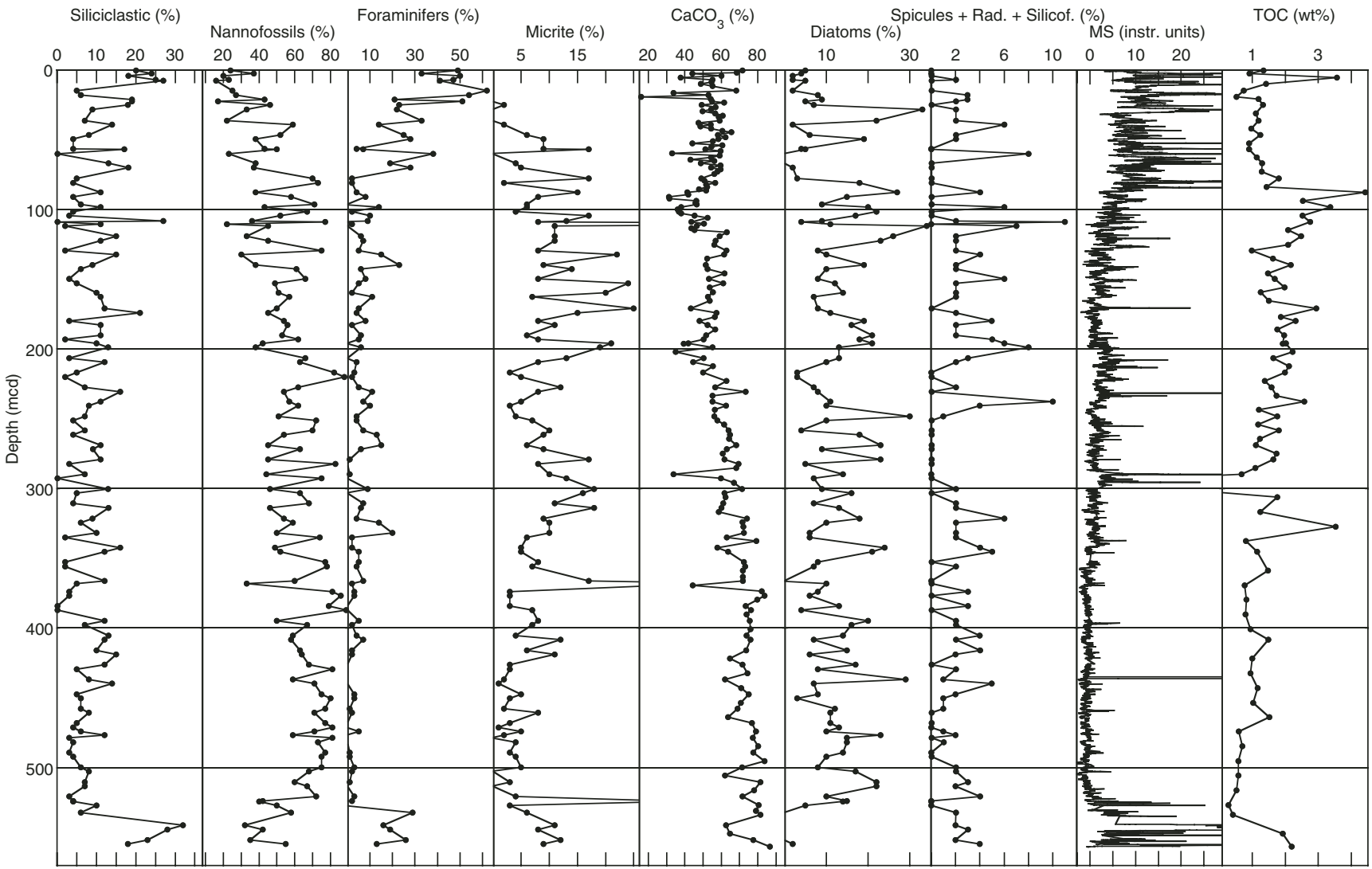

Figure F16. Close-up photograph of representative bioturbated intervals with mottles, burrows, and *Zoophycos* (interval 202-1239A-34X-2, 26–49 cm).

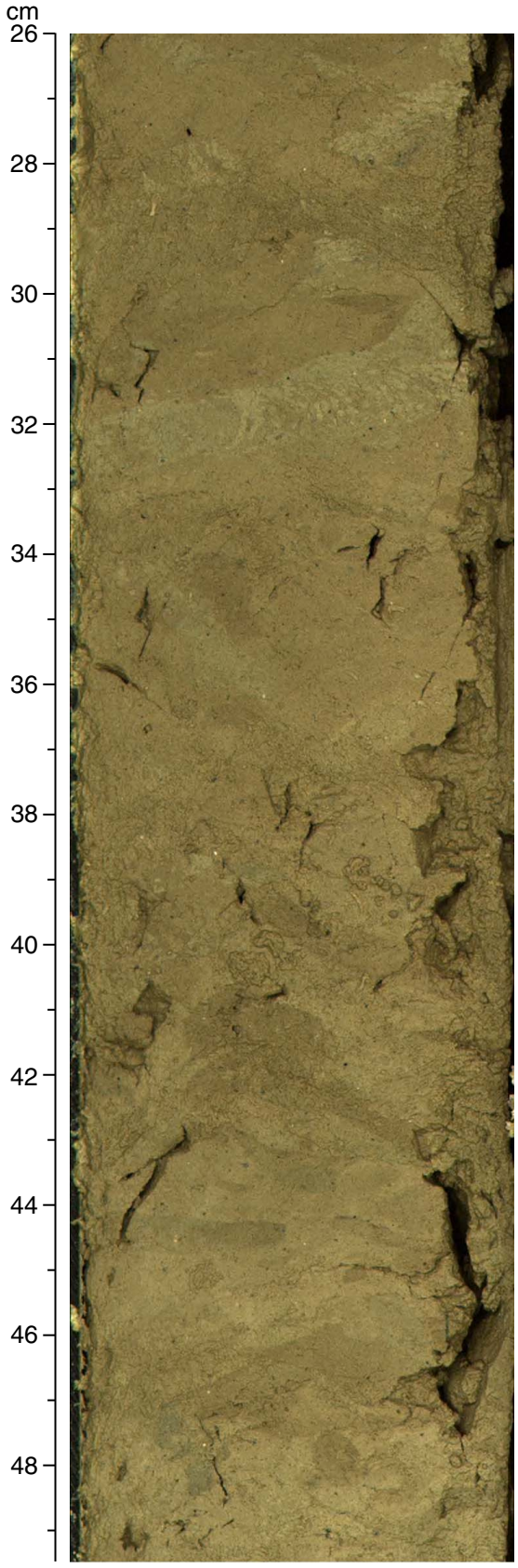

Figure F17. Close-up photograph of representative ash layers found at Site 1239 in interval 202-1239A-8H-1, 92–124 cm (ash layers are between 107 and 113 cm and 114.5 and 119 cm) and in interval 202-1239A-34X-5, 20–35 cm (ash layer is between 29 and 31 cm).

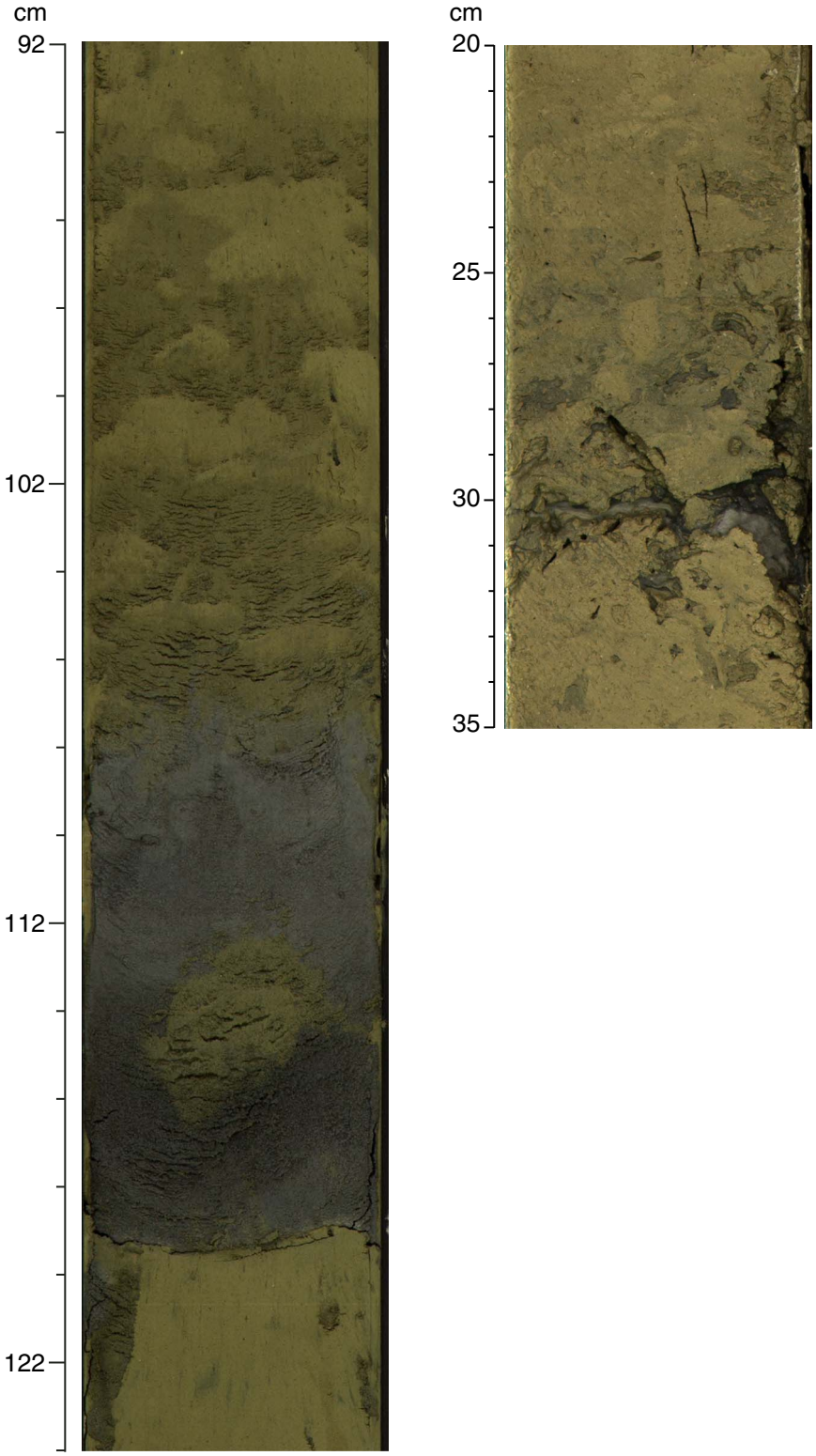

Figure F18. Physical properties measurements for Site 1239. **A.** Gamma ray attenuation (GRA) bulk density and moisture and density (MAD). **B.** Porosity. **C.** Grain density. **D.** Correlation between interpolated GRA and discrete MAD bulk density measurements. **E.** Correlation between MAD bulk density and porosity. **F.** Correlation between $CaCO_3$ and grain density.

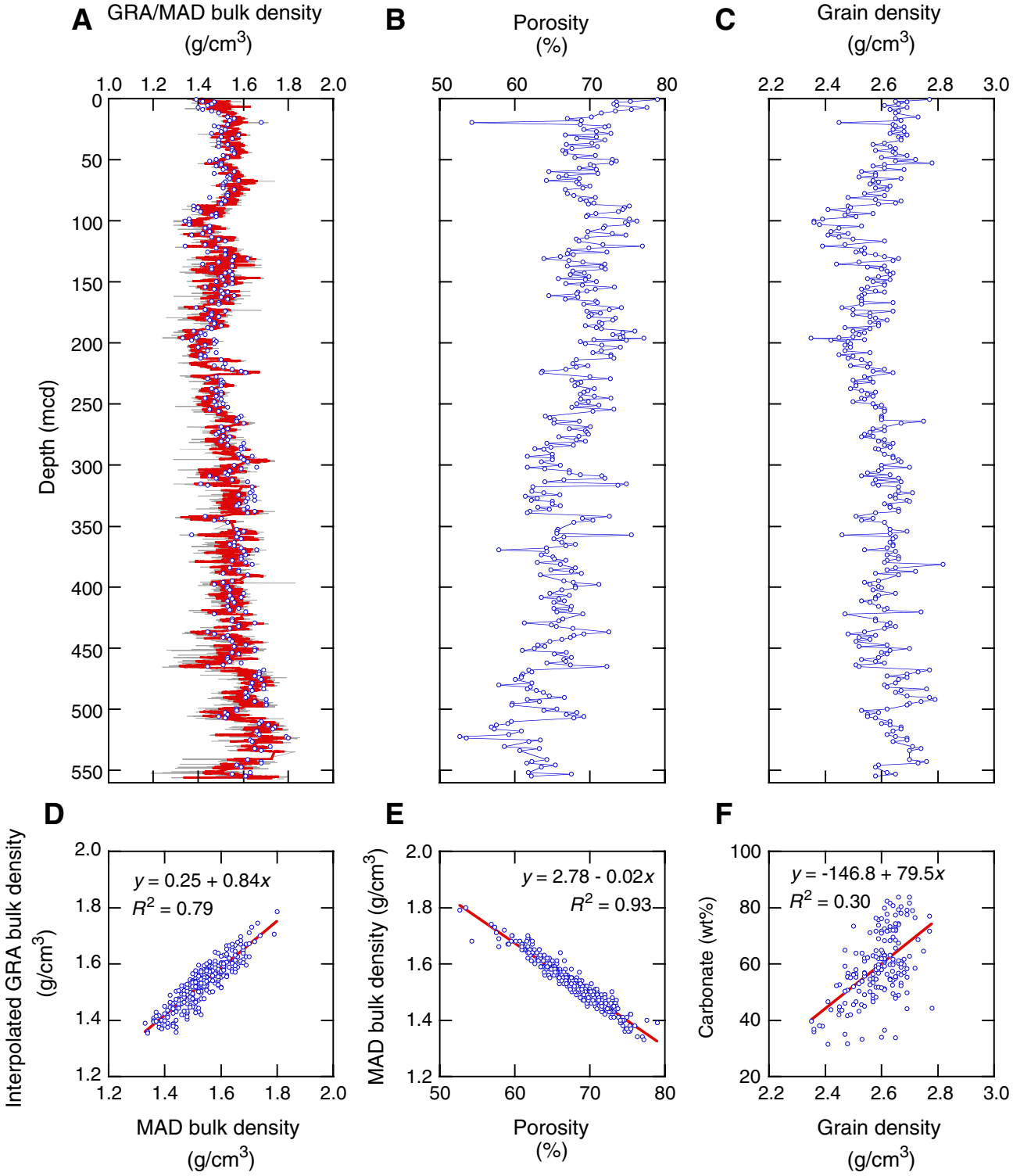

Figure F19. Color measurements at Site 1239 plotted in the a*-b* color plane.

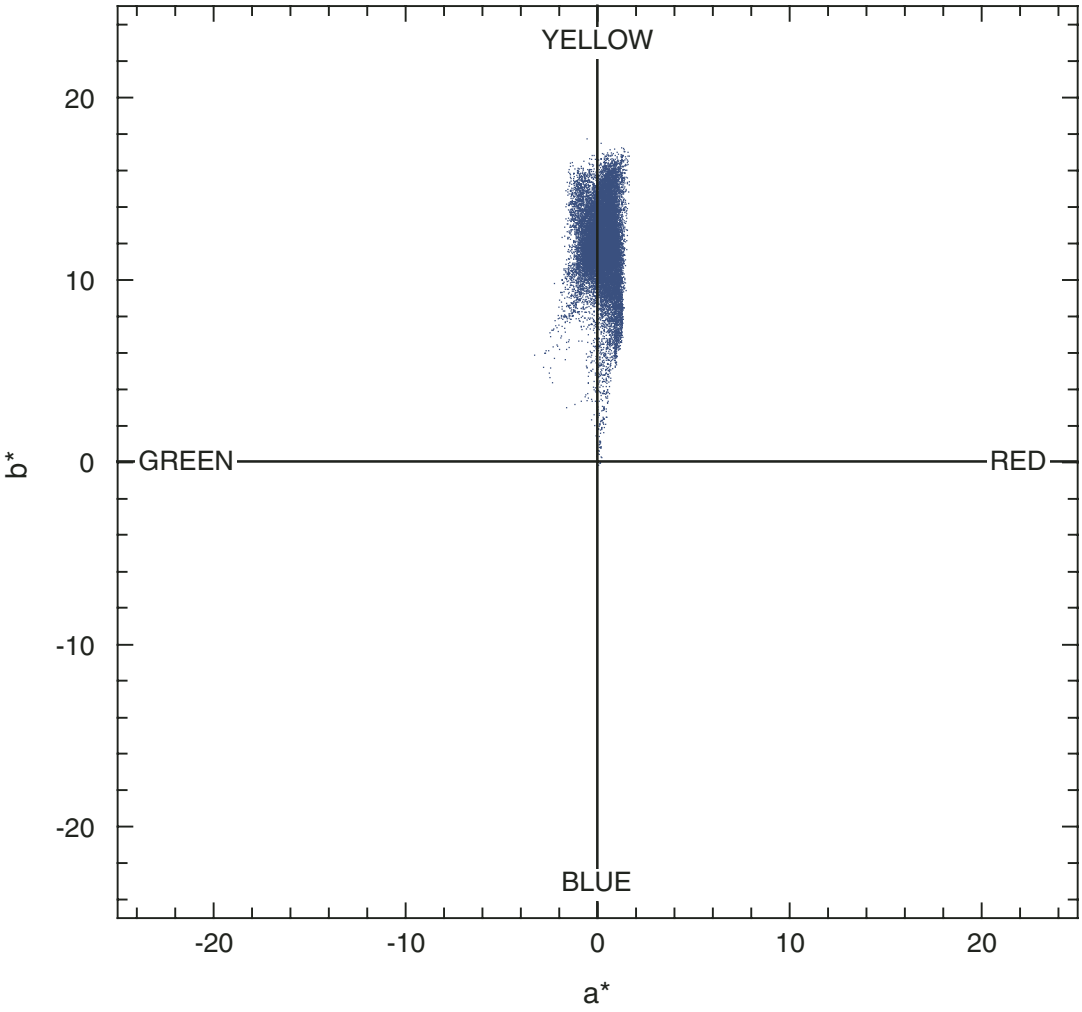

Figure F20. A. Sequential depth plot of raw reflectance spectra for Site 1239. **B.** First derivatives of raw reflectance data with respect to wavelength. Red lines = absorption features typical of organic pigments (e.g., at 410, 510, 560, and 650 nm). **C.** The normalized absorption feature at 650 nm, relative to reflectances at 630 and 700 nm and normalized to a measure of the general slope of the spectrum (i.e., $Depth_{650} = \{R_{630} + [3/7 \times (R_{700} - R_{630}) - R_{650}]\}/[R_{700}-R_{400}]$), is plotted with depth as a proxy for abundance of chlorins.

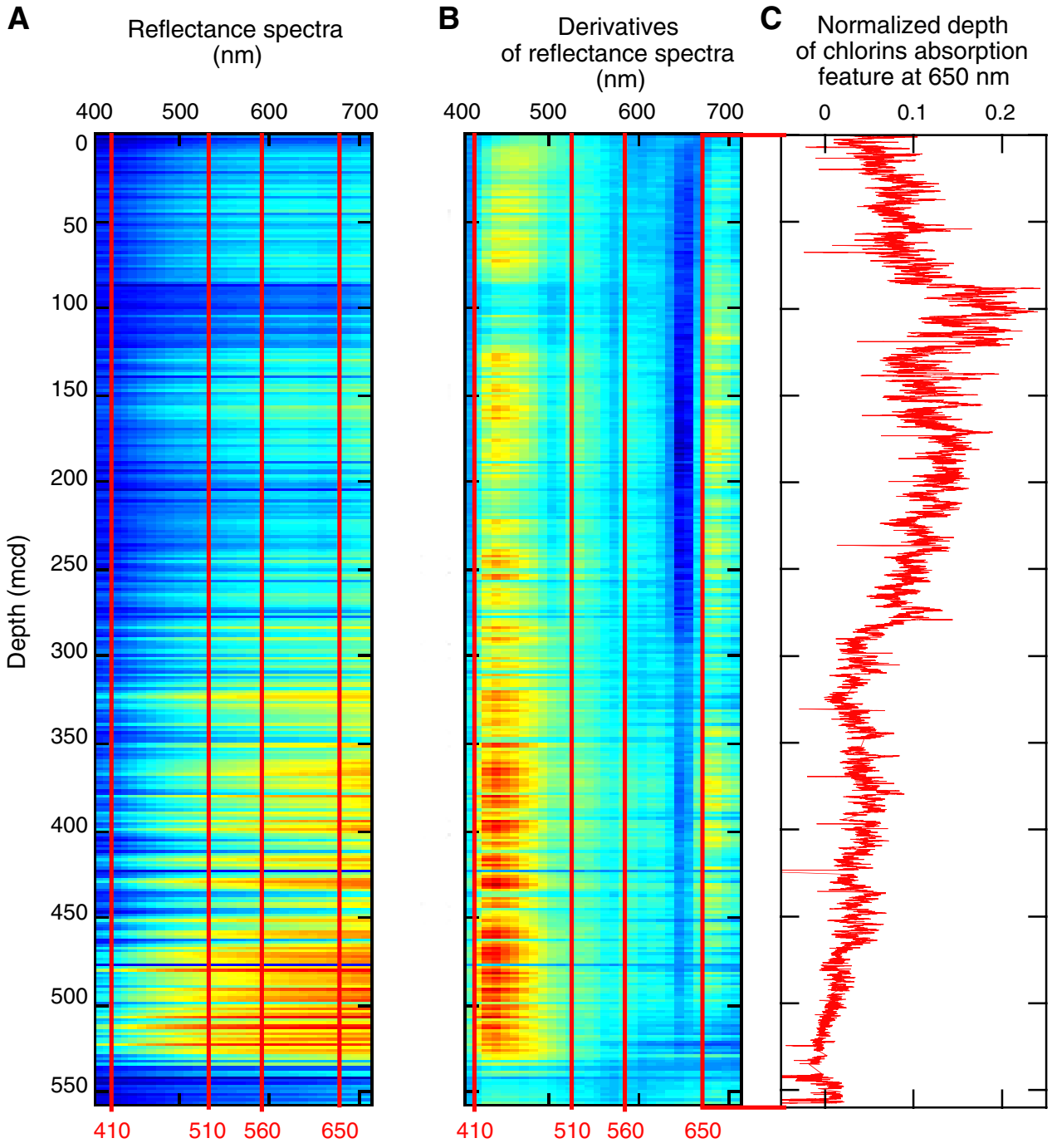

Figure F21. Core recovery, calcareous nannofossils and foraminifer abundance, benthic foraminifer percentage of total foraminifers, and diatom abundance at Hole 1239A (smoothed lines). VA = very abundant, A = abundant, C = common, F = few, R = rare, T = trace, B = barren.

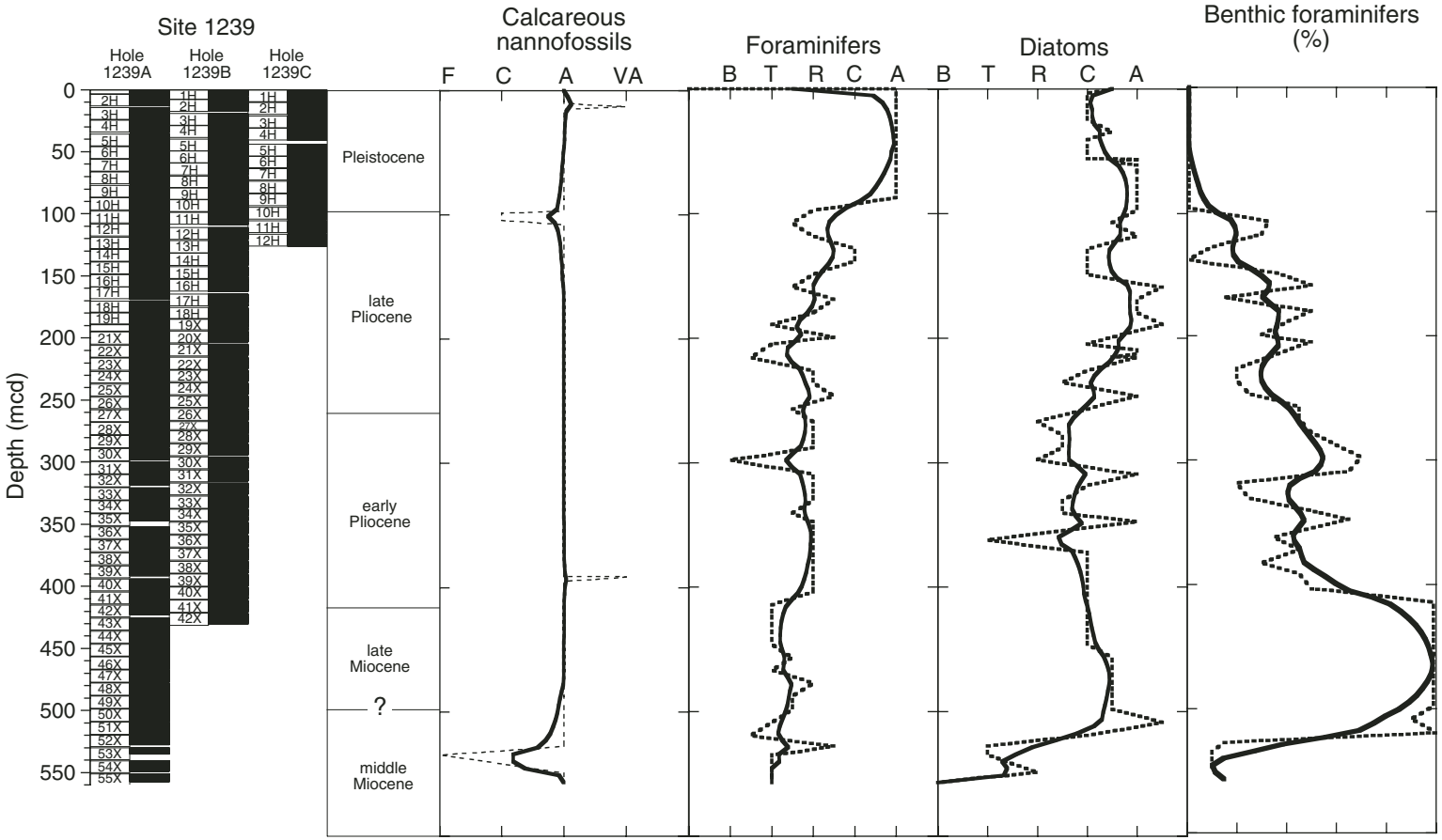

Figure F22. Natural remanent magnetization (NRM) intensities before and after AF demagnetization at 25 mT for Holes 1239A, 1239B, and 1239C. Note the increased noise below 190 mcd, where drilling changed from the APC to the XCB.

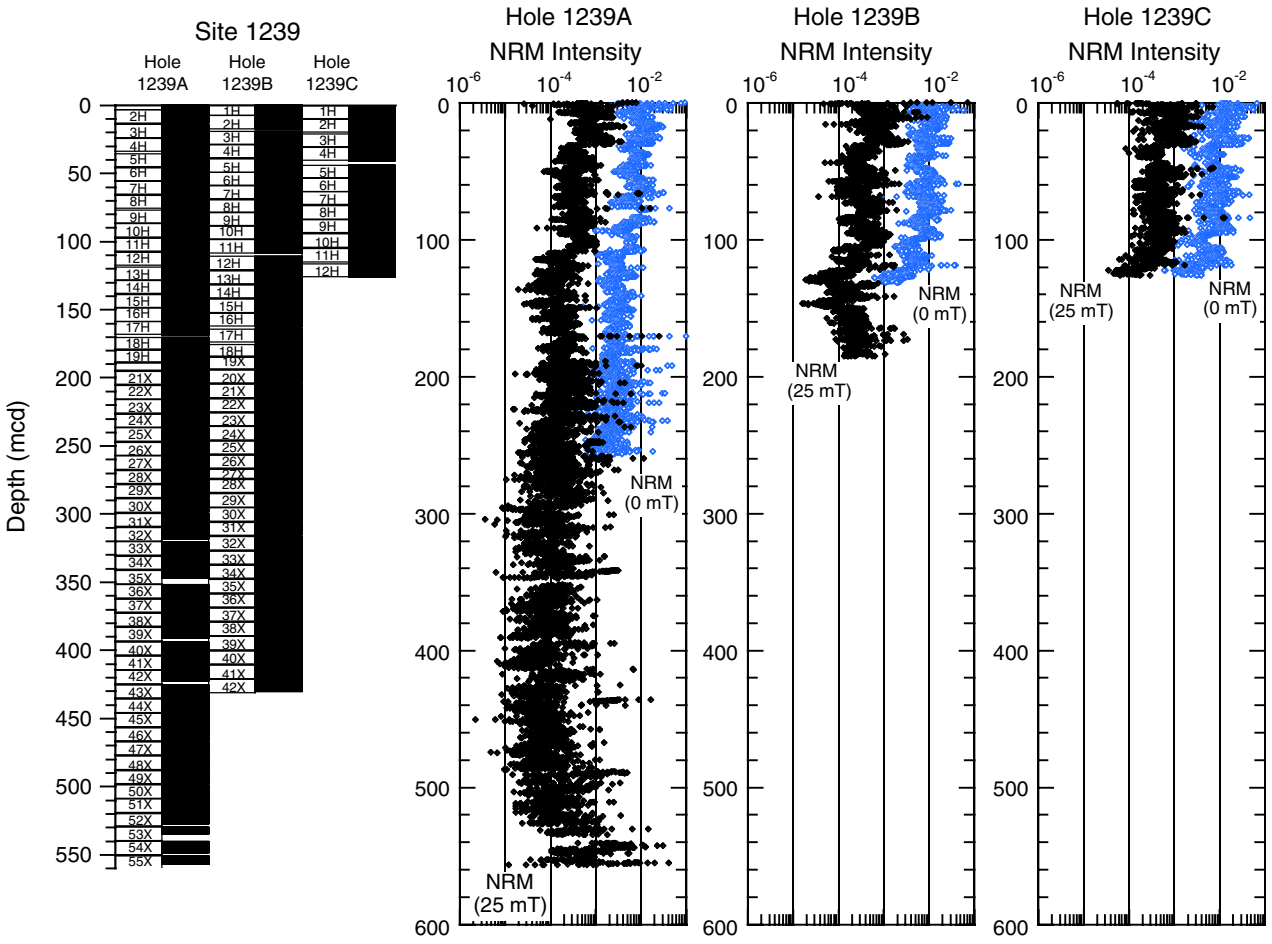

Figure F23. Natural remanent magnetization (NRM) intensity before and after AF demagnetization at 25 mT for the upper 10 mcd of Hole 1239A. Note the large (95%) decrease in intensity within the first meter (composite depth).

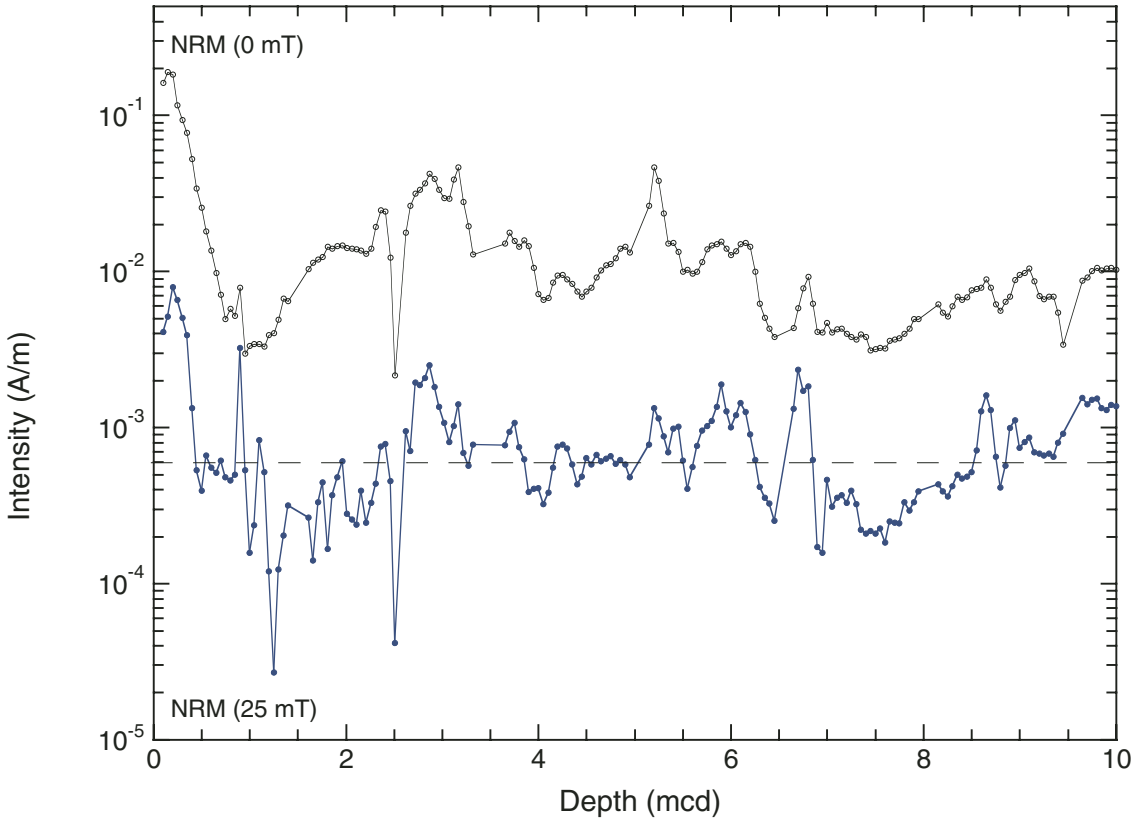

Figure F24. Natural remanent magnetization (NRM) intensity before demagnetization within the upper 140 mcd of (**A**) Hole 1239A and (**B**) Hole 1239B. Individual cores recovered with a normal steel (magnetic) barrel and a nonmagnetic barrel (N-M) are indicated.

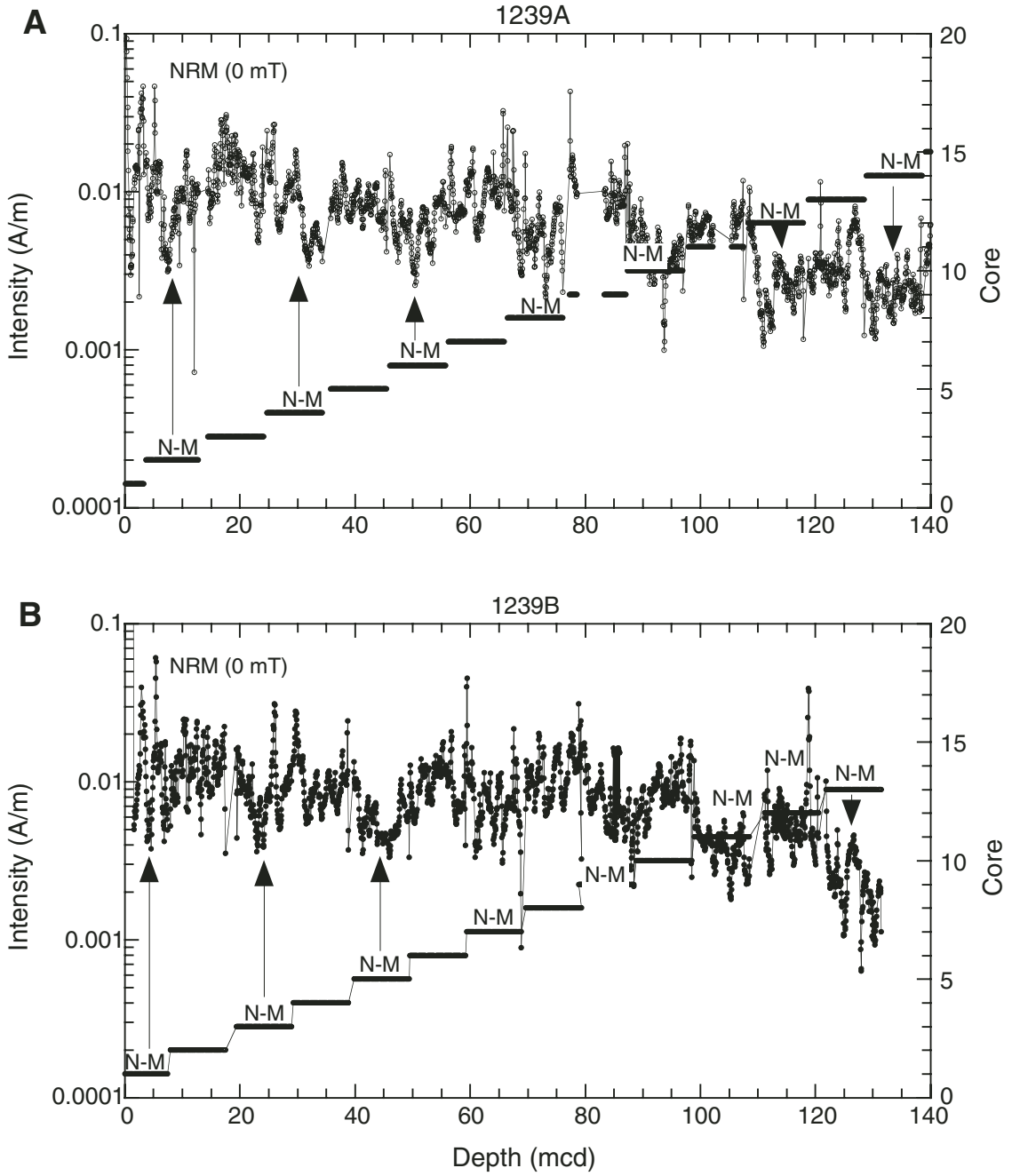

Figure F25. Hole 1239A declinations (top) and inclinations (bottom) after AF demagnetization at 25 mT. Inclinations are near the expected axial dipole expected values (–3.7°) in the uppermost 40 mcd but show a significant continuing overprint for most deeper cores. APC declinations show reasonable within-core correlation, but XCB declinations are essentially random.

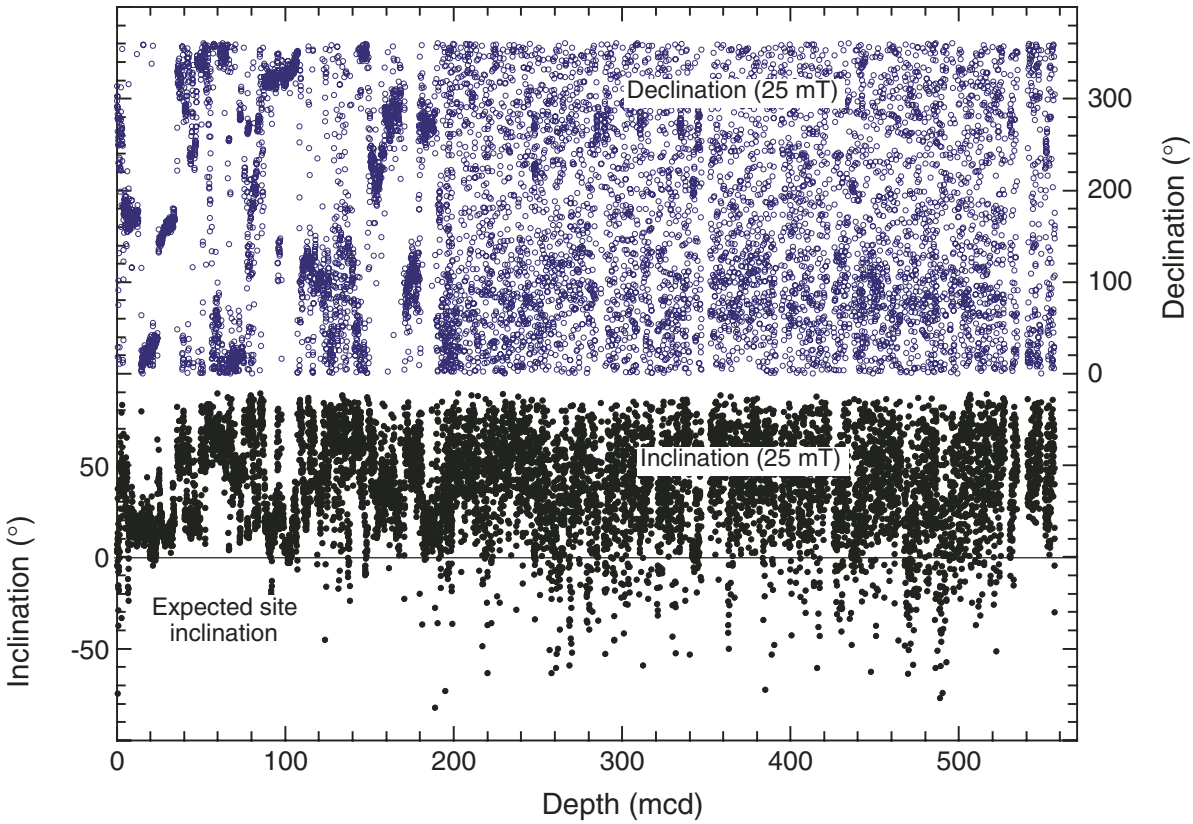

Figure F26. Headspace methane (C_1) concentrations, C_1/C_2 ratios, and CO_2 concentrations vs. depth in sediments for Hole 1239A.

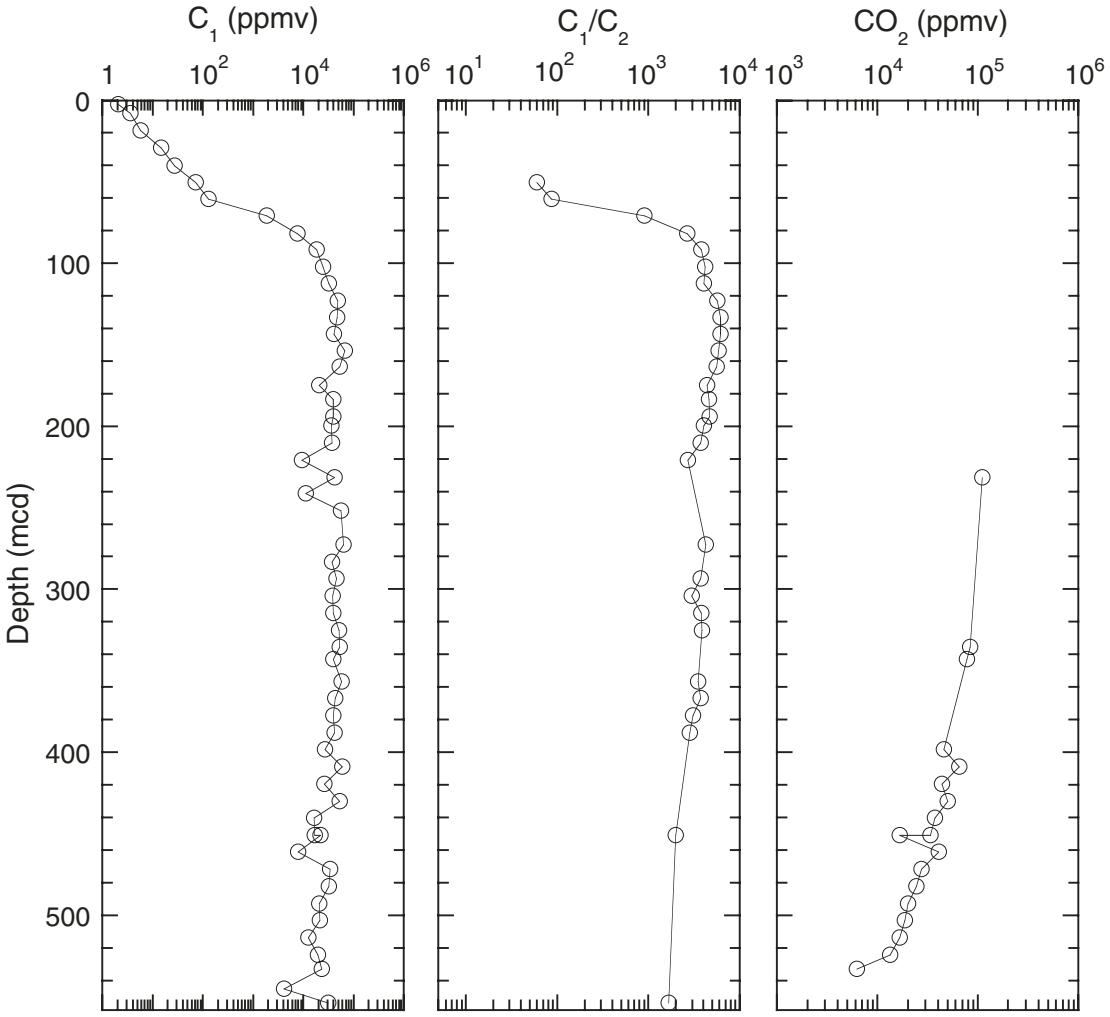

Figure F27. Interstitial water geochemical data for Site 1239. Open squares = calcium concentrations. Values below the detection limit (1.0 mM for sulfate, 0.1 µM for manganese, 0.2 mM for ammonium, and 0.1 µM for barium) are plotted at zero. Note that blank correction for manganese (0.3 µM) was significant compared to most of the measured concentrations, so this profile should be interpreted with caution.

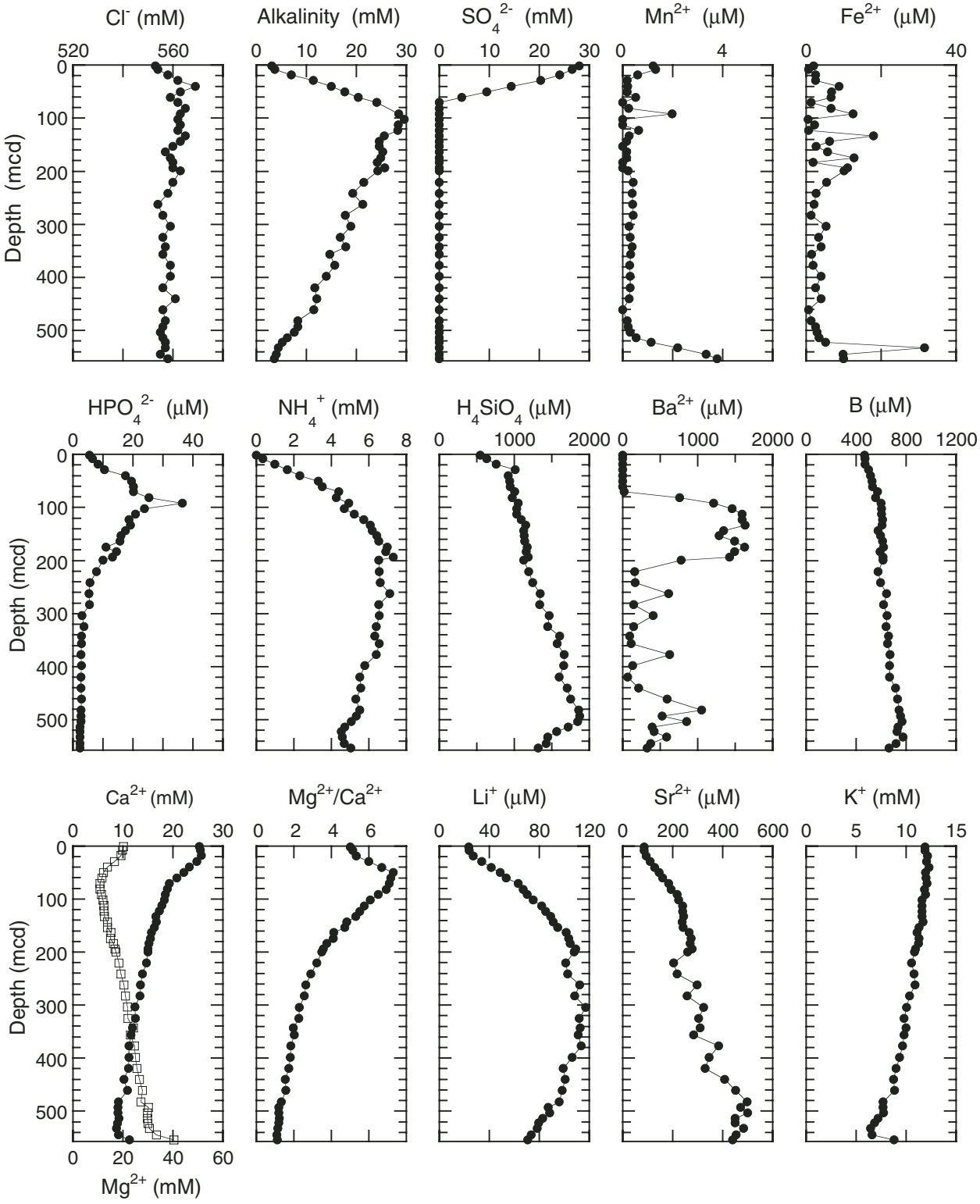

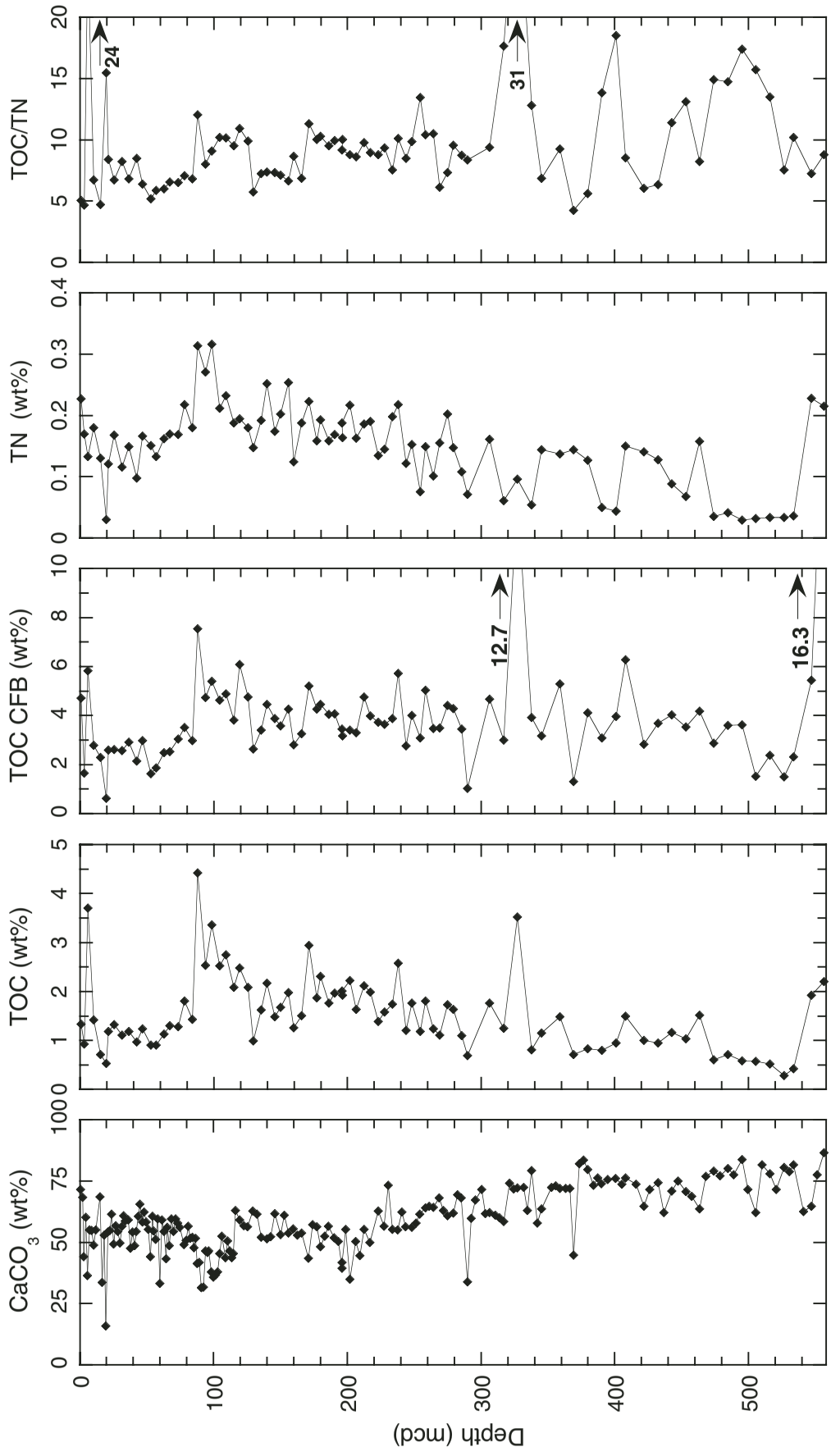

Figure F28. Calcium carbonate ($CaCO_3$), total organic carbon (TOC), TOC on a carbonate-free basis (TOC CFB), and total nitrogen (TN) concentrations, and TOC/TN ratios in sediments vs. depth for Hole 1239A.

Figure F29. Calcium carbonate ($CaCO_3$) vs. total organic carbon (TOC) concentrations and total nitrogen (TN) concentrations vs. TOC contents in sediments of Hole 1239A.

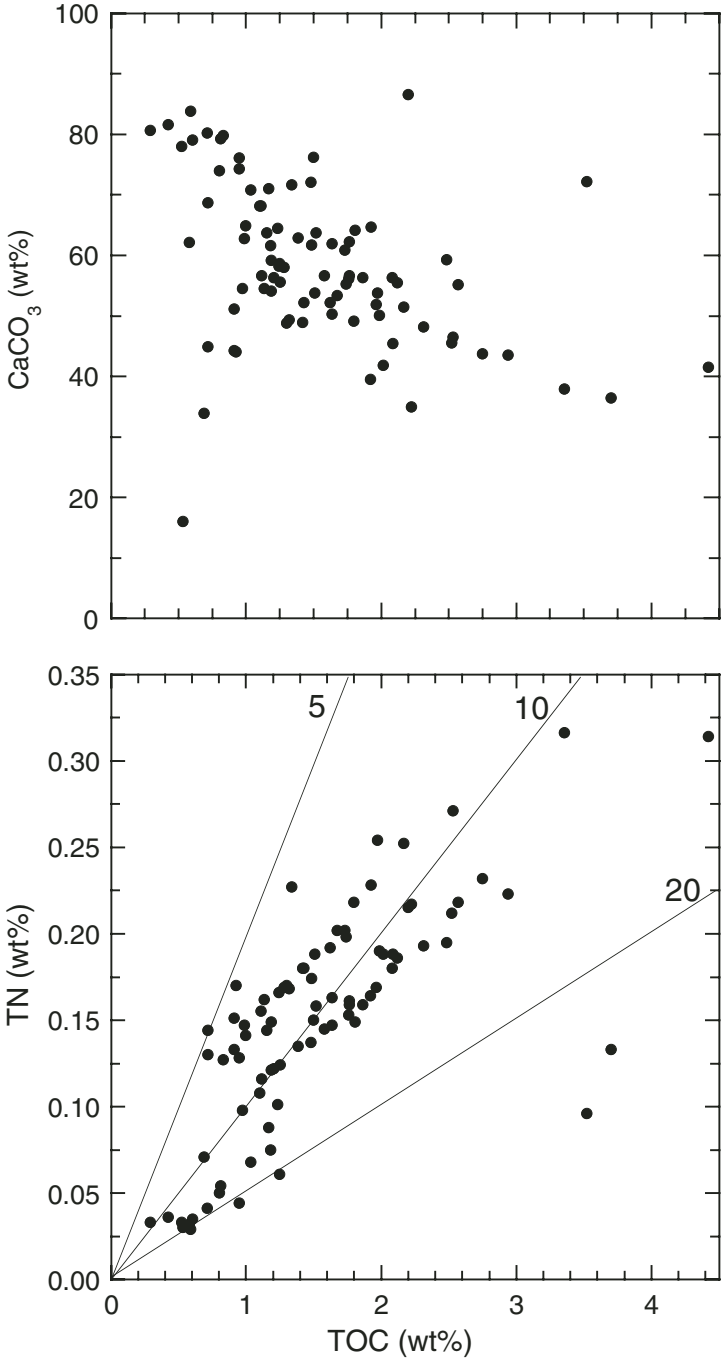

Figure F30. Details of the logging tool string deployments in Hole 1239A. Gray rectangles = drill pipe tools, black rectangles = logging tools. Triple combo = triple combination, MGT = Multi-Sensor Spectral Gamma Ray Tool, FMS = Formation MicroScanner.

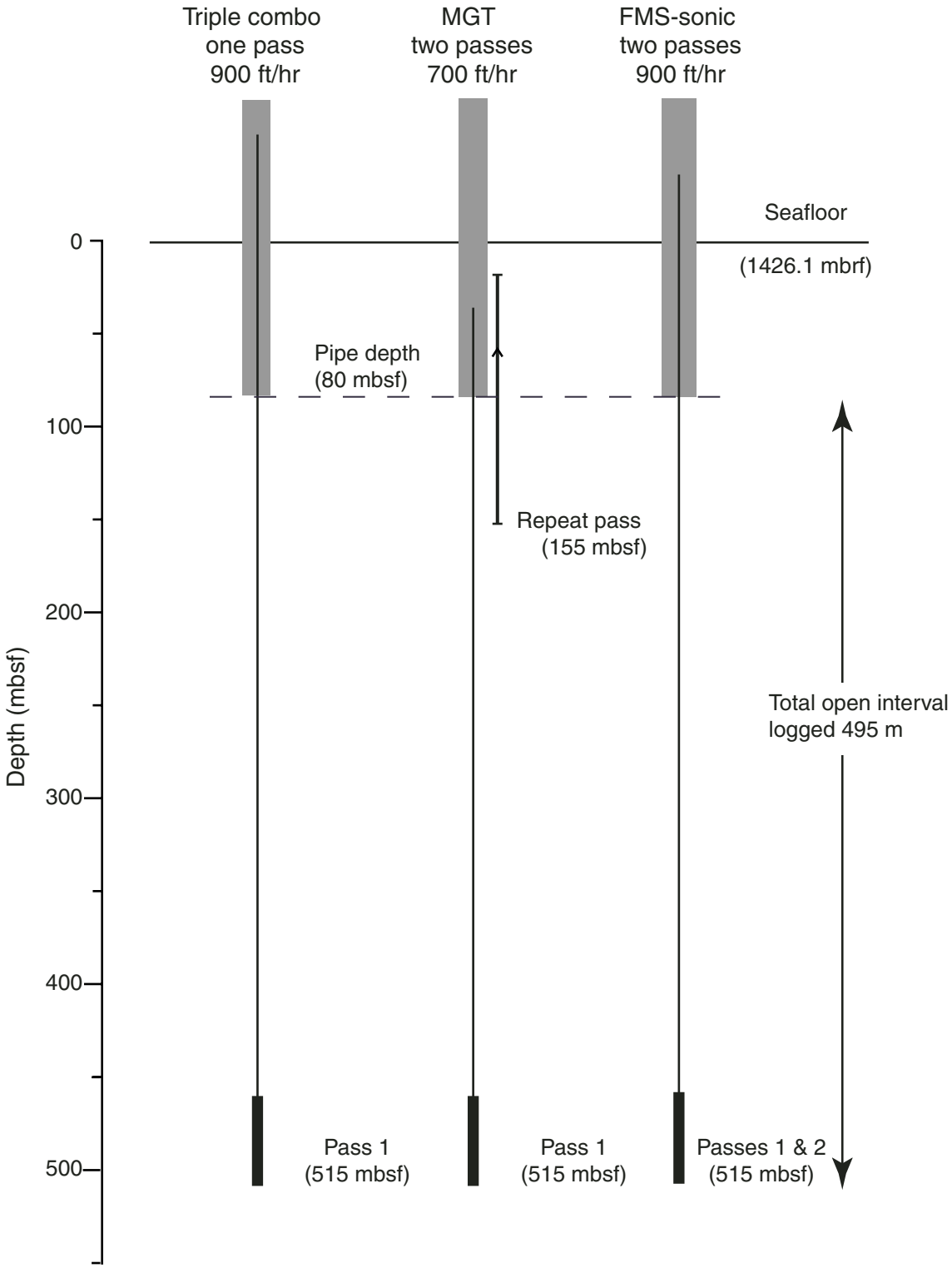

Figure F31. Caliper, deviation, gamma ray, and high-resolution gamma ray records, Hole 1239A.

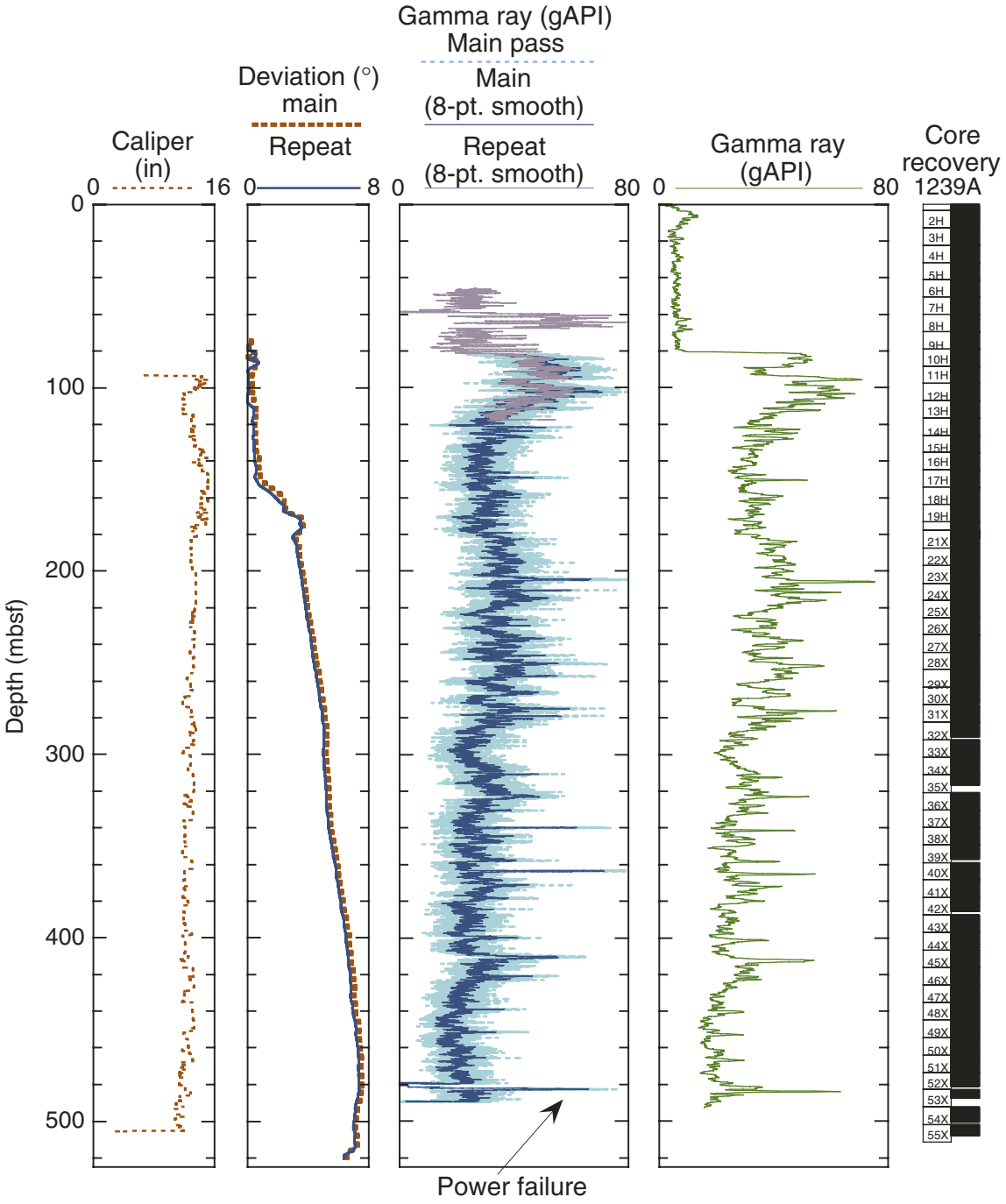

Figure F32. Density, porosity, sonic velocity, and resistivity data for Hole 1239A.

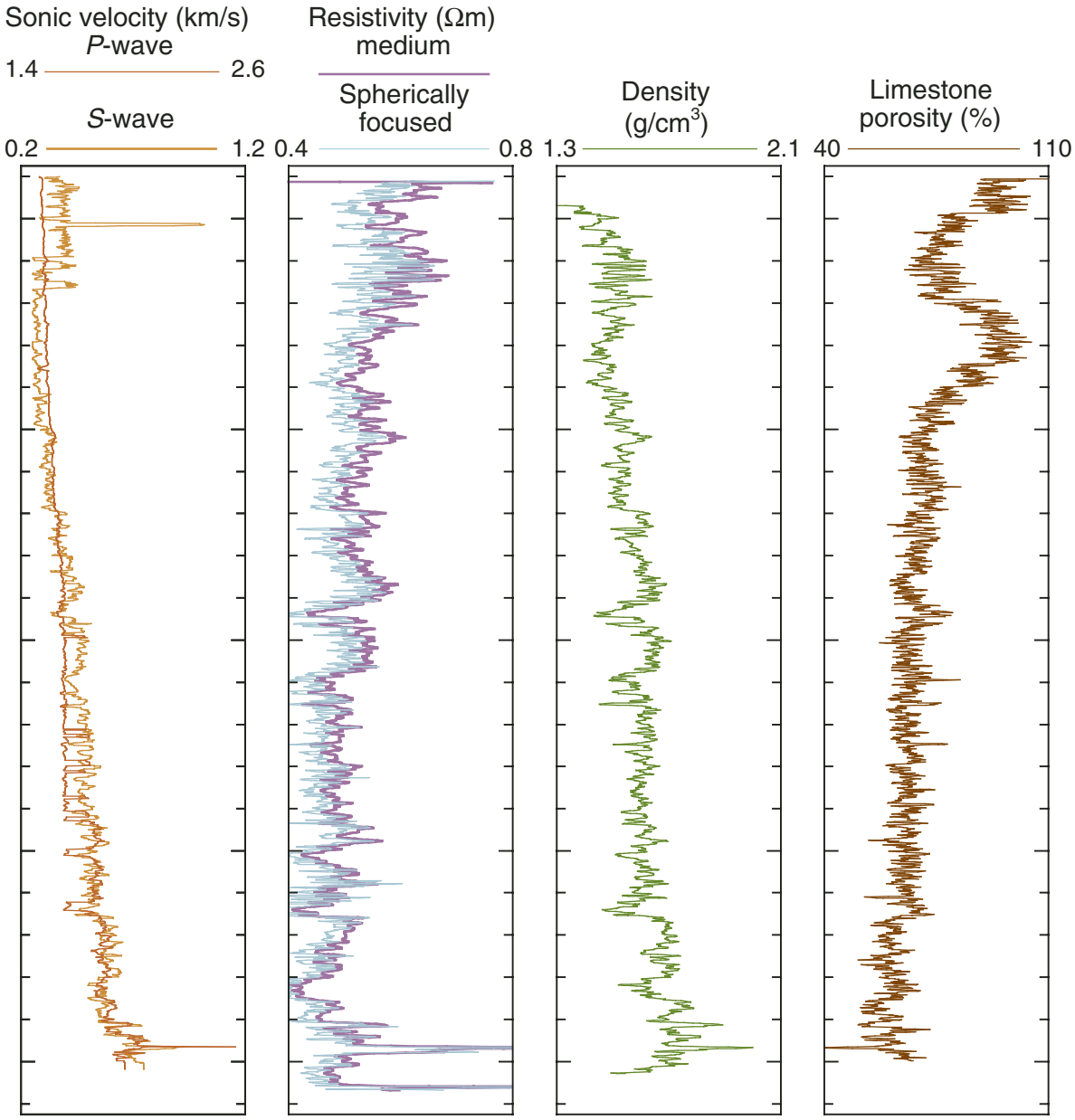

Figure F33. Downhole gamma ray attenuation (GRA) density plotted with core density against Sagan-derived equivalent log depth (eld) for Hole 1239A. **A.** Total interval. **B.** 110–140 m (eld). **C.** 400–430 m (eld).

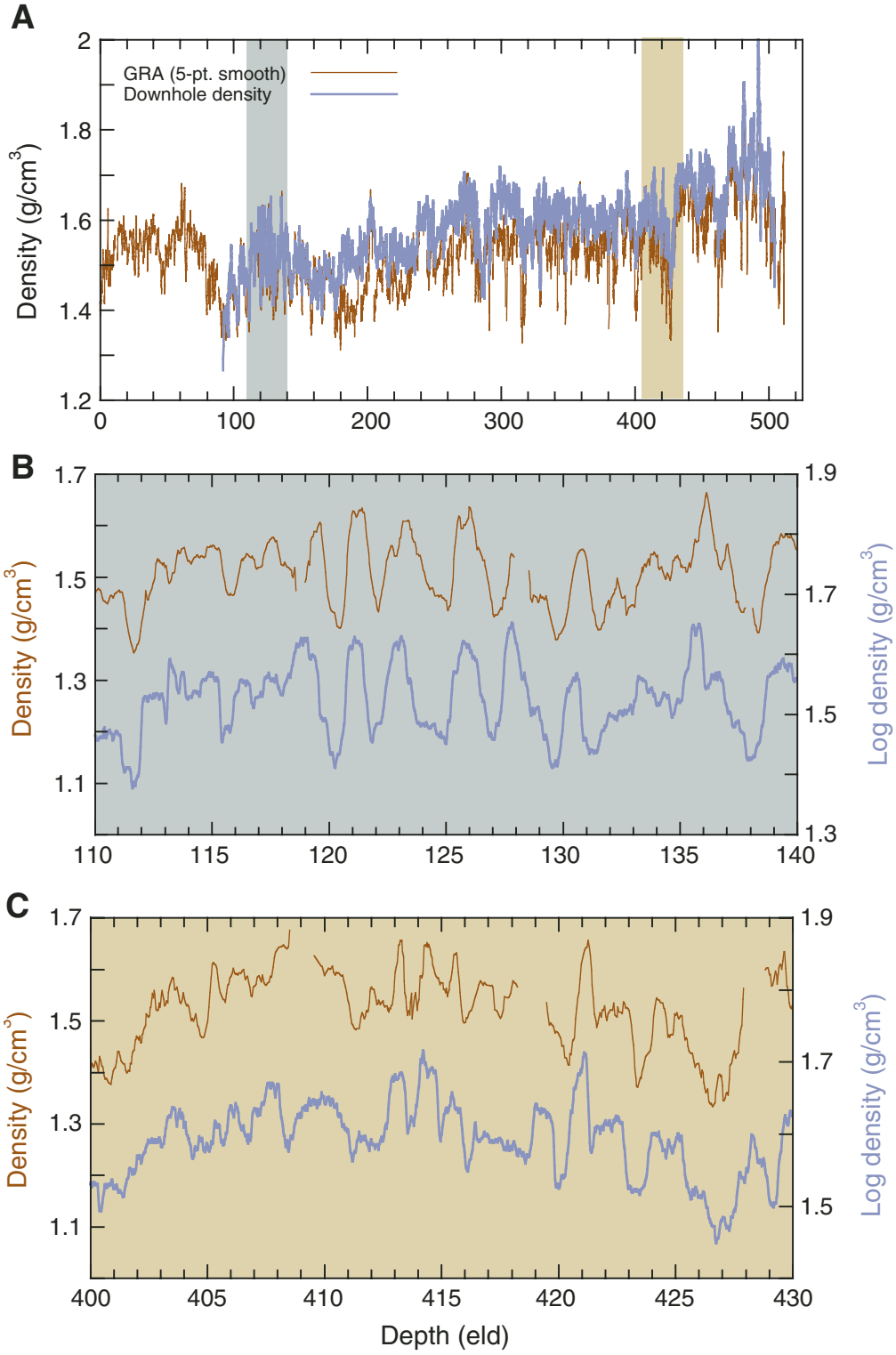

Figure F34. Downhole natural gamma ray activity and core natural gamma ray activity plotted against Sagan-derived equivalent log depth (eld) for Hole 1239A.

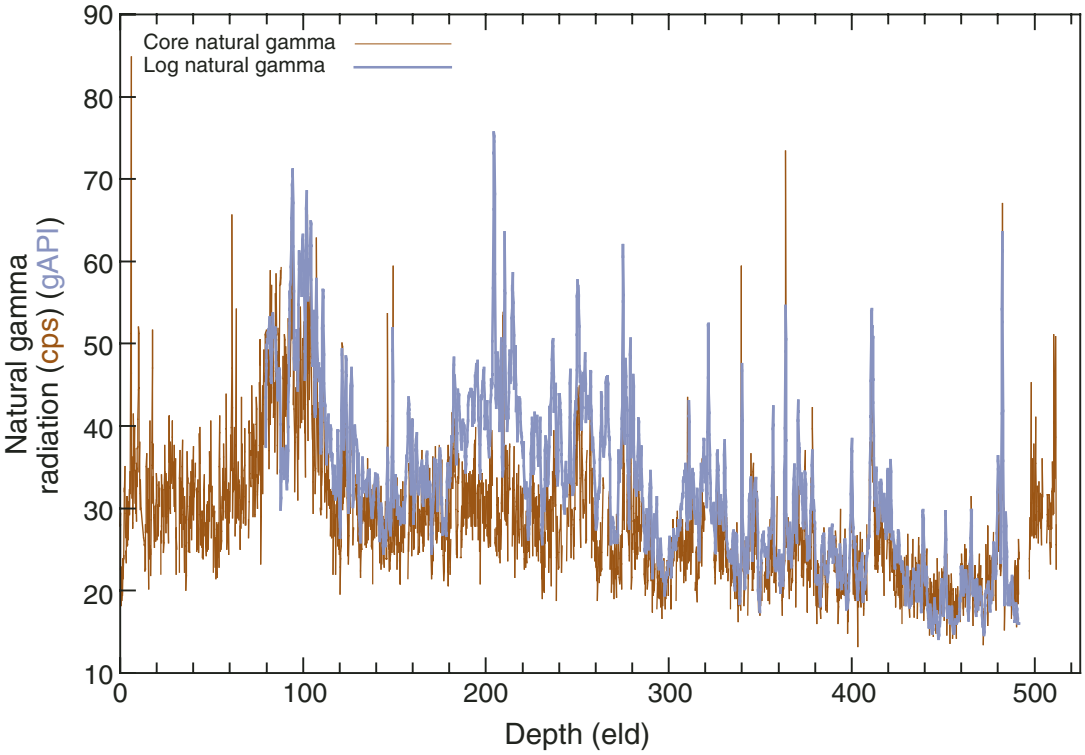

Figure F35. Dynamically normalized Formation MicroScanner (FMS) image of the borehole illustrating the meter-scale banding related to opal to carbonate oscillations.

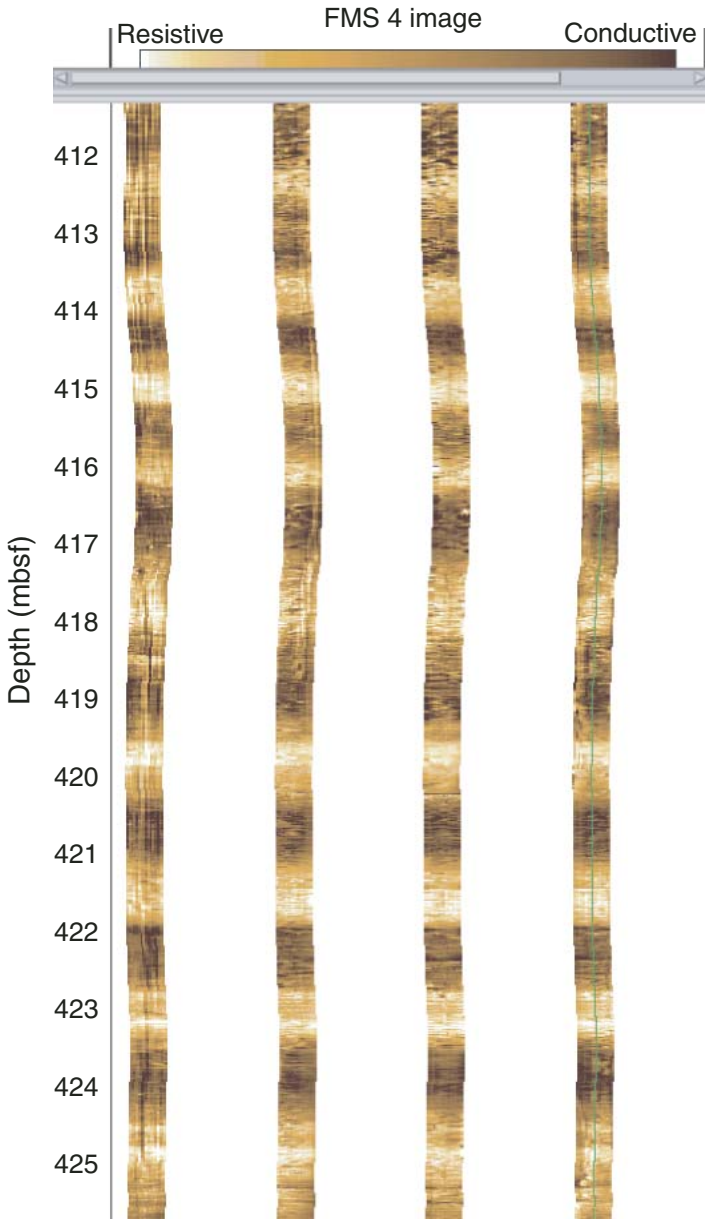

Figure F36. Total gamma ray and spectral gamma ray (HSGR) records for Hole 1239A. Total organic carbon (TOC) is plotted with the U log.

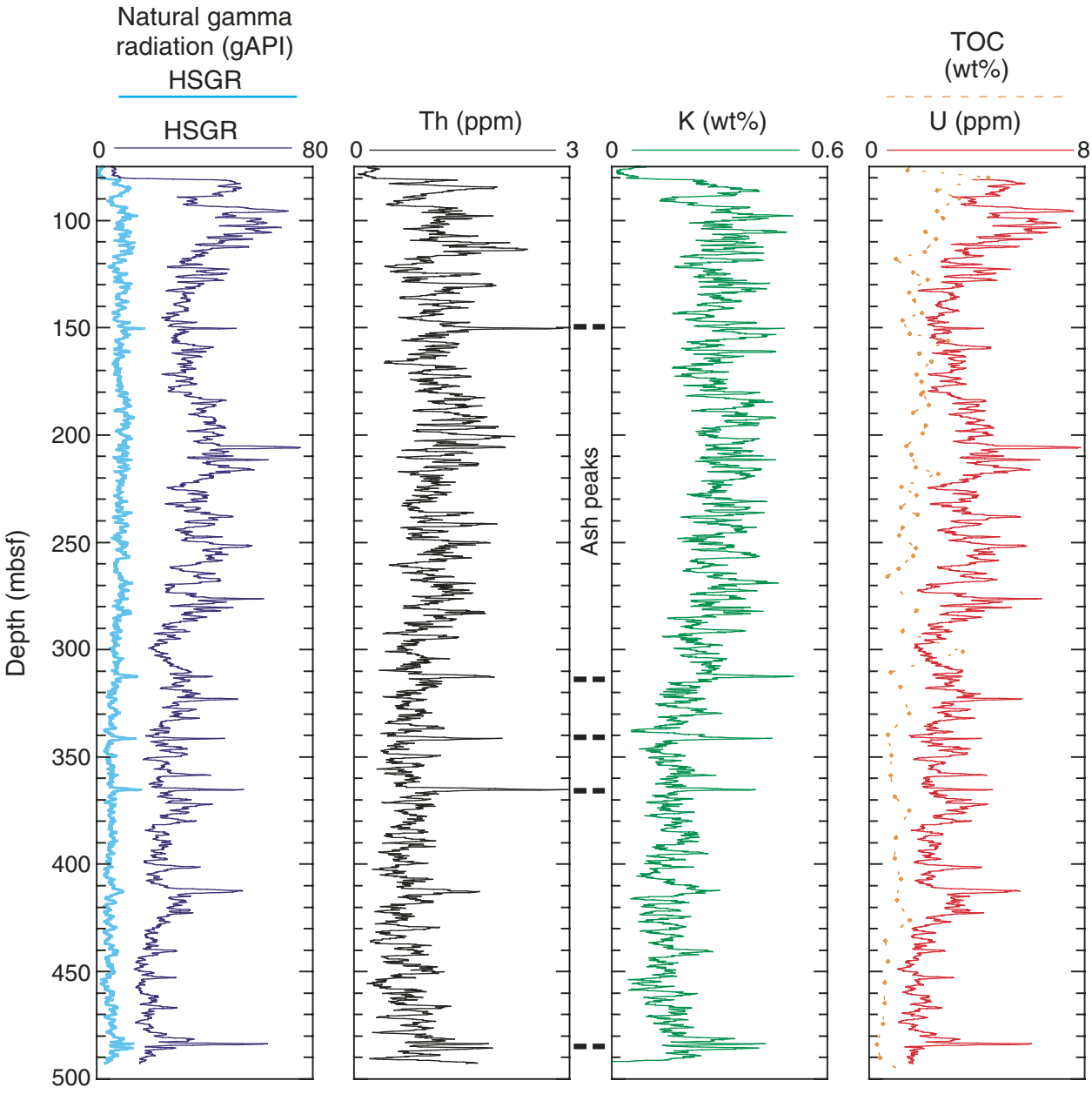

Figure F37. A. Shipboard biostratigraphic and magnetostratigraphic datums and age-depth model. **B.** Corrected linear sedimentation rates (LSR), total mass accumulation rates (MARs), and carbonate mass accumulation rates calculated from the smooth age model, average dry density, and calcium carbonate concentrations at 1-m.y. intervals. FO = first occurrence, LO = last occurrence.

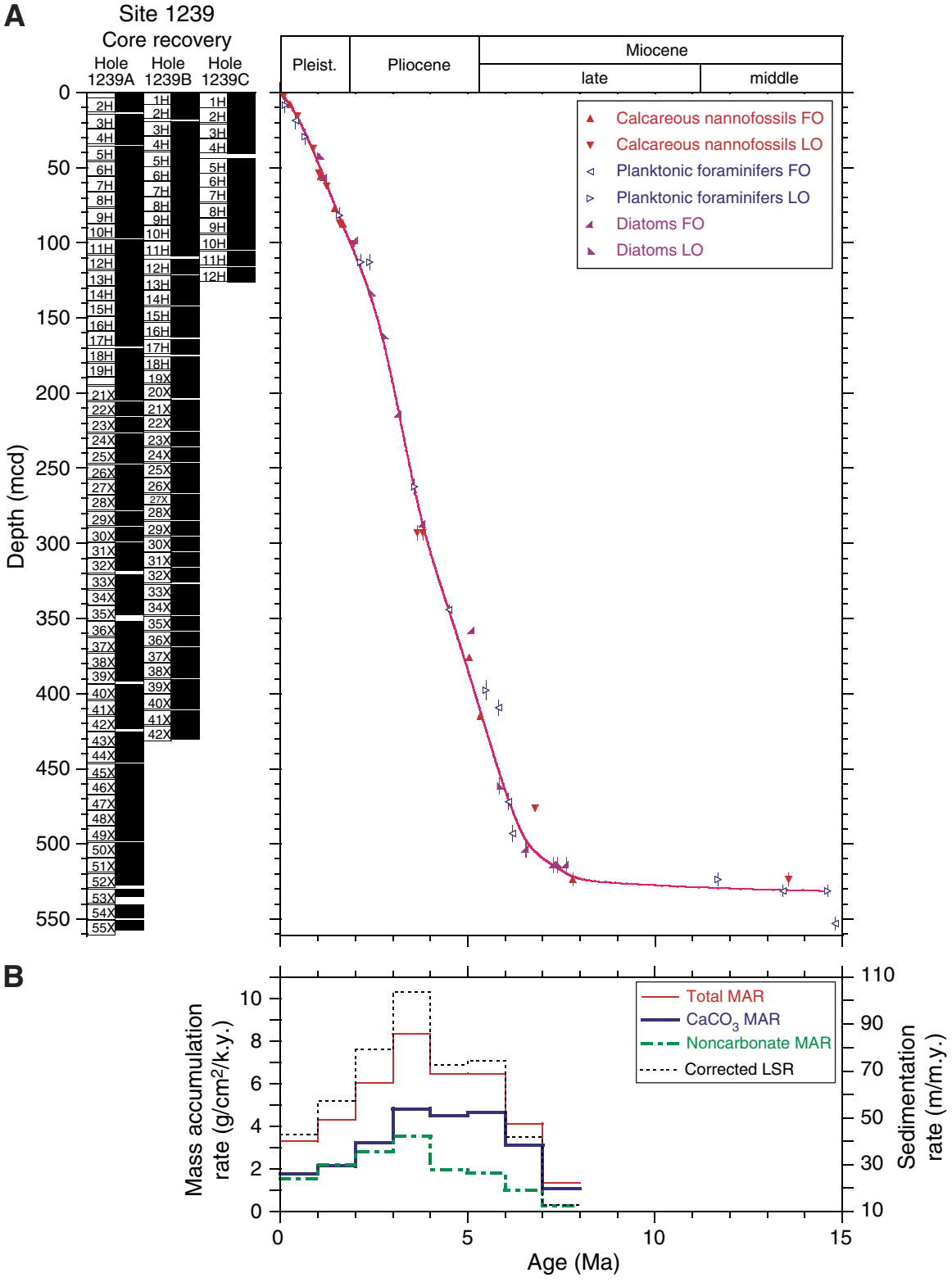

Table T1. Operations summary, Site 1239. (See table notes. Continued on next page.)

Core	Date (May 2002)	Local time	Depth (mbsf) Top	Depth (mbsf) Bottom	Length (m) Cored	Length (m) Recovered	Recovery (%)	APCT	Orientation	NMCB
202-1239A-										
1H	11	0125	0.0	3.4	3.4	3.46	101.8			
2H	11	0200	3.4	12.9	9.5	9.50	100.0			X
3H	11	0230	12.9	22.4	9.5	9.96	104.8			
4H	11	0300	22.4	31.9	9.5	10.00	105.3		Tensor	X
5H	11	0330	31.9	41.4	9.5	10.01	105.4		Tensor	
6H	11	0425	41.4	50.9	9.5	10.13	106.6	X	Tensor	X
7H	11	0455	50.9	60.4	9.5	10.03	105.6		Tensor	
8H	11	0552	60.4	69.9	9.5	10.03	105.6	X	Tensor	X
9H	11	0625	69.9	79.4	9.5	10.04	105.7		Tensor	
10H	11	0725	79.4	88.9	9.5	10.00	105.3	X	Tensor	X
11H	11	0815	88.9	98.4	9.5	9.91	104.3		Tensor	
12H	11	0910	98.4	107.9	9.5	10.05	105.8	X	Tensor	X
13H	11	0940	107.9	117.4	9.5	9.95	104.7		Tensor	
14H	11	1015	117.4	126.9	9.5	9.92	104.4		Tensor*	
15H	11	1050	126.9	136.4	9.5	10.08	106.1		Tensor*	
16H	11	1120	136.4	145.9	9.5	10.00	105.3		Tensor*	
17H	11	1205	145.9	155.4	9.5	10.02	105.5		Tensor*	
18H	11	1250	155.4	164.9	9.5	9.44	99.4		Tensor	
19H	11	1410	164.9	174.4	9.5	9.98	105.1		Tensor	
20X	11	1505	174.4	179.2	4.8	9.80	204.2			
21X	11	1535	179.2	188.9	9.7	9.77	100.7			
22X	11	1615	188.9	198.6	9.7	9.78	100.8			
23X	11	1650	198.6	208.3	9.7	9.79	100.9			
24X	11	1735	208.3	217.6	9.3	9.30	100.0			
25X	11	1759	217.6	227.2	9.6	9.77	101.8			
26X	11	1835	227.2	236.5	9.3	9.76	105.0			
27X	11	1905	236.5	246.1	9.6	9.77	101.8			
28X	11	1940	246.1	255.7	9.6	9.72	101.3			
29X	11	2010	255.7	265.3	9.6	9.51	99.1			
30X	11	2040	265.3	275.0	9.7	9.32	96.1			
31X	11	2115	275.0	284.6	9.6	9.92	103.3			
32X	11	2155	284.6	294.3	9.7	8.38	86.4			
33X	11	2230	294.3	303.9	9.6	9.94	103.5			
34X	11	2305	303.9	313.5	9.6	9.86	102.7			
35X	11	2340	313.5	323.2	9.7	6.05	62.4			
36X	12	0020	323.2	332.8	9.6	9.98	104.0			
37X	12	0055	332.8	342.4	9.6	9.75	101.6			
38X	12	0130	342.4	352.0	9.6	9.89	103.0			
39X	12	0210	352.0	361.7	9.7	8.14	83.9			
40X	12	0250	361.7	371.3	9.6	9.92	103.3			
41X	12	0330	371.3	381.0	9.7	9.87	101.8			
42X	12	0410	381.0	390.6	9.6	8.02	83.5			
43X	12	0445	390.6	400.2	9.6	9.93	103.4			
44X	12	0525	400.2	409.9	9.7	9.95	102.6			
45X	12	0605	409.9	419.4	9.5	9.88	104.0			
46X	12	0640	419.4	429.0	9.6	9.79	102.0			
47X	12	0715	429.0	438.7	9.7	9.84	101.4			
48X	12	0755	438.7	448.3	9.6	9.76	101.7			
49X	12	0830	448.3	458.0	9.7	9.79	100.9			
50X	12	0910	458.0	467.6	9.6	9.79	102.0			
51X	12	0950	467.6	477.2	9.6	9.83	102.4			
52X	12	1020	477.2	486.5	9.3	7.80	83.9			
53X	12	1100	486.5	496.1	9.6	5.11	53.2			
54X	12	1130	496.1	505.7	9.6	8.58	89.4			
55X	12	1250	505.7	515.4	9.7	6.53	67.3			
				Cored totals:	515.4	515.10	99.9			
202-1239B-										
1H	13	1105	0.0	7.8	7.8	7.86	100.8	X		X
2H	13	1135	7.8	17.3	9.5	9.87	103.9			
3H	13	1205	17.3	26.8	9.5	9.92	104.4		Tensor	X
4H	13	1240	26.8	36.3	9.5	10.04	105.7		Tensor	
5H	13	1310	36.3	45.8	9.5	9.95	104.7		Tensor	X
6H	13	1340	45.8	55.3	9.5	10.05	105.8		Tensor	
7H	13	1410	55.3	64.8	9.5	9.90	104.2		Tensor	X
8H	13	1445	64.8	74.3	9.5	10.03	105.6		Tensor	
9H	13	1515	74.3	83.8	9.5	9.88	104.0		Tensor	X

Table T1 (continued).

Core	Date (May 2002)	Local time	Depth (mbsf) Top	Depth (mbsf) Bottom	Length (m) Cored	Length (m) Recovered	Recovery (%)	APCT	Orientation	NMCB
10H	13	1555	83.8	93.3	9.5	10.02	105.5		Tensor	
11H	13	1635	93.3	102.8	9.5	9.91	104.3		Tensor	X
12H	13	1705	104.8	114.3	9.5	9.69	102.0		Tensor	
13H	13	1740	114.3	123.8	9.5	9.97	105.0		Tensor	X
14H	13	1815	123.8	133.3	9.5	9.96	104.8		Tensor	
15H	13	1850	133.3	142.8	9.5	10.07	106.0		Tensor	X
16H	13	2035	142.8	152.3	9.5	10.11	106.4		Tensor*	
17H	13	2130	152.3	161.8	9.5	10.02	105.5		Tensor	
18H	13	2235	161.8	171.3	9.5	10.01	105.4		Tensor	
19X	13	2330	171.3	180.6	9.3	9.86	106.0			
20X	14	5	180.6	190.3	9.7	9.02	93.0			
21X	14	35	190.3	200.0	9.7	9.54	98.4			
22X	14	105	200.0	209.6	9.6	9.70	101.0			
23X	14	135	209.6	218.9	9.3	9.39	101.0			
24X	14	205	218.9	228.5	9.6	9.62	100.2			
25X	14	235	228.5	237.9	9.4	9.45	100.5			
26X	14	310	237.9	247.5	9.6	9.84	102.5			
27X	14	345	247.5	254.1	6.6	8.99	136.2			
28X	14	415	254.1	263.7	9.6	9.60	100.0			
29X	14	445	263.7	273.4	9.7	9.40	96.9			
30X	14	525	273.4	283.0	9.6	9.44	98.3			
31X	14	550	283.0	292.7	9.7	9.24	95.3			
32X	14	625	292.7	302.4	9.7	9.33	96.2			
33X	14	655	302.4	312.0	9.6	9.85	102.6			
34X	14	725	312.0	321.6	9.6	9.78	101.9			
35X	14	800	321.6	331.3	9.7	9.70	100.0			
36X	14	835	331.3	340.9	9.6	9.85	102.6			
37X	14	905	340.9	350.5	9.6	9.92	103.3			
38X	14	935	350.5	360.1	9.6	9.85	102.6			
39X	14	1005	360.1	369.7	9.6	9.91	103.2			
40X	14	1040	369.7	379.4	9.7	9.85	101.6			
41X	14	1110	379.4	389.0	9.6	9.88	102.9			
42X	14	1145	389.0	398.7	9.7	9.05	93.3			
				Cored totals:	396.7	407.32	102.7			
202-1239C-										
1H	14	1430	1.3	10.8	9.5	9.86	103.8			
2H	14	1455	10.8	20.3	9.5	9.98	105.1			X
3H	14	1525	20.3	29.8	9.5	10.01	105.4		Tensor*	
4H	14	1600	29.8	39.3	9.5	10.12	106.5		Tensor*	X
5H	14	1630	41.3	50.8	9.5	9.68	101.9		Tensor	
6H	14	1700	50.8	60.3	9.5	9.93	104.5		Tensor	X
7H	14	1744	60.3	69.8	9.5	10.16	107.0		Tensor	
8H	14	1815	69.8	79.3	9.5	10.00	105.3		Tensor	X
9H	14	1850	79.3	88.8	9.5	10.02	105.5		Tensor	
10H	14	1950	88.8	98.3	9.5	10.02	105.5		Tensor	X
11H	14	2050	98.3	107.8	9.5	10.00	105.3		Tensor	
12H	14	2155	107.8	117.3	9.5	9.87	103.9		Tensor	X
				Cored totals:	114.0	119.65	105.0			
				Site totals:	1026.1	1042.07	101.6			

Notes: APCT = advanced piston corer temperature tool (stainless-steel housing is cutting shoe). NMCB = nonmagnetic core barrel, including cutting shoe (made from monel). X = APCT or NMCB was used. Tensor = brand name for core-barrel orientation tool. * = Tensor measurement attempted but problem occurred, resulting in bad or no data.

Table T2. Composite depth scale, Site 1239. (See table notes. Continued on next page.)

Core	Depth of core top		Depth offset		Translation to cmcd	
	Drillers (mbsf)	Composite (mcd)	Cumulative (m)	Differential (m)	Growth factor*	Depth (cmcd)†
202-1239A-						
1H	0.0	0.00	0.00	0.00	1.08	0.00
2H	3.4	3.55	0.15	0.15	1.08	3.29
3H	12.9	14.30	1.40	1.25	1.08	13.24
4H	22.4	24.60	2.20	0.80	1.08	22.78
5H	31.9	35.65	3.75	1.55	1.08	33.01
6H	41.4	46.00	4.60	0.85	1.08	42.59
7H	50.9	56.15	5.25	0.65	1.08	51.99
8H	60.4	66.35	5.95	0.70	1.08	61.44
9H	69.9	77.20	7.30	1.35	1.08	71.48
10H	79.4	87.20	7.80	0.50	1.08	80.74
11H	88.9	97.80	8.90	1.10	1.08	90.56
12H	98.4	108.20	9.80	0.90	1.08	100.19
13H	107.9	118.70	10.80	1.00	1.08	109.91
14H	117.4	128.75	11.35	0.55	1.08	119.21
15H	126.9	139.05	12.15	0.80	1.08	128.75
16H	136.4	149.20	12.80	0.65	1.08	138.15
17H	145.9	158.95	13.05	0.25	1.08	147.18
18H	155.4	170.40	15.00	1.95	1.08	157.78
19H	164.9	179.20	14.30	–0.70	1.08	165.93
20X	174.4	189.56	15.16	0.86	1.08	175.52
21X	179.2	195.22	16.02	0.86	1.08	180.76
22X	188.9	205.78	16.88	0.86	1.08	190.54
23X	198.6	216.34	17.74	0.86	1.08	200.31
24X	208.3	226.90	18.60	0.86	1.08	210.09
25X	217.6	237.06	19.46	0.86	1.08	219.50
26X	227.2	247.52	20.32	0.86	1.08	229.19
27X	236.5	257.68	21.18	0.86	1.08	238.59
28X	246.1	268.14	22.04	0.86	1.08	248.28
29X	255.7	278.60	22.90	0.86	1.08	257.96
30X	265.3	289.06	23.76	0.86	1.08	267.65
31X	275.0	299.62	24.62	0.86	1.08	277.43
32X	284.6	310.08	25.48	0.86	1.08	287.11
33X	294.3	320.64	26.34	0.86	1.08	296.89
34X	303.9	331.10	27.20	0.86	1.08	306.57
35X	313.5	341.56	28.06	0.86	1.08	316.26
36X	323.2	352.12	28.92	0.86	1.08	326.04
37X	332.8	362.58	29.78	0.86	1.08	335.72
38X	342.4	373.04	30.64	0.86	1.08	345.41
39X	352.0	383.50	31.50	0.86	1.08	355.09
40X	361.7	394.06	32.36	0.86	1.08	364.87
41X	371.3	404.52	33.22	0.86	1.08	374.56
42X	381.0	415.08	34.08	0.86	1.08	384.33
43X	390.6	425.54	34.94	0.86	1.08	394.02
44X	400.2	436.00	35.80	0.86	1.08	403.70
45X	409.9	446.56	36.66	0.86	1.08	413.48
46X	419.4	456.92	37.52	0.86	1.08	423.07
47X	429.0	467.38	38.38	0.86	1.08	432.76
48X	438.7	477.94	39.24	0.86	1.08	442.54
49X	448.3	488.40	40.10	0.86	1.08	452.22
50X	458.0	498.96	40.96	0.86	1.08	462.00
51X	467.6	509.42	41.82	0.86	1.08	471.69
52X	477.2	519.88	42.68	0.86	1.08	481.37
53X	486.5	530.04	43.54	0.86	1.08	490.78
54X	496.1	540.50	44.40	0.86	1.08	500.46
55X	505.7	550.96	45.26	0.86	1.08	510.15
202-1239B-						
1H	0.0	–0.05	–0.05	–0.05	1.08	–0.05
2H	7.8	7.80	0.00	0.05	1.08	7.22
3H	17.3	19.25	1.95	1.95	1.08	17.82
4H	26.8	29.10	2.30	0.35	1.08	26.94
5H	36.3	39.70	3.40	1.10	1.08	36.76
6H	45.8	49.40	3.60	0.20	1.08	45.74
7H	55.3	59.25	3.95	0.35	1.08	54.86
8H	64.8	69.55	4.75	0.80	1.08	64.40
9H	74.3	78.75	4.45	–0.30	1.08	72.92

Table T2 (continued).

Core	Depth of core top: Drillers (mbsf)	Depth of core top: Composite (mcd)	Depth offset: Cumulative (m)	Depth offset: Differential (m)	Translation to cmcd: Growth factor*	Translation to cmcd: Depth (cmcd)†
10H	83.8	88.75	4.95	0.50	1.08	82.18
11H	93.3	98.85	5.55	0.60	1.08	91.53
12H	104.8	111.05	6.25	0.70	1.08	102.82
13H	114.3	121.75	7.45	1.20	1.08	112.73
14H	123.8	131.85	8.05	0.60	1.08	122.08
15H	133.3	142.60	9.30	1.25	1.08	132.04
16H	142.8	152.75	9.95	0.65	1.08	141.44
17H	152.3	164.50	12.20	2.25	1.08	152.31
18H	161.8	175.60	13.80	1.60	1.08	162.59
19X	171.3	184.20	12.90	–0.90	1.08	170.56
20X	180.6	194.36	13.76	0.86	1.08	179.96
21X	190.3	204.92	14.62	0.86	1.08	189.74
22X	200.0	215.48	15.48	0.86	1.08	199.52
23X	209.6	225.94	16.34	0.86	1.08	209.20
24X	218.9	236.10	17.20	0.86	1.08	218.61
25X	228.5	246.56	18.06	0.86	1.08	228.30
26X	237.9	256.82	18.92	0.86	1.08	237.80
27X	247.5	267.28	19.78	0.86	1.08	247.48
28X	254.1	274.74	20.64	0.86	1.08	254.39
29X	263.7	285.20	21.50	0.86	1.08	264.07
30X	273.4	295.76	22.36	0.86	1.08	273.85
31X	283.0	306.22	23.22	0.86	1.08	283.54
32X	292.7	316.78	24.08	0.86	1.08	293.31
33X	302.4	327.34	24.94	0.86	1.08	303.09
34X	312.0	337.80	25.80	0.86	1.08	312.78
35X	321.6	348.26	26.66	0.86	1.08	322.46
36X	331.3	358.82	27.52	0.86	1.08	332.24
37X	340.9	369.28	28.38	0.86	1.08	341.93
38X	350.5	379.74	29.24	0.86	1.08	351.61
39X	360.1	390.20	30.10	0.86	1.08	361.30
40X	369.7	400.66	30.96	0.86	1.08	370.98
41X	379.4	411.22	31.82	0.86	1.08	380.76
42X	389.0	421.68	32.68	0.86	1.08	390.44
202-1239C-						
1H	1.3	0.35	–0.95	–0.95	1.08	0.32
2H	10.8	10.30	–0.50	0.45	1.08	9.54
3H	20.3	21.05	0.75	1.25	1.08	19.49
4H	29.8	30.90	1.10	0.35	1.08	28.61
5H	41.3	44.00	2.70	1.60	1.08	40.74
6H	50.8	53.80	3.00	0.30	1.08	49.81
7H	60.3	63.35	3.05	0.05	1.08	58.66
8H	69.8	73.95	4.15	1.10	1.08	68.47
9H	79.3	83.95	4.65	0.50	1.08	77.73
10H	88.8	94.65	5.85	1.20	1.08	87.64
11H	98.3	105.55	7.25	1.40	1.08	97.73
12H	107.8	116.45	8.65	1.40	1.08	107.82

Notes: * = calculated based on mbsf-mcd relationship for splice shown in Figure **F12,** p. 43. † = within the splice, the following equations apply: cmcd = mcd/growth factor, mcd = mbsf + cumulative depth offset, mcd = cmcd × growth factor, mbsf = cmcd × growth factor – cumulative offset. Growth factor in XCB cores is extrapolated from the APC section. This table is also available in **ASCII**.

Table T3. Splice tie points, Site 1239.

Hole, core, section, interval (cm)	Depth (mbsf)	Depth (mcd)	Depth (cmcd)		Hole, core, section, interval (cm)	Depth (mbsf)	Depth (mcd)	Depth (cmcd)
202-					202-			
1239A-1H-1, 120.0	1.20	1.20	1.11	Tie to	1239C-1H-1, 85.0	2.15	1.20	1.11
1239C-1H-6, 80.0	9.60	8.65	8.01	Tie to	1239B-2H-1, 85.0	8.65	8.65	8.01
1239B-2H-4, 145.0	13.75	13.75	12.73	Tie to	1239C-2H-3, 45.0	14.25	13.75	12.73
1239C-2H-6, 115.0	19.45	18.95	17.55	Tie to	1239A-3H-4, 15.0	17.55	18.95	17.55
1239A-3H-4, 130.0	18.70	20.10	18.61	Tie to	1239B-3H-1, 85.0	18.15	20.10	18.61
1239B-3H-4, 140.0	23.20	25.15	23.29	Tie to	1239C-3H-3, 110.0	24.40	25.15	23.29
1239C-3H-6, 120.0	29.00	29.75	27.55	Tie to	1239B-4H-1, 65.0	27.45	29.75	27.55
1239B-4H-4, 60.0	31.90	34.20	31.67	Tie to	1239C-4H-3, 30.0	33.10	34.20	31.67
1239C-4H-7, 30.0	39.10	40.20	37.22	Tie to	1239B-5H-1, 50.0	36.80	40.20	37.22
1239B-5H-4, 145.0	42.25	45.65	42.27	Tie to	1239C-5H-2, 15.0	42.95	45.65	42.27
1239C-5H-6, 30.0	49.10	51.80	47.96	Tie to	1239B-6H-2, 90.0	48.20	51.80	47.96
1239B-6H-6, 5.0	53.35	56.95	52.73	Tie to	1239C-6H-3, 15.0	53.95	56.95	52.73
1239C-6H-6, 45.0	58.75	61.75	57.18	Tie to	1239B-7H-2, 100.0	57.80	61.75	57.18
1239B-7H-6, 10.0	62.90	66.85	61.90	Tie to	1239C-7H-3, 50.0	63.80	66.85	61.90
1239C-7H-6, 130.0	69.10	72.15	66.81	Tie to	1239B-8H-2, 110.0	67.40	72.15	66.81
1239B-8H-5, 130.0	72.10	76.85	71.16	Tie to	1239C-8H-2, 140.0	72.70	76.85	71.16
1239C-8H-5, 90.0	76.70	80.85	74.86	Tie to	1239B-9H-2, 60.0	76.40	80.85	74.86
1239B-9H-5, 40.0	80.70	85.15	78.84	Tie to	1239C-9H-1, 120.0	80.50	85.15	78.84
1239C-9H-5, 90.0	86.20	90.85	84.12	Tie to	1239B-10H-2, 60.0	85.90	90.85	84.12
1239B-10H-6, 90.0	92.20	97.15	89.95	Tie to	1239C-10H-2, 100.0	91.30	97.15	89.95
1239C-10H-6, 50.0	96.80	102.65	95.05	Tie to	1239B-11H-3, 80.0	97.10	102.65	95.05
1239B-11H-5, 115.0	100.45	106.00	98.15	Tie to	1239C-11H-1, 45.0	98.75	106.00	98.15
1239C-11H-5, 70.0	105.00	112.25	103.94	Tie to	1239B-12H-1, 120.0	106.00	112.25	103.94
1239B-12H-6, 45.0	112.75	119.00	110.19	Tie to	1239C-12H-2, 105.0	110.35	119.00	110.19
1239C-12H-5, 70.0	114.50	123.15	114.03	Tie to	1239B-13H-1, 140.0	115.70	123.15	114.03
1239B-13H-6, 115.0	122.95	130.40	120.74	Tie to	1239A-14H-2, 15.0	119.05	130.40	120.74
1239A-14H-5, 60.0	124.00	135.35	125.32	Tie to	1239B-14H-3, 50.0	127.30	135.35	125.32
1239B-14H-6, 115.0	132.45	140.50	130.09	Tie to	1239A-15H-1, 145.0	128.35	140.50	130.09
1239A-15H-5, 10.0	133.00	145.15	134.40	Tie to	1239B-15H-2, 105.0	135.85	145.15	134.40
1239B-15H-6, 95.0	141.75	151.05	139.86	Tie to	1239A-16H-2, 35.0	138.25	151.05	139.86
1239A-16H-6, 10.0	144.00	156.80	145.19	Tie to	1239B-16H-3, 105.0	146.85	156.80	145.19
1239B-16H-6, 75.0	151.05	161.00	149.07	Tie to	1239A-17H-2, 52.5	147.95	161.00	149.07
1239A-17H-6, 20.0	153.60	166.65	154.31	Tie to	1239B-17H-2, 65.0	154.45	166.65	154.31
1239B-17H-6, 85.0	160.65	172.85	160.05	Tie to	1239A-18H-2, 95.0	157.85	172.85	160.05
1239A-18H-5, 95.0	162.35	177.35	164.21	Tie to	1239B-18H-2, 25.0	163.55	177.35	164.21
1239B-18H-6, 100.0	170.30	184.10	170.46	Tie to	1239A-19H-4, 40.0	169.80	184.10	170.46
1239A-19H-7, 65.0	174.55	188.85	174.86					

Note: This table is also available in **ASCII**.

Table T4. OSUS-MS measurements, Hole 1239A.

Core, section, interval (cm)	Depth (mbsf)	Depth (mcd)	Magnetic susceptibility (instrument units)	Run number	Depth from top of core (cm)
202-1239A-					
1H-1, 5	0.05	0.05	57.3	1514	5
1H-1, 10	0.10	0.10	62.8	1514	10
1H-1, 15	0.15	0.15	71.7	1514	15
1H-1, 20	0.20	0.20	75.1	1514	20
1H-1, 25	0.25	0.25	38.0	1514	25
1H-1, 30	0.30	0.30	29.8	1514	30
1H-1, 35	0.35	0.35	26.1	1514	35
1H-1, 40	0.40	0.40	20.1	1514	40
1H-1, 45	0.45	0.45	13.1	1514	45
1H-1, 50	0.50	0.50	9.7	1514	50
1H-1, 55	0.55	0.55	7.5	1514	55
1H-1, 60	0.60	0.60	5.8	1514	60
1H-1, 65	0.65	0.65	5.0	1514	65
1H-1, 70	0.70	0.70	4.1	1514	70
1H-1, 75	0.75	0.75	3.8	1514	75
1H-1, 80	0.80	0.80	3.2	1514	80
1H-1, 85	0.85	0.85	2.7	1514	85
1H-1, 90	0.90	0.90	2.9	1514	90
1H-1, 95	0.95	0.95	2.8	1514	95
1H-1, 100	1.00	1.00	2.9	1514	100
1H-1, 105	1.05	1.05	3.1	1514	105
1H-1, 110	1.10	1.10	2.5	1514	110
1H-1, 115	1.15	1.15	2.9	1514	115
1H-1, 120	1.20	1.20	3.2	1514	120
1H-1, 125	1.25	1.25	2.7	1514	125
1H-1, 130	1.30	1.30	3.5	1514	130
1H-1, 135	1.35	1.35	3.9	1514	135
1H-1, 140	1.40	1.40	3.6	1514	140
1H-2, 5	1.56	1.56	5.4	1515	155
1H-2, 10	1.61	1.61	6.0	1515	160
1H-2, 15	1.66	1.66	6.2	1515	165
1H-2, 20	1.71	1.71	6.2	1515	170
1H-2, 25	1.76	1.76	6.1	1515	175
1H-2, 30	1.81	1.81	6.2	1515	180
1H-2, 35	1.86	1.86	5.9	1515	185
1H-2, 40	1.91	1.91	5.9	1515	190
1H-2, 45	1.96	1.96	6.0	1515	195
1H-2, 50	2.01	2.01	5.5	1515	200
1H-2, 55	2.06	2.06	5.3	1515	205
1H-2, 60	2.11	2.11	5.3	1515	210
1H-2, 65	2.16	2.16	5.3	1515	215
1H-2, 70	2.21	2.21	5.2	1515	220
1H-2, 75	2.26	2.26	5.4	1515	225
1H-2, 80	2.31	2.31	7.6	1515	230
1H-2, 85	2.36	2.36	9.1	1515	235
1H-2, 90	2.41	2.41	8.8	1515	240
1H-3, 5	2.57	2.57	10.4	1516	255
1H-3, 10	2.62	2.62	12.2	1516	260
1H-3, 15	2.67	2.67	19.9	1516	265
1H-3, 20	2.72	2.72	24.0	1516	270
1H-3, 25	2.77	2.77	26.5	1516	275
1H-3, 30	2.82	2.82	27.5	1516	280
1H-3, 35	2.87	2.87	30.0	1516	285
1H-3, 40	2.92	2.92	23.8	1516	290
1H-3, 45	2.97	2.97	19.2	1516	295
1H-3, 50	3.02	3.02	14.0	1516	300
1H-3, 55	3.07	3.07	11.1	1516	305
1H-3, 60	3.12	3.12	9.8	1516	310
1H-3, 65	3.17	3.17	10.1	1516	315
1H-3, 70	3.22	3.22	10.1	1516	320
1H-3, 75	3.27	3.27	10.5	1516	325
1H-3, 80	3.32	3.32	8.8	1516	330
2H-1, 5	3.45	3.60	11.6	1517	5

Note: Only a portion of this table appears here. The complete table is available in **ASCII**.

Table T5. OSUS-MS measurements, Hole 1239B.

Core, section, interval (cm)	Depth (mbsf)	Depth (mcd)	Magnetic susceptibility (instrument units)	Run number	Depth from top of core (cm)
202-1239B-					
1H-1, 5	0.05	0.00	341.4	1756	5
1H-1, 10	0.10	0.05	87.1	1756	10
1H-1, 15	0.15	0.10	73.7	1756	15
1H-1, 20	0.20	0.15	73.0	1756	20
1H-1, 25	0.25	0.20	55.2	1756	25
1H-1, 30	0.30	0.25	32.4	1756	30
1H-1, 35	0.35	0.30	24.3	1756	35
1H-1, 40	0.40	0.35	22.3	1756	40
1H-1, 45	0.45	0.40	15.4	1756	45
1H-1, 50	0.50	0.45	8.8	1756	50
1H-1, 55	0.55	0.50	6.7	1756	55
1H-1, 60	0.60	0.55	4.4	1756	60
1H-1, 65	0.65	0.60	3.4	1756	65
1H-1, 70	0.70	0.65	3.0	1756	70
1H-1, 75	0.75	0.70	2.5	1756	75
1H-1, 80	0.80	0.75	2.1	1756	80
1H-1, 85	0.85	0.80	1.8	1756	85
1H-1, 90	0.90	0.85	1.7	1756	90
1H-1, 95	0.95	0.90	1.7	1756	95
1H-1, 100	1.00	0.95	1.3	1756	100
1H-1, 105	1.05	1.00	1.4	1756	105
1H-1, 110	1.10	1.05	1.5	1756	110
1H-1, 115	1.15	1.10	1.5	1756	115
1H-1, 120	1.20	1.15	1.3	1756	120
1H-1, 125	1.25	1.20	1.6	1756	125
1H-1, 130	1.30	1.25	1.8	1756	130
1H-1, 135	1.35	1.30	1.9	1756	135
1H-1, 140	1.40	1.35	1.9	1756	140
1H-1, 145	1.45	1.40	2.3	1756	145
1H-2, 5	1.57	1.52	3.5	1757	155
1H-2, 10	1.62	1.57	4.2	1757	160
1H-2, 15	1.67	1.62	4.7	1757	165
1H-2, 20	1.72	1.67	5.1	1757	170
1H-2, 25	1.77	1.72	5.2	1757	175
1H-2, 30	1.82	1.77	5.3	1757	180
1H-2, 35	1.87	1.82	4.8	1757	185
1H-2, 40	1.92	1.87	4.6	1757	190
1H-2, 45	1.97	1.92	4.7	1757	195
1H-2, 50	2.02	1.97	4.8	1757	200
1H-2, 55	2.07	2.02	4.8	1757	205
1H-2, 60	2.12	2.07	5.0	1757	210
1H-2, 65	2.17	2.12	5.3	1757	215
1H-2, 70	2.22	2.17	6.0	1757	220
1H-2, 75	2.27	2.22	6.0	1757	225
1H-2, 80	2.32	2.27	6.4	1757	230
1H-2, 85	2.37	2.32	6.6	1757	235
1H-2, 90	2.42	2.37	7.2	1757	240
1H-2, 95	2.47	2.42	7.1	1757	245
1H-2, 100	2.52	2.47	7.6	1757	250
1H-2, 105	2.57	2.52	8.3	1757	255
1H-2, 110	2.62	2.57	9.3	1757	260
1H-2, 115	2.67	2.62	10.8	1757	265
1H-2, 120	2.72	2.67	14.8	1757	270
1H-2, 125	2.77	2.72	20.6	1757	275
1H-2, 130	2.82	2.77	24.6	1757	280
1H-2, 135	2.87	2.82	27.8	1757	285
1H-2, 140	2.92	2.87	35.5	1757	290
1H-2, 145	2.97	2.92	35.4	1757	295
1H-3, 5	3.08	3.03	26.1	1758	305
1H-3, 10	3.13	3.08	18.8	1758	310
1H-3, 15	3.18	3.13	16.9	1758	315
1H-3, 20	3.23	3.18	14.2	1758	320
1H-3, 25	3.28	3.23	11.9	1758	325

Note: Only a portion of this table appears here. The complete table is available in **ASCII**.

Table T6. OSUS-MS measurements, Hole 1239C.

Core, section, interval (cm)	Depth (mbsf)	Depth (mcd)	Magnetic susceptibility (instrument units)	Run number	Depth from top of core (cm)
202-1239C-					
1H-1, 5	1.35	0.40	52.4	1766	5
1H-1, 10	1.40	0.45	16.9	1766	10
1H-1, 15	1.45	0.50	6.3	1766	15
1H-1, 20	1.50	0.55	4.7	1766	20
1H-1, 25	1.55	0.60	4.6	1766	25
1H-1, 30	1.60	0.65	4.0	1766	30
1H-1, 35	1.65	0.70	3.6	1766	35
1H-1, 40	1.70	0.75	3.5	1766	40
1H-1, 45	1.75	0.80	3.2	1766	45
1H-1, 50	1.80	0.85	3.1	1766	50
1H-1, 55	1.85	0.90	3.3	1766	55
1H-1, 60	1.90	0.95	3.2	1766	60
1H-1, 65	1.95	1.00	3.5	1766	65
1H-1, 70	2.00	1.05	3.6	1766	70
1H-1, 75	2.05	1.10	3.7	1766	75
1H-1, 80	2.10	1.15	4.0	1766	80
1H-1, 85	2.15	1.20	4.4	1766	85
1H-1, 90	2.20	1.25	4.4	1766	90
1H-1, 95	2.25	1.30	4.8	1766	95
1H-1, 100	2.30	1.35	5.1	1766	100
1H-1, 105	2.35	1.40	5.3	1766	105
1H-1, 110	2.40	1.45	5.6	1766	110
1H-1, 115	2.45	1.50	5.7	1766	115
1H-1, 120	2.50	1.55	6.2	1766	120
1H-1, 125	2.55	1.60	7.8	1766	125
1H-1, 130	2.60	1.65	5.2	1766	130
1H-1, 135	2.65	1.70	5.0	1766	135
1H-1, 140	2.70	1.75	5.1	1766	140
1H-1, 145	2.75	1.80	4.5	1766	145
1H-2, 5	2.86	1.91	5.8	1767	155
1H-2, 10	2.91	1.96	6.5	1767	160
1H-2, 15	2.96	2.01	6.8	1767	165
1H-2, 20	3.01	2.06	7.0	1767	170
1H-2, 25	3.06	2.11	7.2	1767	175
1H-2, 30	3.11	2.16	7.5	1767	180
1H-2, 35	3.16	2.21	8.9	1767	185
1H-2, 40	3.21	2.26	9.6	1767	190
1H-2, 45	3.26	2.31	9.9	1767	195
1H-2, 50	3.31	2.36	9.8	1767	200
1H-2, 55	3.36	2.41	9.5	1767	205
1H-2, 60	3.41	2.46	9.9	1767	210
1H-2, 65	3.46	2.51	13.4	1767	215
1H-2, 70	3.51	2.56	19.8	1767	220
1H-2, 75	3.56	2.61	22.9	1767	225
1H-2, 80	3.61	2.66	23.5	1767	230
1H-2, 85	3.66	2.71	27.5	1767	235
1H-2, 90	3.71	2.76	31.2	1767	240
1H-2, 95	3.76	2.81	29.8	1767	245
1H-2, 100	3.81	2.86	24.4	1767	250
1H-2, 105	3.86	2.91	17.2	1767	255
1H-2, 110	3.91	2.96	11.8	1767	260
1H-2, 115	3.96	3.01	9.6	1767	265
1H-2, 120	4.01	3.06	8.8	1767	270
1H-2, 125	4.06	3.11	9.1	1767	275
1H-2, 130	4.11	3.16	8.4	1767	280
1H-2, 135	4.16	3.21	8.0	1767	285
1H-2, 140	4.21	3.26	9.5	1767	290
1H-2, 145	4.26	3.31	9.6	1767	295
1H-3, 5	4.37	3.42	9.3	1788	305
1H-3, 10	4.42	3.47	8.8	1788	310
1H-3, 15	4.47	3.52	8.1	1788	315
1H-3, 20	4.52	3.57	7.3	1788	320
1H-3, 25	4.57	3.62	6.6	1788	325

Note: Only a portion of this table appears here. The complete table is available in **ASCII**.

Table T7. Lithologic Unit I, Site 1239.

Unit	Top			Base			Description	Interpretation
	Hole, core, section, interval (cm)	Depth (mbsf)	Depth (mcd)	Hole, core, section, interval (cm)	Depth (mbsf)	Depth (mcd)		
	202-							
I	1239A-1H-1, 0	0.0	0.0	1239A-55X-CC, 55	512.3	557.5	Nannofossil ooze and foraminifer ooze with clay, diatoms, and micrite	Pelagic setting with moderate to high productivity
	1239B-1H-1, 0	0.0	0.0	1239B-42X-CC, 37	398.1	430.7		
	1239C-1H-1, 0	0.0	0.0	1239C-12H-CC, 24	117.7	126.4		

Table T8. Ash layers, Site 1239.

Number	Core, section, interval (cm)	Top depth (mcd)	Bottom depth (mcd)	Bottom depth (mbsf)	Core, section, interval (cm)	Top depth (mcd)	Bottom depth (mcd)	Bottom depth (mbsf)	Core, section, interval (cm)	Top depth (mcd)	Bottom depth (mcd)	Bottom depth (mbsf)
	202-1239A-				202-1239B-				202-1239C-			
1	**2H-2, 11–14**	**5.16**	**5.19**	**5.04**	**1H-4, 87–92**	**5.36**	**5.41**	**5.46**	NF			
2	NF				NF				1H-4, 69–71	5.57	5.59	6.54
3	NF				NF				1H-4, 89–93	5.77	5.81	6.76
4	**2H-3, 10–28**	**6.65**	**6.83**	**6.68**	**1H-5, 85–107**	**6.87**	**7.07**	**7.12**	**1H-5, 33–49**	**6.72**	**6.88**	**7.83**
5	2H-3, 41–46	6.96	7.01	6.86	NF				NF			
6	2H-6, 37–38	11.42	11.43	11.28	NF				NF			
7	Core gap				2H-4, 90–98	13.23	13.31	13.31	2H-2, 140–145	13.21	13.26	13.76
8	**3H-4, 72–78**	**19.54**	**19.60**	**18.20**	Core gap				2H-7, 39–45	19.72	19.78	20.28
9	**6H-5, 79–80**	**52.81**	**52.82**	**48.22**	**6H-3, 31–43**	**52.73**	**52.85**	**49.35**	NF			
10	**7H-3, 124–136**	**60.39**	**60.51**	**55.26**	**7H-1, 101–105**	**60.26**	**60.30**	**56.35**	**6H-5, 47–48**	**60.32**	**60.33**	**57.33**
11	**7H-6, 40–42**	**64.06**	**64.08**	**58.83**	**7H-3, 121–124**	**63.48**	**63.51**	**59.56**	Core gap			
12	8H-1, 106–118	67.41	67.53	61.58	7H-6, 63–77	67.43	67.57	63.62	7H-3, 110–119	67.45	67.54	64.49
13	NF				NF				8H-5, 36–38	80.35	80.37	76.22
14	**9H-5, 121–127**	**84.46**	**84.52**	**77.22**	**9H-4, 109–110**	**84.38**	**84.39**	**79.94**	**9H-1, 30–35**	**84.25**	**84.30**	**79.65**
15	**10H-3, 93–96**	**91.14**	**91.17**	**83.37**	**10H-2, 79–81**	**91.05**	**91.07**	**86.12**	**9H-5, 108–109**	**91.06**	**91.07**	**86.42**
16	**13H-1, 0–4**	**118.70**	**118.74**	**107.94**	**12H-6, 14–19**	**118.76**	**118.81**	**112.56**	**12H-2, 74–78**	**118.69**	**118.73**	**110.08**
17	**17H-2, 84–90**	**161.30**	**161.36**	**148.31**	**16H-6, 100–103**	**161.30**	**161.33**	**151.38**				
18	**18H-2, 122–125**	**173.13**	**173.16**	**158.16**	**17H-6, 115–118**	**173.21**	**173.24**	**161.04**				
19	30X-1, 84–91	289.90	289.97	266.21								
20	34X-5, 29–31	337.41	337.43	310.23								
21	37X-5, 67–74	369.28	369.35	339.57								
22	40X-2, 90–92	396.47	396.49	364.13								
23	52X-5, 107–109	526.99	527.01	484.33								
24	52X-5, 123–126	527.15	527.18	484.50								

Notes: Ash layers that could be correlated between holes are located in the same row and printed in bold type. NF = not found.

Table T9. Age-depth control points, Hole 1239A. (See table notes. Continued on next page.)

Datum	Source	Age (Ma) Minimum	Age (Ma) Maximum	Top sample (FO presence/LO absence) Core, section, interval (cm)	Top sample (FO presence/LO absence) Depth (mbsf)	Bottom sample (LO presence/FO absence) Core, section, interval (cm)	Bottom sample (LO presence/FO absence) Depth (mbsf)	Age (Ma) Average	Age (Ma) Uncertainty (±)	Depth Average (mbsf)	Depth Average (mcd)	Depth Uncertainty (±m)
				202-1239A-		202-1239A-						
Start of *Emiliania huxleyi* acme	CN	0.08	0.08	1H-2, 75	2.26	1H-3, 40	2.92	0.08	0.00	2.59	2.59	0.33
LO *Globigerinoides ruber* pink	PF	0.12	0.12	1H-CC, 9	3.44	2H-CC, 20	12.85	0.12	0.00	8.15	8.22	4.71
FO *Emiliania huxleyi*	CN	0.26	0.26	2H-3, 75	7.15	2H-4, 75	8.65	0.26	0.00	7.90	8.05	0.75
FO *Globigerinoides ruber* pink	PF	0.40	0.40	2H-CC, 20	12.85	3H-CC, 18	22.88	0.40	0.00	17.87	18.64	5.02
LO *Pseudoemiliania lacunosa*	CN	0.46	0.46	3H-1, 75	13.65	3H-2, 75	15.16	0.46	0.00	14.41	15.81	0.76
LO *Globorotalia tosaensis*	PF	0.65	0.65	3H-CC, 18	22.88	4H-CC, 26	32.39	0.65	0.00	27.64	29.44	4.76
LO *Stilostomella*	PF	0.65	0.65	3H-CC, 18	22.88	4H-CC, 26	32.39	0.65	0.00	27.64	29.44	4.76
LO *Reticulofenestra asanoi*	CN	0.88	0.88	5H-1, 75	32.65	5H-2, 75	34.15	0.88	0.00	33.40	37.15	0.75
Reentry *Gephyrocapsa* (medium)	CN	1.02	1.02	6H-5, 75	48.17	6H-6, 75	49.67	1.02	0.00	48.92	53.52	0.75
LO *Rhizosolenia matuyamai*	D	1.05	1.05	5H-4, 75	37.16	5H-6, 75	40.18	1.05	0.00	38.67	42.42	1.51
FO *Reticulofenestra asanoi*	CN	1.08	1.08	6H-7, 40	50.82	6H-CC, 35	51.50	1.08	0.00	51.16	55.76	0.34
FO *Rhizosolenia matuyamai*	D	1.18	1.18	6H-CC, 35	51.50	7H-1, 75	51.65	1.18	0.00	51.58	56.50	0.08
LO *Gephyrocapsa* (large)	CN	1.24	1.24	7H-4, 75	56.15	7H-5, 75	57.65	1.24	0.00	56.90	62.15	0.75
FO *Gephyrocapsa* (large)	CN	1.45	1.45	8H-CC, 31	70.46	9H-1, 75	70.65	1.45	0.00	70.56	77.18	0.10
LO *Neogloboquadrina acostaensis*	PF	1.58	1.58	8H-CC, 31	70.46	9H-CC, 21	79.96	1.58	0.00	75.21	81.84	4.75
LO *Calcidiscus macintyrei*	CN	1.59	1.59	9H-7, 40	79.36	9H-CC, 21	79.96	1.59	0.00	79.66	86.96	0.30
FO *Gephyrocapsa* (medium)	CN	1.67	1.67	9H-CC, 21	79.96	10H-1, 75	80.15	1.67	0.00	80.06	87.61	0.10
LO *Discoaster brouweri*	CN	1.96	1.96	11H-2, 75	91.16	11H-3, 75	92.67	1.96	0.00	91.92	100.82	0.75
FO *Pseudoeunotia doliolus*	D	2.00	2.00	10H-CC, 30	89.43	11H-2, 75	91.16	2.00	0.00	90.30	98.65	0.86
LO *Globorotalia exilis*	PF	2.15	2.15	11H-CC, 21	98.83	12H-CC, 23	117.88	2.15	0.00	108.36	112.95	9.52
LO *Globorotalia limbata*	PF	2.38	2.38	11H-CC, 21	98.83	12H-CC, 23	117.88	2.38	0.00	108.36	112.95	9.52
LO *Thalassiosira convexa* s.l.	D	2.41	2.41	14H-3, 75	121.18	14H-4, 75	122.70	2.41	0.00	121.94	133.29	0.76
LO *Nitzschia jouseae*	D	2.77	2.77	17H-2, 75	148.16	17H-3, 75	149.67	2.77	0.00	148.92	161.97	0.75
FO *Rhizosolenia praebergonii* s.l.	D	3.17	3.17	22X-5, 75	195.69	22X-7, 40	198.36	3.17	0.00	197.03	213.91	1.34
LO *Globorotalia margaritae*	PF	3.58	3.58	26X-CC, 30	236.96	27X-CC, 33	246.24	3.58	0.00	241.60	262.35	4.64
LO *Sphenolithus* spp.	CN	3.65	3.65	29X-CC, 30	265.19	30X-CC, 1	274.23	3.65	0.00	269.71	293.04	4.52
LO *Reticulofenestra pseudoumbilicus*	CN	3.80	3.80	29X-CC, 30	265.19	30X-CC, 1	274.23	3.80	0.00	269.71	293.04	4.52
FO *Thalassiosira convexa* v. *convexa*	D	3.81	3.81	29X-6, 40	263.63	29X-7, 40	264.63	3.81	0.00	264.13	287.03	0.50
FO *Globorotalia puncticulata*	PF	4.50	4.50	34X-CC, 34	313.78	35X-CC, 35	319.53	4.50	0.00	316.66	344.27	2.88
FO *Ceratolithus cristatus*	CN	5.04	5.04	38X-2, 75	344.70	38X-3, 75	346.20	5.04	0.00	345.45	376.06	0.75
FO *Nitzschia jouseae*	D	5.12	5.12	36X-4, 75	328.47	36X-5, 75	329.98	5.12	0.00	329.23	358.15	0.75
FO *Ceratolithus acutus*	CN	5.34	5.34	41X-CC, 34	381.19	42X-1, 75	381.80	5.34	0.00	381.50	415.12	0.31
LO *Globoquadrina dehiscens*	PF	5.49	5.49	39X-CC, 1	359.76	40X-CC, 34	371.64	5.49	0.00	365.70	397.63	5.94
FO *Globorotalia tumida*	PF	5.82	5.82	40X-CC, 34	371.64	41X-CC, 34	381.19	5.82	0.00	376.42	409.21	4.77
LO *Thalassiosira miocenica*	D	5.84	5.84	45X-CC, 37	419.82	46X-CC, 31	429.18	5.84	0.00	424.50	461.59	4.68
FO *Globorotalia margaritae*	PF	6.09	6.09	46X-CC, 31	429.18	47X-CC, 33	438.85	6.09	0.00	434.02	471.97	4.83
FO *Globigerinoides conglobatus*	PF	6.20	6.20	48X-CC, 33	448.48	49X-CC, 28	458.10	6.20	0.00	453.29	492.96	4.81
FO *Thalassiosira miocenica*	D	6.55	6.55	49X-CC, 28	458.10	50X-CC, 31	467.80	6.55	0.00	462.95	503.48	4.85
FO *Thalassiosira convexa* v. *aspinosa*	D	6.57	6.57	49X-CC, 28	458.10	50X-CC, 31	467.80	6.57	0.00	462.95	503.48	4.85
LO Absence interval *Reticulofenestra pseudoumbilicus* >7 µm	CN	6.80	6.80	47X-6, 75	437.29	47X-7, 40	438.25	6.80	0.00	437.77	476.15	0.48
FO *Nitzschia miocenica* s.l.	D	7.30	7.30	50X-CC, 31	467.80	51X-CC, 35	477.47	7.30	0.00	472.64	514.03	4.83
LO *Rossiela paleasea* group	D	7.40	7.40	50X-CC, 31	467.80	51X-CC, 35	477.47	7.40	0.00	472.64	514.03	4.83
FO *Nitzschia reinholdii*	D	7.64	7.64	50X-CC, 31	467.80	51X-CC, 35	477.47	7.64	0.00	472.64	514.03	4.83
FO *Discoaster surculus*	CN	7.80	7.80	51X-CC, 35	477.47	52X-CC, 32	485.01	7.80	0.00	481.24	523.49	3.77
LO *Globorotalia fohsi* s.l.	PF	11.68	11.68	51X-CC, 35	477.47	52X-CC, 32	485.01	11.68	0.00	481.24	523.49	3.77
FO *Globorotalia fohsi* s.l.	PF	13.42	13.42	52X-CC, 32	485.01	53X-CC, 8	491.35	13.42	0.00	488.18	531.29	3.17

Table T9 (continued).

Datum	Source	Age (Ma) Minimum	Age (Ma) Maximum	Top sample (FO presence/LO absence) Core, section, interval (cm)	Top sample (FO presence/LO absence) Depth (mbsf)	Bottom sample (LO presence/FO absence) Core, section, interval (cm)	Bottom sample (LO presence/FO absence) Depth (mbsf)	Age (Ma) Average	Age (Ma) Uncertainty (±)	Depth Average (mbsf)	Depth Average (mcd)	Depth Uncertainty (±m)
LO *Sphenolithus heteromorphus*	CN	13.57	13.57	51X-CC, 35	477.47	52X-CC, 32	485.01	13.57	0.00	481.24	523.49	3.77
LO *Globorotalia peripheroronda*	PF	14.6	14.6	52X-CC, 32	485.01	53X-CC, 8	491.35	14.60	0.00	488.18	531.29	3.17
FO *Globorotalia peripheroacuta*	PF	14.8	14.8	54X-CC, 27	504.71	55X-CC, 1	511.72	14.80	0.00	508.22	553.05	3.51
FO *Globorotalia praemenardii*	PF	14.9	14.9	55X-CC, 1	511.72							

Notes: FO = first occurrence, LO = last occurrence. CN = calcareous nannofossils, PF = planktonic foraminifers, D = diatoms.

Table T10. Distribution of calcareous nannofossils, Hole 1239A. (**See table notes.** Continued on next two pages.)

Core, section, interval (cm)	Depth (mbsf)	Depth (mcd)	Preservation	Abundance	*Amaurolithus primus/delicatus*	*Calcidiscus macintyrei*	*Calcidiscus premacintyrei*	*Ceratolithus armatus*	*Ceratolithus cristatus*	*Coccolithus miopelagicus*	*Cyclicargolithus floridanus*	*Discoaster brouweri*	*Discoaster loeblichii*	*Discoaster pentaradiatus*	*Discoaster quinqueramus/berggrenii*	*Discoaster surculus*	*Discoaster tamalis*	*Discoaster variabilis* gr.	*Emiliania huxleyi*	*Gephyrocapsa* spp. (large)	*Gephyrocapsa* spp. (medium)	*Gephyrocapsa* spp. (small)	*Helicosphaera sellii*	*Pseudoemiliania lacunosa*	*Reticulofenestra asanoi*	*Reticulofenestra pseudoumbilicus* >7 µm	*Reticulofenestra rotaria*	*Reticulofenestra* <7 µm	*Sphenolithus abies/neoabies*	*Sphenolithus heteromorphus*
202-1239A-																														
1H-1, 0	0.00	0.00	G	A															C			C								
1H-1, 75	0.75	0.75	G	A															C		F	F								
1H-2, 75	2.26	2.26	G	A															A		F	F								
1H-3, 40	2.92	2.92	G	A															F		C	A								
1H-CC, 9	3.44	3.44	G	A															F		A	A								
2H-3, 75	7.15	7.30	G	A															F		C	A								
2H-4, 75	8.65	8.80	G	A																	A	A								
2H-5, 75	10.15	10.30	G	A																	A	A								
2H-CC, 20	12.85	13.00	G	VA																	A	A								
3H-1, 75	13.65	15.05	G	A																	C	A								
3H-2, 75	15.16	16.56	G	A																	C	A		R						
3H-3, 75	16.66	18.06	G	A																	C	A		R						
3H-5, 75	19.68	21.08	G	A																	C	A		R						
3H-7, 40	22.35	23.75	G	A																	C	A		F						
3H-CC, 18	22.88	24.28	G	A																	C	C		R						
4H-CC, 26	32.39	34.59	G	A																	A	A		F						
5H-1, 75	32.65	36.40	G	A																	A	A		F						
5H-2, 75	34.15	37.90	G	A																	A	A		F	R					
5H-3, 75	35.66	39.41	G	A																	A	A		F	F					
5H-CC, 22	41.91	45.66	M	A																	A	A		F	F					
6H-3, 75	45.16	49.76	G	A																	C	A		C	F					
6H-5, 75	48.17	52.77	G	A																	C	A		C	F					
6H-6, 75	49.67	54.27	G	A																		A		C	F					
6H-7, 40	50.82	55.42	G	A																		A		C	F					
6H-CC, 35	51.50	56.10	G	A																		A		C						
7H-3, 75	54.65	59.90	M	A																		A		C						
7H-4, 75	56.15	61.40	M	A																		A		C						
7H-5, 75	57.65	62.90	M	A																C	C	A		C						
7H-CC, 24	60.91	66.16	M	A																F	C	A		C						
8H-CC, 31	70.46	76.41	G	A																R	C	A		F						
9H-1, 75	70.65	77.95	G	A																	C	A		C						
9H-3, 75	73.68	80.98	G	A																	C	A		C						
9H-CC, 21	79.96	87.26	G	A		R															C	A		C						
10H-1, 75	80.15	87.95	G	A		R																C		C						
10H-2, 75	81.66	89.46	G	A		R																C		C						
10H-3, 75	83.16	90.96	G	A		F																C		C						
10H-4, 75	84.68	92.48	G	A		F																C		C						
10H-6, 75	87.71	95.51	G	A		F																C		C						
10H-CC, 30	89.43	97.23	G	A		F																C		C				C		
11H-1, 75	89.65	98.55	M	C		F																A		C						
11H-2, 75	91.16	100.06	M	C		F																A		C						
11H-3, 75	92.67	101.57	M	C		F						R			R			R				A		C						
11H-4, 75	94.18	103.08	M	C		F						R				R						A		C						
11H-5, 75	95.69	104.59	M	C		F										R		R				A		C						
11H-CC, 21	98.83	107.73	G	A		F						R										A		C				C		
12H-CC, 35	108.48	118.28	G	A		R						R										A		C				C		
13H-CC, 23	117.88	128.68	M	A								R										C		C				C		
14H-CC, 21	127.41	138.76	G	A								R										C	F	C				A		
15H-CC, 24	137.03	149.18	G	A																		A		C				A		
16H-4, 75	141.69	154.49	G	A								F		R			R					C	F	F				A		
16H-5, 75	143.20	156.00	G	A								F		R			R					C	F	F		R		A	R	
16H-6, 75	144.72	157.52	G	A								F		R			R					C	F	F		R		A	R	
16H-7, 40	145.88	158.68	G	A								F		R			R					C	F	F		F		A	R	

Table T10 (continued).

Core, section, interval (cm)	Depth (mbsf)	Depth (mcd)	Preservation	Abundance	*Amaurolithus primus/delicatus*	*Calcidiscus macintyrei*	*Calcidiscus premacintyrei*	*Ceratolithus armatus*	*Ceratolithus cristatus*	*Coccolithus miopelagicus*	*Cyclicargolithus floridanus*	*Discoaster brouweri*	*Discoaster loeblichii*	*Discoaster pentaradiatus*	*Discoaster quinqueramus/berggrenii*	*Discoaster surculus*	*Discoaster tamalis*	*Discoaster variabilis* gr.	*Emiliania huxleyi*	*Gephyrocapsa* spp. (large)	*Gephyrocapsa* spp. (medium)	*Gephyrocapsa* spp. (small)	*Helicosphaera sellii*	*Pseudoemiliania lacunosa*	*Reticulofenestra asanoi*	*Reticulofenestra pseudoumbilicus* >7 µm	*Reticulofenestra rotaria*	*Reticulofenestra* <7 µm	*Sphenolithus abies/neoabies*	*Sphenolithus heteromorphus*
16H-CC, 21	146.45	159.25	M	A								F		R			R						F	F		R		A	R	
17H-2, 75	148.16	161.21	G	A								F		R			R						F	F		R		A	R	
17H-4, 75	151.19	164.24	G	A								F		R			R						F	F		R		A	R	
17H-5, 75	152.71	165.76	G	A								F		R			R						F	F		R		A	R	
17H-6, 75	154.23	167.28	G	A								F		R			R						F	R		R		A	R	
17H-7, 40	155.40	168.45	G	A								F		R			R						F			R		A	R	
17H-CC, 25	155.98	169.03	G	A					R			F											F			F		A	F	
18H-CC, 25	164.90	179.90	G	A								F						R								F		A	R	
19H-CC, 23	174.94	189.24	M	A					R			R											C			R		A	R	
20X-CC, 27	184.21	199.37	M	A								R				R										R	R	A	R	
21X-CC, 37	189.01	205.03	M	A								R		R	R	R								R		R		A	F	
22X-CC, 27	198.69	215.57	M	A																						R		A		
23X-CC, 35	208.44	226.18	M	A					R							R										R		A	R	
24X-CC, 30	217.56	236.16	M	A											R									R		R		A	F	
25X-CC, 28	227.37	246.83	M	A					R							R										R		A	F	
26X-CC, 30	236.96	257.28	M	A											R	R										F		A		
27X-CC, 33	246.24	267.42	M	A				R				R		R			R	R								F		A	R	
28X-CC, 33	255.79	277.83	M	A				R	R						R	R	R									F		A	R	
29X-CC, 30	265.19	288.09	M	A					R			R				R										R		A	R	
30X-CC, 1	274.23	297.99	M	A								R				R										C		A	C	
31X-CC, 34	284.91	309.53	M	A								R			R	R										C		C	F	
32X-CC, 30	292.88	318.36	M	A																						C		C	A	
33X-CC, 39	304.22	330.56	M	A					R			R				R										C		C	A	
34X-CC, 34	313.75	340.95	M	A	R			R	R					R	R	R										C		C	C	
35X-CC, 35	319.53	347.59	M	A					R			R		R	R	R		R								C		A	C	
36X-CC, 47	333.22	362.14	M	A					R			F		R												C		A	C	
37X-CC, 22	342.54	372.32	M	A	R				R					R	R	R										F		A	C	
38X-1, 75	343.15	373.79	M	A					R					R	R	R										F		A	C	
38X-2, 75	344.66	375.30	M	A										R	R	R										F		A	C	
38X-3, 75	346.17	376.81	M	A				R						R	R	R										F		A	C	
38X-CC, 34	352.28	382.92	M	A	R							R		R	R	R										F		A	C	
39X-1, 75	352.75	384.25	M	A								R		R	R	R										F		A	C	
39X-3, 75	355.77	387.27	M	A				R				R		R		R										F		A	C	
39X-5, 75	358.77	390.27	M	A				R				R		R	R	R										F		A	C	
39X-6, 60	359.64	391.14	M	A				R				R		R	R	R										F		A	C	
39X-CC, 1	359.76	391.26	M	VA				R				R				R										R		C	C	
40X-1, 75	362.45	394.81	M	A				R				R			R	R										R		A	C	
40X-2, 75	363.96	396.32	M	A				R				R			R	R										R		A	C	
40X-3, 75	365.47	397.83	M	A								R				R										R		A	C	
40X-4, 75	366.98	399.34	M	A				R				R			R	R										R		A	C	
40X-5, 75	368.49	400.85	M	A				R				R			R	R										R		A	C	
40X-6, 75	370.00	402.36	M	A				R				R				R										R		A	C	
40X-CC, 34	371.64	404.00	M	A				R				R			R											R		C	C	
41X-2, 75	373.56	406.78	M	A				R				R														R		C	C	
41X-4, 75	376.58	409.80	M	A				R				R			R											R		C	C	
41X-6, 75	379.60	412.82	M	A				R				R			R											R		C	C	
41X-7, 40	380.76	413.98	M	A				R				R														R		C	C	
41X-CC, 34	381.19	414.41	M	A				R				R			R	R										F		C	C	
42X-1, 75	381.75	415.83	M	A								R			R	R										F		C	C	
42X-2, 75	383.26	417.34	M	A								R				R										F		C	C	
42X-3, 75	384.77	418.85	M	A								R			R	R										F		C	C	
42X-CC, 39	389.02	423.10	G	A								R		R				R								F		A	C	
43X-CC, 37	400.53	435.47	M	A										R	R											C		A	C	
44X-CC, 40	410.16	445.96	M	A										R	R											C		A	R	
45X-CC, 37	419.82	456.48	M	A								R			R	R										C		A	C	
46X-CC, 31	429.18	466.70	M	A								F			F	F										C		A	C	
47X-3, 75	432.77	471.15	M	A								F			F	F										C		A	C	
47X-5, 75	435.78	474.16	M	A								F			F	F										C		A	C	

Table T10 (continued).

Core, section, interval (cm)	Depth (mbsf)	Depth (mcd)	Preservation	Abundance	*Amaurolithus primus/delicatus*	*Calcidiscus macintyrei*	*Calcidiscus premacintyrei*	*Ceratolithus armatus*	*Ceratolithus cristatus*	*Coccolithus miopelagicus*	*Cyclicargolithus floridanus*	*Discoaster brouweri*	*Discoaster loeblichii*	*Discoaster pentaradiatus*	*Discoaster quinqueramus/berggrenii*	*Discoaster surculus*	*Discoaster tamalis*	*Discoaster variabilis* gr.	*Emiliania huxleyi*	*Gephyrocapsa* spp. (large)	*Gephyrocapsa* spp. (medium)	*Gephyrocapsa* spp. (small)	*Helicosphaera sellii*	*Pseudoemiliania lacunosa*	*Reticulofenestra asanoi*	*Reticulofenestra pseudoumbilicus* >7 µm	*Reticulofenestra rotaria*	*Reticulofenestra* <7 µm	*Sphenolithus abies/neoabies*	*Sphenolithus heteromorphus*
47X-6, 75	437.29	475.67	M	A								F			F	F										F		A	C	
47X-7, 52	438.37	476.75	M	A								F				F												A	C	
47X-CC, 33	438.85	477.23	M	A								R						R										A	C	
48X-CC, 33	448.48	487.72	M	A											R	R		R								F		A	C	
49X-CC, 28	458.10	498.20	M	A								F			F	F										F		A	A	
50X-CC, 31	467.80	508.76	M	A														R								F		A		
51X-CC, 35	477.47	519.29	M	A								R	R		R	R		R										A		
52X-CC, 32	485.01	527.69	M	A						R	F															F		C		R
53X-CC, 8	491.35	534.89	M	F			R			R	F															F		C		R
54X-CC, 27	504.71	549.11	M	A						R	F															F		C		R
55X-CC, 1	511.72	556.98	M	A						R	F															F		C		R

Notes: Preservation: G = good, M = moderate. Abundance: VA = very abundant, A = abundant, C = common, F = few, R = rare, T = trace.

Table T11. Distribution of foraminifers, Hole 1239A. (See table notes. Continued on next page.)

Core, section, interval (cm)	Depth (mbsf)	Depth (mcd)	Preparation	Preservation	Abundance	Benthic/planktonic foraminifers (%)	Remarks	*Dentoglobigerina altispira*	*Globigerina bulloides*	*Globigerina quinqueloba*	*Globigerinoides conglobatus*	*Globigerinoides extremus*	*Globigerinoides obliquus*	*Globigerinoides ruber* pink	*Globigerinoides trilobus*	*Globoquadrina dehiscens*	*Globorotalia conoidea*	*Globorotalia crassaformis*	*Globorotalia crassula*	*Globorotalia exilis*	*Globorotalia inflata*	*Globorotalia limbata*	*Globorotalia margaritae*	*Globorotalia menardii*	*Globorotalia peripheroacuta*	*Globorotalia peripheroronda*	*Globorotalia plesiotumida*	*Globorotalia praemenardii*	*Globorotalia pseudomiocenica*	*Globorotalia puncticulata*	*Globorotalia ruber* white	*Globorotalia sacculifer*	*Globorotalia scitula*	*Globorotalia tosaensis*	*Globorotalia tumida*	*Globorotalia ungulata*	*Globorotalia fohsi*	*Neogloboquadrina acostaensis*	*Neogloboquadrina dutertrei*	*Neogloboquadrina pachyderma*	*Orbulina suturalis*	*Orbulina universa*	*Pulleniatina obliquiloculata*	*Pulleniatina finalis*	*Pulleniatina praecursor*	*Pulleniatina primalis*	*Sphaeroidinella dehiscens*	*Sphaeroidinellopsis seminula*
202-1239A-																																														
Mudline	0.00	0.00	S	G	A	1/99	Radiolarians: R																	C						R	R			R					A	R		R						
1H-CC, 9	3.44	3.44	S	G	A	1/99	Radiolarians: R		F	F														C						R	F			R					A	R		R	F					
2H-CC, 20	12.85	13.00	S	G	A	1/99	Radiolarians: R		F	F				F										C						R	F			R					A	R		R						
3H-CC, 18	22.88	24.28	S	G	A	1/99	Radiolarians: R		F	F								F	F		F			F						F	F	F		R					F	C		R						
4H-CC, 26	32.39	34.59	S	G	A	1/99	Radiolarians: R		F	F											R			C								R	F							C	C		C		R				
5H-CC, 22	41.91	45.66	S	G	A	1/99	Radiolarians: C		F	F			F											F						F										C			C		F				
6H-CC, 35	51.50	56.10	S	G	A	1/99	Radiolarians: F		F	F			F											C						R	R									C	R		C		F				
7H-CC, 24	60.91	66.16	S	G	A	1/99	Radiolarians: F		F	F		R												C								F	R					C	C	R		C	F	R			R		
8H-CC, 31	70.46	76.41	S	G	A	1/99	Radiolarians: R		F	F														F								F	R					C	F	R		C	C					
9H-CC, 21	79.96	87.26	S	G	A	1/99	Radiolarians: F		F	F										R				F								F	R	F				F	C	F		C	F					
10H-CC, 30	89.43	97.23	S	M	F	1/99	Radiolarians: A																	F										F				C			R					R	
11H-CC, 21	98.83	107.73	S	M	R/F	33/67	Radiolarians: A																											F	R		F	R	F	F	F						
12H-CC, 35	108.48	118.28	S	M	F	30/60	Radiolarians: A						F								R		F		F								F				F	F			F						
13H-CC, 23	117.88	128.68	S	M/G	C	10/90	Radiolarians: C					R	F																R					F				F	C			F	F				
14H-CC, 21	127.41	138.76	S	M	C	1/99	Radiolarians: R								F							F							F					R				F	C			F					
15H-CC, 24	137.03	149.18	S	M	F	35/65	Radiolarians: A					R	F																		R			F	R	R			F	F	F		C	F				
16H-CC, 21	146.45	159.25	S	M	R/F	50/50	Radiolarians: A								R							R							R									F	R			R	R				
17H-CC, 25	155.98	169.03	S	M	F/C	15/85	Radiolarians: C								F																		F					F	F	R		F					
18H-CC, 25	164.90	179.90	S	M	F	50/50	Radiolarians: A					R			R							R																R	R			R					
19H-CC, 23	174.94	189.24	S	P/M	R	40/60	Radiolarians: A								R																		R					R			R						
20X-CC, 27	184.21	199.37	S	M	F/C	30/70	Radiolarians: C					R			F							F							F									F	F	F							
21X-CC, 37	189.01	205.03	S	P/M	R	50/50	Radiolarians: A								F							F			F							F	F				F	F			F					
22X-CC, 27	198.69	215.57	S	P/M	T/R		BF R																																								
23X-CC, 35	208.44	226.18	S	M	F	20/80	Radiolarians: C	R							F							F							R	R		R	F		F			C	C	R		C						
24X-CC, 30	217.56	236.16	S	M	F	20/80	Radiolarians: F								F							F							F	F		R	F		R			F	F	F		R			R		
25X-CC, 28	227.37	246.83	S	M	F/C	25/75	Radiolarians: C								F							F		F					F				R		F			F	F	R		F		F			F
26X-CC, 30	236.96	257.28	S	M	R/F	45/55	Radiolarians: A	F				R			F						R	F	R	R										F				F	F	F		F					F
27X-CC, 33	246.24	267.42	S	M	F	45/55	Radiolarians: A	F					F		F							F	R	F					F				F					F	F			R			R		F
28X-CC, 33	255.79	277.83	S	M	F	50/50	Radiolarians: A	F							F							F	F						F				F					F	F	R		F					F
29X-CC, 30	265.19	288.09	S	P/M	F	60/40	Radiolarians: A	F							F		R					F	R						R				F						F			F					F
30X-CC, 1	274.23	297.99	S	P/M	R	70/30	Radiolarians: A						R		R															R			R	R				F	F	F		R					
31X-CC, 34	284.91	309.53	S	M	F	65/35	Radiolarians: A	F					F									F	C						C	F			F					F	C			F					R
32X-CC, 38	292.96	318.44	S	M	F	20/80	Radiolarians: C	F							F							F	F						F				F					F	C	F		F					R
33X-CC, 39	304.22	330.56	S	M		25/75	Radiolarians: C	F					F		F							F	F						F						C			C	F	F		F					F
34X-CC, 34	313.75	340.95	S	M	R/F	50/50	Radiolarians: A								F								R				F		F									F		F		R					R
35X-CC, 35	319.53	347.59	S	M/G	F	65/35	Radiolarians: A	F							F							F	R					F	R		R										F			R		F
36X-CC, 47	333.22	362.14	S	M	F	35/65	Radiolarians: C	F					F		F							F							F									F									F
37X-CC, 22	342.54	372.32	S	M	F	45/55	Radiolarians: A	F					F		F							F	F						F									F		F		F					F
38X-CC, 34	352.28	382.92	S	M	F	30/70	Radiolarians: C	F					F		F							C							F									F		F		F					F

Table T11 (continued).

Core, section, interval (cm)	Depth (mbsf)	Depth (mcd)	Preparation	Preservation	Abundance	Benthic/planktonic foraminifers (%)	Remarks	*Dentoglobigerina altispira*	*Globigerina bulloides*	*Globigerina quinqueloba*	*Globigerinoides conglobatus*	*Globigerinoides extremus*	*Globigerinoides obliquus*	*Globigerinoides ruber* pink	*Globigerinoides trilobus*	*Globoquadrina dehiscens*	*Globorotalia conoidea*	*Globorotalia crassaformis*	*Globorotalia crassula*	*Globorotalia exilis*	*Globorotalia inflata*	*Globorotalia limbata*	*Globorotalia margaritae*	*Globorotalia menardii*	*Globorotalia peripheroacuta*	*Globorotalia peripheronda*	*Globorotalia plesiotumida*	*Globorotalia praemenardii*	*Globorotalia pseudomiocenica*	*Globorotalia puncticulata*	*Globorotalia ruber* white	*Globorotalia sacculifer*	*Globorotalia scitula*	*Globorotalia tosaensis*	*Globorotalia tumida*	*Globorotalia ungulata*	*Globorotalia fohsi*	*Neogloboquadrina acostaensis*	*Neogloboquadrina dutertrei*	*Neogloboquadrina pachyderma*	*Orbulina suturalis*	*Orbulina universa*	*Pulleniatina obliquiloculata*	*Pulleniatina finalis*	*Pulleniatina praecursor*	*Pulleniatina primalis*	*Sphaeroidinella dehiscens*	*Sphaeroidinellopsis seminula*
39X-CC, 1	359.76	391.26	S	M	F	45/55	Radiolarians: C	F					F		F							F	F	F				F							F	F	F		R						F
40X-CC, 34	371.64	404.00	C	M	F	50/50	Radiolarians: C	C					F		F	R						C		R					R										F				R		F
41X-CC, 34	381.19	414.41	C	M	R	99/1	Radiolarians: A	R					R		R							R	R	R															R						R
42X-CC, 39	389.02	423.10	C	M	R	99/1	Radiolarians: C	R					R		R							R																	R				R	R	R
43X-CC, 37	400.53	435.47	C	P/M	R	99/1	Radiolarians: A								R							R																	R						
44X-CC, 40	410.16	445.96	C	M	R	99/1	Radiolarians: A								R							R																	R						
45X-CC, 37	419.82	456.48	C	M	R/F	99/1	Radiolarians: A				R		R		R							R																	R				R		
46X-CC, 31	429.18	466.70	C	P/M	R	99/1	Radiolarians: A	R					R									R	R																R						R
47X-CC, 33	438.85	477.23	C	M	F	99/1	Radiolarians: A	R					R											R															R						R
48X-CC, 33	448.48	487.72	C	M	R/F	99/1	Radiolarians: C	F					R		F	R						F		R															F						R
49X-CC, 28	458.10	498.20	C	M	R/F	99/1	Radiolarians: C						R											R																					
50X-CC, 31	467.80	508.76	C	M	R	90/1	Radiolarians: C	F							F							F		R				R										F						F
51X-CC, 35	477.47	519.29	C	P	T/R	100/0	Radiolarians: A																																						
52X-CC, 32	485.01	527.69	C	P/M	F/C	15/1	Radiolarians: F	C							F	R																					F								F
53X-CC, 8	491.35	534.89	C	P	R	10/1	Glauconite: A								F											F	F																		
54X-CC, 27	504.71	549.11	C	P/M	R	10/90																				F		F																
55X-CC, 0	511.71	556.97	C	P	R	15/85																					F	F																

Notes: Preparation: S = sieve, C = Calgon. Preservation: G = good, M = moderate, P = poor. Abundance: A = abundant, C = common, F = few, R = rare, T = trace.

Table T12. Distribution of diatoms, Hole 1239A. (See table notes. Continued on next page.)

Core, section, interval (cm)	Depth (mbsf)	Depth (mcd)	Identification	Method	Abundance	Preservation	*Actinocyclus ellipticus*	*Actinocyclus ellipticus* v. *lanceolata*	*Actinocyclus* spp.	*Actinoptychus senarius*	*Asteromphalus elegans*	*Asteromphalus* spp.	*Azpeitia nodulifera*	*Chaetoceros* spp. (resting spores)	*Coscinodiscus* spp.	*Diploneis bombus*	*Hemidiscus cuneiformis*	*Nitzschia cylindrica*	*Nitzschia marina*	*Nitzschia miocenica*	*Nitzschia porteri*	*Nitzschia reinholdii*	*Nitzschia fossilis*	*Nitzschia jouseae*	*Paralia sulcata*	*Pseudoeunotia doliolus*	*Rhizosolenia* spp.	*Rhizosolenia matuyama*	*Rhizosolenia praebergonii robusta*	*Rhizosolenia praebergonii*	*Rossiela paleacea*	*Stephanopyxis* spp.	*Thalassionema* spp.	*Thalassiosira* spp.	*Thalassiosira burckliana*	*Thalassiosira convexa*	*Thalassiosira convexa aspinosa*	*Thalassiosira miocenica*	*Thalassiosira oestrupii*	*Thalassiosira praeconvexa*	*Thalassiothrix*	Remarks
202-1239A-																																									
Mudline	0.00	0.00	PAL	S	F–C	M							R				R								F						F	F	F					F			*Cyclotella*
1H-CC, 9	3.44	3.44	PAL	S	F	P						R	C		F				F				F		F	F						C	F–C					F	F	*Cyclotella*
2H-CC, 20	12.85	13.00	PAL	S	F	P				R			F		F		T					F		R	F		F				T	F							F	
3H-CC, 18	22.88	24.28	PAL	S	F	P		R		F		T	R		R							F	F			T			R–F			F							R–F	
4H-CC, 26	32.39	34.59	PAL	S	F–C	P–M		F		F		T	F										F	T					F			F	F	F		F		F		
5H-4, 75	37.16	40.91	Toothpick	S	F	P	T	F		R–F									R			T		T–R					R	R			F			R			F		
5H-6, 75	40.18	43.93	Toothpick	S	F	P–M	R	F		R–F			F				F		F			R–F	F	F	T		R									R					
5H-CC, 22	41.91	45.66	PAL	S	F	P–M							F				R–F		R–F			R		R–F			R						C			R–F			F–C		
6H-CC, 35	51.50	56.10	PAL	S	F	P		R–F	R–F	R			F			T			R			T					T				R				F					
7H-1, 75	51.65	56.90	Toothpick	S	C	M				T			T			T						T		R	T		T					F				T			F		
7H-2, 75	53.15	58.40	Toothpick	S	F–C	P–M			T				T										T	R								R								
7H-4, 75	56.15	61.40	Toothpick	S	C	G							C						F			F		F										T							
7H-CC, 24	60.91	66.16	PAL	S	C	M			T	F			T											F								T							T		
8H-CC, 31	70.46	76.41	PAL	S	C	M																																				
9H-CC, 21	79.96	87.26	PAL	S	C	M	F		R	F			F		F			T						R		T		R					F							F	*Thalassionema-Thalassiothrix* fragments VA
10H-CC, 30	89.43	97.23	PAL	S	C	M			F				F						F	R		F											F							F	
11H-2, 75	91.16	100.06	Toothpick	S						F			F–C				R			T												F–C	F				T			
11H-4, 75	94.18	103.08	Toothpick	S				R		R					T				F			F										F		T					F	
11H-CC, 21	98.83	107.73	PAL	S	F–C	M		R	R	T			F						R	T	T						R					F	R			R	F		T	F	
12H-CC, 35	108.48	118.28	PAL	S	C	M–G				T		T	F							F	T	T	T										T	T						F	*Actynocyclus moronensis*
13H-CC, 23	117.88	128.68	PAL	S	F	P																											T							T	
14H-CC, 21	127.41	138.76	PAL	S	F	P–M																											T							T	
15H-CC, 24	137.03	149.18	PAL	S	F	P																																			
16H-CC, 21	146.45	159.25	PAL	S	C–A	M–G			R	F			F–C	C			F		F				F			F	F						C	F–C				F		F	
17H-CC, 25	155.98	169.03	PAL	S	C	M			R	F			F	C	R		F		F			F	R				F			F		R	C	F–C						F	
18H-CC, 25	164.90	179.90	PAL	S	C	M			F	F		R	F	F			F		F				F			F	F						C	C				F		F	
19H-CC, 23	174.94	189.24	PAL	S	C–A	M–G				F		T	F	F	F		F		F							F	R					T	F	F				F		F	
20X-CC, 27	184.21	199.37	PAL	S	F–C	M							F	F												F	F						F	F				F		F	
21X-CC, 37	189.01	205.03	PAL	S	F	P–M							F	F	F		R						T				R		T				F–C	F–C				F		F	*Cyclotella*
22X-3, 75	192.67	209.55	Toothpick	S	C	M	T					T	F	F								T				F	R						F	F						F	
22X-5, 75	195.69	212.57	Toothpick	S	C	M						F	F	F	F								F			F	R	R					F								
22X-7, 40	198.36	215.24	Toothpick	S	F–C	P–M						R	F	F	F		F						R			F	F	F					F	F						F	
22X-CC, 27	198.69	215.57	PAL	S	C	M–G			R	R			F	F	F		R		F				R			F	F	F					F	F						F	
23X-CC, 35	208.44	226.18	PAL	S	F	M–G			F	R		R	F	F	R–F		R–F		F				F			F	R						F	F				F		F	
24X-CC, 30	217.56	236.16	PAL	S	R–F	P–M				R			F	F	F				F			F				T	F					R	F–C	F–C				F		R	
25X-CC, 28	227.37	246.83	PAL	S	C	M				T			F	F	F	T	F		F			T	F		T	R	F					F	F	R–F				F		F	

Table T12 (continued).

Core, section, interval (cm)	Depth (mbsf)	Depth (mcd)	Identification	Method	Abundance	Preservation	*Actinocyclus ellipticus*	*Actinocyclus ellipticus* v. *lanceolata*	*Actinocyclus* spp.	*Actinoptychus senarius*	*Asteromphalus elegans*	*Asteromphalus* spp.	*Azpeitia nodulifera*	*Chaetoceros* spp. (resting spores)	*Coscinodiscus* spp.	*Diploneis bombus*	*Hemidiscus cuneiformis*	*Nitzschia cylindrica*	*Nitzschia marina*	*Nitzschia miocenica*	*Nitzschia porteri*	*Nitzschia reinholdii*	*Nitzschia fossilis*	*Nitzschia jouseae*	*Paralia sulcata*	*Pseudoeunotia doliolus*	*Rhizosolenia* spp.	*Rhizosolenia matuyama*	*Rhizosolenia praebergonii robusta*	*Rhizosolenia praebergonii*	*Rossiela paleacea*	*Stephanopyxis* spp.	*Thalassionema* spp.	*Thalassiosira* spp.	*Thalassiosira burckliana*	*Thalassiosira convexa*	*Thalassiosira convexa aspinosa*	*Thalassiosira miocenica*	*Thalassiosira oestrupii*	*Thalassiosira praeconvexa*	*Thalassiothrix*	Remarks
26X-CC, 30	236.96	257.28	PAL	S	F	P–M			F				F	F			F										F			F			F							
27X-CC, 33	246.24	267.42	PAL	S	R	P			F	F			F	F					F				F				F						F	F				F		
28X-CC, 33	255.79	277.83	PAL	S	R–F	P–M			R	F			F	F								R	F		T		F			F			F	F					F	
29X-CC, 30	265.19	288.09	PAL	S	R–F	P			T	T		T	F	F			F		T				F	R			T				R–F	F		R–F					F	*Cyclotella*
30X-CC, 1	284.91	297.99	PAL	S	R	P	R	T	T	R			T	F			R		T					T–R			R					R–F			F–R				R–F	
31X-CC, 34	292.96	309.53	PAL	S	C	M							F	F			R		F					T								F	F						R	
32X-CC, 38	304.22	318.44	PAL	S	F	P			T	T		T	F	F	T				F				F	F								C	R			T			F	
33X-CC, 39	313.75	330.56	PAL	S	R–F	P–M			F	F			F	F			F					R		R			F			R		F	F						F	
34X-CC, 34	319.53	340.95	PAL	S	R–F	P		F	F	F			F	F				F	F			F										F			F					
35X-CC, 35	333.22	347.59	PAL	S	C	M			F				F	F			F	R									F			R		F	F						F	
36X-CC, 47	342.54	362.14	PAL	S	T	P	F	R	F	F			F	F		T				T							F			R		F							F	
37X-CC, 22	352.28	372.32	PAL	S	F	P–M				F			F	F			F	F	F	T			F									F							F	
38X-CC, 34	381.19	382.92	PAL	S	F	P							F	F				F	F	F							R					F	F			R			F	
39X-CC, 1	371.64	391.26	PAL	S	F	P–M		R	R	F		T	F	F–C			F		F			F	F	R			F			T–R		F	F		F	F	T–R		F	
40X-CC, 34	389.02	404.00	PAL	S	F	P	T	T		F			T	R			F–C		R			R	F						F	T		R	F	T		R		T		F	
41X-CC, 34	400.53	414.41	PAL	S	F	P				F			T	R					R				T				T						R–F		F					R	
42X-CC, 39	410.16	423.10	PAL	S	F	P	T	T	T				T	R			T							T			R						R		T			T		F	
43X-CC, 37	419.82	435.47	PAL	S	F	P	R	T	T				R–F	R	T		F		R				F	F–C			F						R–F	T		F	F		R	R–F	
44X-CC, 40	429.18	445.96	PAL	S	F	P–M			R	T			R	R			R					T		R			F						F		R–F	R–F				F	
45X-CC, 37	438.85	456.48	PAL	S	F–C	P–M				T			F	R					R–F					T									F							R–F	
46X-CC, 31	448.48	466.70	PAL	S	F–C	M				R				R	R		R		R								R				R		F	F						F	
47X-CC, 33	458.10	477.23	PAL	S	F–C	P–M	T			R		T	F	R–F			F					F				F	F					R	F	F–C				F			
48X-CC, 33	467.80	487.72	PAL	S	F–C	P–M			T	F			R–F	R–F	R		R						T						R–F					F	R						
49X-CC, 28	477.47	498.20	PAL	S	F–C	P–M		R	R	R			F	R–F			R		T			R	F	F	T		T		T			R	F–C		R	R–F		T		R	
50X-CC, 31	485.01	508.76	PAL	S	C–A	P–M	T			R			R	R–F				T	T					R–F									R–F	R	R					R–F	
51X-CC, 35	491.35	519.29	PAL	S	F	P			T	F			F–C	T	T		F		R			T	F	R			T		T	R		F	T	T	R	R–F		T		T	
52X-CC, 32	504.71	527.69	PAL	S	T	P	T	T		T			F–C	T			F		T			R	R	F			R			R		F	F	F	T	R				F	
53X-CC, 8	511.71	534.89	PAL	S	T	P				T			F	T			R		R		T		T				T						F–C	T						F	
54X-CC, 27	504.63	549.11	PAL	S	R	P								T					R	F			T										F			F	R			F	
55X-CC, 0	511.69	556.97	PAL	S	B	—								T	T	T																	T							T	

Notes: PAL = paleontology sample. S = smear slide. Abundance: A = abundant, C = common, F = few, R = rare, T = trace, B = barren. Preservation: G = good, M = moderate, P = poor.

Table T13. Headspace gas concentrations and C_1/C_2 ratios, Hole 1239A.

Core, section, interval (cm)	Depth (mbsf)	Depth (mcd)	Instrument	C_1 (ppmv)	C_2 (ppmv)	C_1/C_2	C_2= (ppmv)	C_3 (ppmv)	*i*-C_4 (ppm)	*n*-C_4 (ppm)	*i*-C_5 (ppm)	CO_2 (ppm)
202-1239A-												
1H-3, 0–5	2.52	2.52	GC	2								
2H-4, 0–5	7.90	8.05	GC	4								
3H-4, 0–5	17.42	18.82	GC	6								
4H-4, 0–5	26.93	29.13	GC	15								
5H-4, 0–5	36.41	40.16	GC	28								
6H-4, 0–5	45.92	50.52	GC	71	1.2	59						
7H-4, 0–5	55.40	60.65	GC	131	1.5	87						
8H-4, 0–5	64.94	70.89	GC	1,882	2.1	896						
9H-4, 0–5	74.43	81.73	GC	7,634	2.9	2,632						
10H-4, 0–5	83.93	91.73	GC	18,713	4.9	3,819						
11H-4, 0–5	93.43	102.33	GC	25,051	6.0	4,175						
12H-4, 0–5	102.93	112.73	GC	32,194	7.9	4,075						
13H-4, 0–5	112.45	123.25	GC	48,976	8.6	5,695		4.3				
14H-4, 0–5	121.95	133.30	GC	47,735	7.7	6,199						
15H-4, 0–5	131.44	143.59	GC	40,548	6.6	6,144						
16H-4, 0–5	140.94	153.74	GC	66,563	11.4	5,839		6.9				
17H-4, 0–5	150.44	163.49	GC	52,319	9.3	5,626		4.7				
18H-4, 0–5	159.93	174.93	GC	20,550	4.7	4,372						
19H-4, 0–5	169.45	183.75	GC	39,097	8.5	4,600		6.7				
20X-4, 0–5	178.92	194.08	GC	39,794	8.5	4,682		7.0				
21X-4, 0–5	183.74	199.76	GC	36,491	9.0	4,055		7.8				
22X-4, 0–5	193.43	210.31	GC	37,086	9.9	3,746	0.7	9.6				
23X-4, 0–5	203.14	220.88	GC	9,407	3.5	2,688		3.8				
24X-4, 0–5	212.80	231.40	NGA	42,048				12.5	1.5	2.1	2.9	109,740
25X-4, 0–5	222.02	241.48	NGA	11,250				4.4		0.8	1.1	
26X-4, 0–5	231.71	252.03	NGA	56,748				11.5	1.2	1.5	2.0	
28X-4, 0–5	250.62	272.66	GC	62,449	14.8	4,220		12.8				
29X-4, 0–5	260.22	283.12	NGA	37,188				8.5	0.8	1.1	1.3	
30X-4, 0–5	269.80	293.56	GC	45,334	12.2	3,716		12.0				
31X-4, 0–5	279.50	304.12	GC	38,847	13.1	2,965	0.5	15.3				
32X-4, 0–5	289.12	314.60	GC	39,104	10.3	3,797		9.3				
33X-4, 0–5	298.80	325.14	GC	51,010	13.2	3,864		10.8				
34X-4, 0–5	308.41	335.61	NGA	52,405				14.3	1.3	1.7	2.0	83,159
35X-2, 0–5	315.01	343.07	NGA	39,554				8.3	0.7	1.0	1.2	78,177
36X-4, 0–5	327.72	356.64	GC	58,751	16.8	3,497		14.3				
37X-4, 0–5	337.33	367.11	GC	43,794	11.8	3,711		9.3				
38X-4, 0–5	346.91	377.55	GC	39,826	13.0	3,064		11.8				
39X-4, 0–5	356.52	388.02	GC	42,015	14.8	2,839		15.7				
40X-4, 0–5	366.23	398.59	NGA	26,948				5.7				45,753
41X-4, 0–5	375.83	409.05	NGA	59,042				14.9				64,815
42X-4, 0–5	385.52	419.60	NGA	26,274				6.3				43,727
43X-4, 0–5	395.12	430.06	NGA	52,210				6.6				49,970
44X-4, 0–5	404.72	440.52	NGA	16,664								37,112
45X-4, 0–5	414.45	451.11	NGA	16,954				6.3				33,724
45X-4, 0–5	414.45	451.11	GC	22,063	11.2	1,970	0.7	7.5				
46X-4, 0–5	423.92	461.44	NGA	7,938								16,636
47X-4, 0–5	433.52	471.90	NGA	33,542								40,604
48X-4, 0–5	443.22	482.46	NGA	32,193								27,493
49X-4, 0–5	452.82	492.92	NGA	20,944								24,318
50X-4, 0–5	462.52	503.48	NGA	21,740								20,083
51X-4, 0–5	472.13	513.95	NGA	12,603								18,861
52X-4, 0–5	481.73	524.41	NGA	19,761								16,594
53X-3, 0–5	489.51	533.05	NGA	23,230								13,456
54X-4, 0–5	500.64	545.04	NGA	4,185								6,203
55X-3, 0–5	508.71	553.97	GC	31,662	19.0	1,666						

Note: GC = gas chromatograph, NGA = natural gas analyzer.

Table T14. Interstitial water geochemical data, Hole 1239A.

Core, section, interval (cm)	Depth (mbsf)	Depth (mcd)	pH	Alkalinity (mM)	Salinity	Cl^- (mM)	Na^+ (mM)	SO_4^{2-} (mM)	HPO_4^{2-} (µM)	NH_4^+ (mM)	H_4SiO_4 (µM)	Mn^{2+} (µM)	Fe^{2+} (µM)	Ca^{2+} (mM)	Mg^{2+} (mM)	B (µM)	Sr^{2+} (µM)	Ba^{2+} (µM)	Li^+ (µM)	K^+ (mM)
202-1239A-																				
1H-1, 145–150	1.45	1.45	7.08	3.0	34.0	553	478	28.0	5.5	BDL	545	1.2	1.9	10.1	50.7	469	87	BDL	24	11.9
2H-3, 145–150	7.85	8.00	7.56	3.7	34.0	554	477	26.5	6.4	0.33	632	1.3	0.7	9.9	51.1	472	86	BDL	24	11.9
3H-3, 145–150	17.36	18.76	7.55	7.0	33.0	558	479	24.1	8.3	0.97	757	0.6	2.5	9.7	51.5	472	94	BDL	27	12.1
4H-3, 145–150	26.87	29.07	7.50	11.3	34.0	562	486	20.3	10.4	1.65	1014	0.2	2.5	8.3	49.7	498	110	BDL	34	12.1
5H-3, 145–150	36.36	40.11	7.51	14.9	33.0	569	493	14.4	17.5	2.31	916	0.2	8.7	7.0	46.7	515	127	1	42	12.3
6H-3, 145–150	45.86	50.46	7.40	17.7	34.0	563	487	9.5	19.4	3.30	937	0.2	6.8	6.1	44.5	528	145	1	49	12.0
7H-3, 145–150	55.35	60.60	7.46	20.4	35.0	559	481	4.5	20.2	3.51	948	0.5	6.7	5.8	41.7	532	161	1	54	12.0
8H-3, 145–150	64.87	70.82	7.82	24.0	33.0	562	486	BDL	20.2	4.40	1003	BDL	1.4	5.5	38.7	573	184	17	63	12.1
9H-3, 145–150	74.38	81.68	7.43	—	33.0	565	—	BDL	25.3	4.26	975	0.2	6.7	5.5	37.8	557	195	762	67	11.9
10H-3, 145–150	83.86	91.66	7.36	28.4	34.0	563	494	BDL	36.5	4.92	1052	2.0	12.6	5.7	37.1	599	217	1210	70	11.9
11H-3, 145–150	93.37	102.27	7.32	29.6	33.0	562	495	BDL	23.8	4.69	1035	BDL	0.5	6.0	36.6	602	225	1460	75	11.6
12H-3, 145–150	102.87	112.67	7.35	28.4	33.0	563	496	BDL	20.9	5.23	1030	BDL	2.2	6.2	35.7	602	241	1592	82	11.6
13H-3, 145–150	112.39	123.19	7.15	28.3	33.0	562	497	BDL	18.7	5.72	1090	0.6	0.7	6.3	34.6	613	241	1591	85	11.6
14H-3, 145–150	121.88	133.23	7.24	25.6	33.0	565	500	BDL	19.2	6.07	1155	0.3	17.9	6.3	33.3	608	245	1633	89	11.6
15H-3, 145–150	131.38	143.53	7.32	24.6	33.0	563	495	BDL	17.5	6.19	1123	0.2	6.3	6.9	33.5	574	238	1345	91	11.7
16H-3, 145–150	140.88	153.68	7.22	24.6	33.0	560	494	BDL	16.0	6.43	1134	BDL	2.7	6.9	32.6	597	242	1288	95	11.3
17H-3, 145–150	150.37	163.42	7.26	25.3	33.0	557	493	BDL	15.7	6.52	1139	0.2	5.7	7.6	31.4	611	266	1493	101	11.1
18H-3, 145–150	159.87	174.87	7.13	24.9	33.0	559	495	BDL	10.9	6.99	1172	0.2	12.8	7.6	31.0	621	274	1628	104	11.3
19H-3, 145–150	169.38	183.68	7.23	24.2	33.0	560	496	BDL	14.5	6.90	1161	BDL	1.8	8.1	30.5	592	270	1495	105	11.3
20X-3, 145–150	178.87	194.03	7.15	25.7	33.0	560	498	BDL	13.2	7.30	1188	BDL	11.0	8.4	30.1	617	278	1423	109	10.9
21X-3, 145–150	183.68	199.70	7.32	24.3	33.0	563	499	BDL	10.0	6.52	1128	0.2	10.1	8.6	30.1	614	259	782	108	10.9
23X-3, 145–150	203.08	220.82	6.99	21.5	33.0	560	494	BDL	7.9	6.55	1193	0.4	5.5	9.2	29.5	576	205	162	101	10.5
25X-3, 145–150	221.95	241.41	6.91	19.3	33.0	558	492	BDL	5.7	6.62	1248	0.4	2.6	9.6	27.8	595	217	167	103	10.8
27X-3, 145–150	240.96	262.14	6.74	21.3	33.0	554	490	BDL	5.3	7.13	1346	0.4	2.1	10.2	27.0	645	298	612	112	10.9
29X-3, 145–150	260.15	283.05	6.68	17.8	33.0	556	489	BDL	5.5	6.52	1341	0.4	1.3	10.5	26.8	620	258	144	108	10.4
31X-3, 145–150	279.45	304.07	6.73	18.9	33.0	559	496	BDL	3.0	6.57	1466	0.3	5.3	10.9	24.9	647	324	404	117	10.0
33X-3, 145–150	298.76	325.10	6.84	16.8	33.0	556	491	BDL	3.6	6.40	1444	0.3	3.3	11.0	25.1	641	304	146	112	9.8
35X-1, 145–150	314.95	343.01	6.61	17.9	33.0	557	493	BDL	2.8	6.31	1608	0.4	4.1	12.1	23.9	660	310	95	113	10.0
36X-3, 145–150	327.67	356.59	6.73	14.7	33.0	556	491	BDL	2.8	6.57	1575	0.3	1.5	11.5	23.2	652	283	111	111	9.8
38X-3, 145–150	346.87	377.51	6.65	15.7	33.0	559	496	BDL	2.6	6.40	1668	0.3	1.9	12.3	22.5	671	384	624	113	9.7
40X-3, 145–150	366.17	398.53	6.78	14.0	32.0	559	493	BDL	2.8	5.79	1657	0.3	4.0	12.5	22.5	666	345	131	106	9.3
42X-3, 145–150	385.47	419.55	6.79	11.7	32.0	556	489	BDL	2.6	5.53	1597	0.3	2.5	12.8	22.2	666	329	64	99	9.0
44X-3, 145–150	404.67	440.47	6.55	12.1	33.0	561	497	BDL	2.6	5.56	1706	0.2	4.0	13.3	20.5	715	409	212	101	8.7
46X-3, 145–150	423.87	461.39	6.83	11.5	33.0	556	487	BDL	2.8	5.30	1755	BDL	0.6	14.0	21.8	731	451	590	99	8.8
48X-3, 140–150	443.12	482.36	6.63	8.3	32.0	557	494	BDL	2.6	5.53	1858	0.2	1.3	13.6	18.2	742	498	1050	96	7.7
49X-3, 140–150	452.72	492.82	6.42	8.3	32.0	556	490	BDL	2.6	5.32	1875	0.2	2.5	15.1	18.0	757	472	527	87	7.7
50X-3, 140–150	462.41	503.37	6.45	7.6	32.0	555	489	BDL	2.6	5.06	1847	0.3	2.9	15.0	18.0	766	500	852	88	7.7
51X-3, 140–150	472.02	513.84	6.29	6.2	32.0	556	488	BDL	2.3	4.73	1722	0.5	3.4	15.0	18.5	734	450	390	83	7.2
52X-2, 140–150	480.11	522.79	6.30	5.2	32.0	557	490	BDL	2.3	4.54	1564	1.1	5.2	15.0	17.9	730	450	419	79	6.9
53X-2, 140–150	489.40	532.94	6.77	4.4	32.0	557	489	BDL	2.3	4.59	1444	2.2	31.6	15.3	17.4	777	483	588	78	6.5
54X-3, 140–150	500.52	544.92	6.76	4.0	32.0	555	483	BDL	2.3	4.69	1428	3.3	9.8	16.7	18.2	721	454	372	74	6.6
55X-2, 140–150	508.60	553.86	6.19	3.6	31.0	558	467	BDL	2.3	5.04	1319	3.8	10.0	20.2	22.7	662	439	325	71	8.8

Notes: BDL = below detection limit (SO_4^{2-} = 1.0 mM, NH_4^+ = 0.19 mM, Mn^{2+} = 0.1 µM, Ba^{2+} = 0.1 µM). — = not determined.

Table T15. Inorganic carbon, calcium carbonate, total carbon, total organic carbon, total organic carbon on a carbonate-free basis, and total nitrogen concentrations, and TOC/TN ratios, Hole 1239A. (**See table note.** Continued on next two pages.)

Core, section, interval (cm)	Depth (mbsf)	Depth (mcd)	IC (wt%)	$CaCO_3$ (wt%)	TC (wt%)	TOC (wt%)	TOC CFB (wt%)	TN (wt%)	TOC/TN (atomic)
202-1239A-									
1H-1, 74–75	0.74	0.74	8.60	71.6	9.94	1.34	4.71	0.23	5.05
1H-2, 74–75	2.25	2.25	8.21	68.4					
1H-3, 40–41	2.92	2.92	5.29	44.0	6.22	0.93	1.65	0.17	4.66
2H-1, 74–75	4.14	4.29	7.23	60.2					
2H-2, 74–75	5.64	5.79	4.37	36.4	8.07	3.70	5.82	0.13	23.86
2H-3, 74–75	7.14	7.29	6.62	55.1					
2H-4, 74–75	8.64	8.79	6.57	54.8					
2H-5, 74–75	10.14	10.29	5.87	48.9	7.29	1.42	2.78	0.18	6.76
2H-6, 74–75	11.64	11.79	6.62	55.2					
3H-1, 74–75	13.64	15.04	8.24	68.6	8.96	0.72	2.29	0.13	4.73
3H-2, 74–75	15.15	16.55	4.04	33.7					
3H-3, 74–75	16.65	18.05	6.37	53.0					
3H-4, 74–75	18.16	19.56	1.92	16.0	2.45	0.53	0.63	0.03	15.49
3H-5, 74–75	19.67	21.07	6.50	54.1	7.69	1.19	2.59	0.12	8.42
3H-6, 74–75	21.18	22.58	6.59	54.9					
3H-7, 20–21	22.15	23.55	7.39	61.5					
4H-1, 74–75	23.14	25.34	5.92	49.3	7.24	1.32	2.61	0.17	6.74
4H-2, 74–75	24.65	26.85	6.82	56.8					
4H-3, 74–75	26.16	28.36	6.55	54.5					
4H-4, 74–75	27.67	29.87	5.96	49.7					
4H-5, 74–75	29.18	31.38	6.79	56.6	7.90	1.11	2.57	0.12	8.23
4H-6, 74–75	30.68	32.88	7.30	60.8					
4H-7, 20–21	31.64	33.84	7.05	58.7					
5H-1, 74–75	32.64	36.39	7.11	59.2	8.30	1.19	2.91	0.15	6.83
5H-2, 74–75	34.14	37.89	5.72	47.6					
5H-3, 74–75	35.65	39.40	6.51	54.3					
5H-4, 74–75	37.15	40.90	5.83	48.6					
5H-5, 74–75	38.66	42.41	6.55	54.5	7.52	0.97	2.14	0.10	8.48
5H-6, 74–75	40.17	43.92	7.28	60.6					
5H-7, 20–21	41.14	44.89	7.87	65.5					
6H-1, 74–75	42.14	46.74	6.98	58.2	8.22	1.24	2.97	0.17	6.41
6H-2, 74–75	43.65	48.25	7.49	62.4					
6H-3, 74–75	45.15	49.75	7.00	58.4					
6H-4, 74–75	46.66	51.26	6.64	55.3					
6H-5, 74–75	48.16	52.76	5.31	44.2	6.22	0.91	1.63	0.15	5.17
6H-6, 74–75	49.66	54.26	7.27	60.6					
6H-7, 20–21	50.62	55.22	6.57	54.7					
7H-1, 74–75	51.64	56.89	6.14	51.2	7.05	0.91	1.87	0.13	5.87
7H-2, 74–75	53.14	58.39	7.15	59.6					
7H-3, 74–75	54.64	59.89	3.98	33.1					
7H-4, 74–75	56.14	61.39	7.11	59.2					
7H-5, 74–75	57.64	62.89	6.54	54.5	7.67	1.13	2.49	0.16	5.99
7H-6, 74–75	59.15	64.40	5.19	43.2					
7H-7, 20–21	60.12	65.37	6.74	56.1					
8H-1, 74–75	61.14	67.09	5.85	48.8	7.15	1.30	2.54	0.17	6.56
8H-2, 74–75	62.65	68.60	7.16	59.6					
8H-3, 74–75	64.16	70.11	6.53	54.4					
8H-4, 74–75	65.68	71.63	7.16	59.6					
8H-5, 74–75	67.19	73.14	6.96	58.0	8.24	1.28	3.05	0.17	6.50
8H-6, 74–75	68.70	74.65	6.75	56.2					
9H-1, 74–75	70.64	77.94	5.89	49.1	7.69	1.80	3.53	0.22	7.08
9H-2, 74–75	72.15	79.45	6.10	50.8					
9H-3, 74–75	73.67	80.97	6.79	56.6					
9H-4, 74–75	75.17	82.47	6.20	51.7					
9H-5, 74–75	76.69	83.99	6.26	52.2	7.69	1.43	2.99	0.18	6.81
9H-6, 74–75	78.19	85.49	5.74	47.8					
9H-7, 20–21	79.16	86.46	6.21	51.7					
10H-1, 74–75	80.14	87.94	4.98	41.5	9.40	4.42	7.55	0.31	12.07
10H-2, 74–75	81.65	89.45	5.02	41.8					
10H-3, 74–75	83.15	90.95	3.77	31.4					
10H-4, 74–75	84.67	92.47	3.80	31.6					
10H-5, 74–75	86.18	93.98	5.57	46.4	8.10	2.53	4.73	0.27	8.01

Table T15 (continued).

Core, section, interval (cm)	Depth (mbsf)	Depth (mcd)	IC (wt%)	$CaCO_3$ (wt%)	TC (wt%)	TOC (wt%)	TOC CFB (wt%)	TN (wt%)	TOC/TN (atomic)
10H-6, 74–75	87.70	95.50	5.52	45.9					
10H-7, 20–21	88.67	96.47	5.58	46.5					
11H-1, 74–75	89.64	98.54	4.55	37.9	7.91	3.36	5.40	0.32	9.11
11H-2, 74–75	91.15	100.05	4.31	35.9					
11H-3, 74–75	92.66	101.56	4.40	36.7					
11H-4, 74–75	94.17	103.07	4.56	38.0					
11H-5, 74–75	95.68	104.58	5.46	45.5	7.98	2.52	4.63	0.21	10.20
11H-6, 74–75	97.19	106.09	6.31	52.6					
12H-1, 74–75	99.14	108.94	5.25	43.7	8.00	2.75	4.89	0.23	10.17
12H-2, 74–75	100.65	110.45	6.07	50.6					
12H-3, 74–75	102.16	111.96	5.58	46.5					
12H-4, 74–75	103.67	113.47	5.25	43.7					
12H-5, 74–75	105.19	114.99	5.45	45.4	7.54	2.09	3.82	0.19	9.52
12H-6, 74–75	106.71	116.51	7.56	63.0					
13H-1, 74–75	108.64	119.44	7.11	59.2	9.59	2.48	6.09	0.20	10.92
13H-3, 74–75	111.68	122.48	6.82	56.8					
13H-5, 74–75	114.69	125.49	6.75	56.3	8.83	2.08	4.76	0.18	9.91
14H-1, 74–75	118.14	129.49	7.54	62.8	8.53	0.99	2.65	0.15	5.75
14H-3, 74–75	121.17	132.52	7.39	61.6					
14H-5, 74–75	124.21	135.56	6.26	52.2	7.89	1.63	3.40	0.19	7.25
15H-1, 74–75	127.64	139.79	6.17	51.4	8.34	2.17	4.46	0.25	7.37
15H-3, 74–75	130.67	142.82	6.29	52.4					
15H-5, 74–75	133.69	145.84	7.41	61.7	8.89	1.48	3.88	0.17	7.31
16H-1, 74–75	137.14	149.94	6.40	53.3	8.08	1.68	3.59	0.20	7.11
16H-3, 74–75	140.17	152.97	7.33	61.1					
16H-5, 74–75	143.19	155.99	6.45	53.7	8.42	1.97	4.27	0.25	6.66
17H-1, 74–75	146.64	159.69	6.67	55.6	7.92	1.25	2.82	0.12	8.67
17H-3, 74–75	149.66	162.71	6.34	52.8					
17H-5, 74–75	152.70	165.75	6.45	53.8	7.96	1.51	3.26	0.19	6.88
18H-1, 74–75	156.14	171.14	5.22	43.5	8.16	2.94	5.20	0.22	11.30
18H-3, 74–75	159.16	174.16	6.88	57.3					
18H-5, 74–75	162.19	177.19	6.76	56.3	8.63	1.87	4.27	0.16	10.05
19H-1, 74–75	165.64	179.94	5.78	48.2	8.09	2.31	4.47	0.19	10.28
19H-3, 74–75	168.67	182.97	6.31	52.5					
19H-5, 74–75	171.70	186.00	6.79	56.6	8.55	1.76	4.06	0.16	9.50
20X-1, 74–75	175.14	190.30	6.22	51.8	8.18	1.96	4.08	0.17	9.96
20X-3, 74–75	178.16	193.32	6.04	50.3					
20X-5, 74–75	181.17	196.33	4.75	39.5	6.67	1.92	3.18	0.16	10.04
21X-1, 74–75	179.94	195.96	5.02	41.8	7.03	2.01	3.46	0.19	9.18
21X-3, 74–75	182.97	198.99	6.63	55.2					
21X-5, 74–75	186.00	202.02	4.20	35.0	6.42	2.22	3.42	0.22	8.78
22X-1, 74–75	189.64	206.52	6.04	50.3	7.68	1.64	3.29	0.16	8.60
22X-3, 74–75	192.66	209.54	5.37	44.7					
22X-5, 74–75	195.68	212.56	6.65	55.4	8.77	2.12	4.75	0.19	9.76
23X-1, 74–75	199.34	217.08	6.01	50.1	8.00	1.99	3.98	0.19	8.97
23X-5, 74–75	205.39	223.13	7.55	62.9	8.93	1.38	3.73	0.14	8.79
24X-1, 74–75	209.04	227.64	6.80	56.7	8.38	1.58	3.65	0.15	9.36
24X-3, 74–75	212.04	230.64	8.80	73.3					
24X-5, 74–75	215.04	233.64	6.63	55.3	8.37	1.74	3.89	0.20	7.54
25X-1, 74–75	218.34	237.80	6.61	55.1	9.18	2.57	5.73	0.22	10.12
25X-3, 74–75	221.24	240.70	7.50	62.5					
25X-5, 74–75	224.26	243.72	6.76	56.3	7.97	1.21	2.76	0.12	8.48
26X-1, 74–75	227.94	248.26	6.73	56.1	8.49	1.76	4.01	0.15	9.87
26X-3, 74–75	230.95	251.27	6.96	58.0					
26X-5, 74–75	233.96	254.28	7.39	61.5	8.57	1.18	3.08	0.08	13.45
27X-1, 74–75	237.24	258.42	7.70	64.1	9.51	1.81	5.04	0.15	10.40
27X-3, 74–75	240.25	261.43	7.78	64.8					
27X-5, 74–75	243.25	264.43	7.73	64.4	8.97	1.24	3.47	0.10	10.50
28X-1, 74–75	246.84	268.88	8.18	68.2	9.29	1.11	3.49	0.16	6.15
28X-3, 74–75	249.85	271.89	7.56	62.9					
28X-5, 74–75	252.86	274.90	7.30	60.8	9.03	1.73	4.42	0.20	7.35
29X-1, 74–75	256.44	279.34	7.43	61.9	9.07	1.64	4.29	0.15	9.55
29X-3, 74–75	259.44	282.34	8.33	69.4					
29X-5, 74–75	262.46	285.36	8.19	68.2	9.29	1.10	3.46	0.11	8.75
30X-1, 74–75	266.04	289.80	4.06	33.8	4.75	0.69	1.04	0.07	8.34
30X-3, 74–75	269.04	292.80	7.17	59.8					
30X-5, 74–75	272.04	295.80	8.08	67.3					
31X-1, 74–75	275.74	300.36	8.59	71.5					
31X-3, 74–75	278.74	303.36	7.42	61.8					

Table T15 (continued).

Core, section, interval (cm)	Depth (mbsf)	Depth (mcd)	IC (wt%)	$CaCO_3$ (wt%)	TC (wt%)	TOC (wt%)	TOC CFB (wt%)	TN (wt%)	TOC/TN (atomic)
31X-5, 74–75	281.74	306.36	7.47	62.2	9.24	1.77	4.67	0.16	9.40
32X-1, 74–75	285.34	310.82	7.34	61.1					
32X-3, 74–75	288.36	313.84	7.20	60.0					
32X-5, 74–75	291.36	316.84	7.03	58.6	8.28	1.25	3.01	0.06	17.67
33X-1, 74–75	295.04	321.38	8.91	74.2					
33X-3, 74–75	298.05	324.39	8.61	71.8					
33X-5, 74–75	301.04	327.38	8.70	72.5	12.18	3.48	12.66	0.10	31.22
34X-1, 74–75	304.64	331.84	8.70	72.5					
34X-3, 74–75	307.65	334.85	7.57	63.1					
34X-5, 74–75	310.66	337.86	9.52	79.3	10.33	0.81	3.92	0.05	12.81
35X-1, 74–75	314.24	342.30	6.95	57.9					
35X-3, 74–75	317.26	345.32	7.65	63.7	8.81	1.16	3.18	0.14	6.88
36X-1, 74–75	323.94	352.86	8.70	72.5					
36X-3, 74–75	326.96	355.88	8.78	73.1					
36X-5, 74–75	329.97	358.89	8.64	72.0	10.12	1.48	5.29	0.14	9.27
37X-1, 74–75	333.54	363.32	8.64	72.0					
37X-3, 74–75	336.56	366.34	8.64	72.0					
37X-5, 74–75	339.57	369.35	5.39	44.9	6.11	0.72	1.30	0.14	4.27
38X-1, 74–75	343.14	373.78	9.87	82.2					
38X-3, 74–75	346.16	376.80	10.05	83.7					
38X-5, 74–75	349.15	379.79	9.57	79.8	10.40	0.83	4.11	0.13	5.62
39X-1, 74–75	352.74	384.24	8.80	73.3					
39X-3, 74–75	355.76	387.26	9.17	76.4					
39X-5, 74–75	358.76	390.26	8.88	74.0	9.68	0.80	3.08	0.05	13.87
40X-1, 74–75	362.44	394.80	9.09	75.7					
40X-5, 74–75	368.48	400.84	9.13	76.1	10.08	0.95	3.97	0.04	18.53
41X-1, 74–75	372.04	405.26	8.85	73.8					
41X-3, 74–75	375.06	408.28	9.15	76.2	10.65	1.50	6.29	0.15	8.55
42X-1, 74–75	381.74	415.82	8.84	73.7					
42X-5, 74–75	387.77	421.85	7.78	64.8	8.78	1.00	2.83	0.14	6.06
43X-1, 74–75	391.34	426.28	8.59	71.6					
43X-5, 74–75	397.36	432.30	8.92	74.3	9.87	0.95	3.69	0.13	6.35
44X-1, 74–75	400.94	436.74	7.44	62.0					
44X-5, 74–75	406.97	442.77	8.52	71.0	9.69	1.17	4.02	0.09	11.41
45X-1, 74–75	410.64	447.30	9.02	75.1					
45X-5, 74–75	416.70	453.36	8.50	70.8	9.54	1.04	3.54	0.07	13.12
46X-1, 74–75	420.14	457.66	8.27	68.9					
46X-5, 74–75	426.16	463.68	7.65	63.7	9.17	1.52	4.18	0.16	8.23
47X-1, 74–75	429.74	468.12	9.23	76.9					
47X-5, 74–75	435.77	474.15	9.48	79.0	10.08	0.60	2.87	0.03	14.94
48X-1, 74–75	439.44	478.68	9.27	77.2					
48X-5, 74–75	445.48	484.72	9.63	80.2	10.34	0.71	3.60	0.04	14.74
49X-1, 74–75	449.04	489.14	9.30	77.5					
49X-5, 74–75	455.07	495.17	10.05	83.8	10.64	0.59	3.63	0.03	17.38
50X-1, 74–75	458.74	499.70	8.59	71.5					
50X-5, 74–75	464.77	505.73	7.46	62.2	8.04	0.58	1.53	0.03	15.73
51X-1, 74–75	468.34	510.16	9.79	81.6					
51X-5, 74–75	474.38	516.20	9.36	77.9	9.88	0.52	2.37	0.03	13.50
52X-1, 74–75	477.94	520.62	8.60	71.6					
52X-5, 74–75	483.98	526.66	9.68	80.6	9.97	0.29	1.50	0.03	7.55
53X-1, 74–75	487.24	530.78	9.47	78.9					
53X-3, 74–75	490.25	533.79	9.79	81.6	10.22	0.43	2.31	0.04	10.20
54X-1, 74–75	496.84	541.24	7.52	62.6					
54X-5, 74–75	502.89	547.29	7.76	64.7	9.69	1.93	5.45	0.23	7.24
55X-1, 74–75	506.44	551.70	9.31	77.6					
55X-5, 20–21	511.38	556.64	10.39	86.6	12.59	2.20	16.35	0.22	8.77

Note: IC = inorganic carbon, TC = total carbon, TOC = total organic carbon, CFB = carbonate-free basis, TN = total nitrogen.

Table T16. Age-depth model, linear sedimentation rates, and mass accumulation rates, Site 1239.

Age (Ma)	Depth (mcd)	LSR (mcd/m.y.)	mcd growth factor	Corrected LSR (m/m.y.)	Dry density (g/cm^3)	$CaCO_3$ average concentration (wt%)	TOC average concentration (wt%)	Total MAR ($g/cm^2/k.y.$)	$CaCO_3$ MAR ($g/cm^2/k.y.$)	TOC MAR ($g/cm^2/k.y.$)	Noncarbonate MAR ($g/cm^2/k.y.$)
0.0	0.0										
1.0	46.4	46	1.08	43	0.77	53.8	0.48	3.3	1.8	0.016	1.5
2.0	108.2	62	1.08	57	0.76	49.5	0.57	4.3	2.1	0.025	2.2
3.0	193.6	85	1.08	79	0.77	53.7	1.18	6.1	3.2	0.071	2.8
4.0	305.6	112	1.08	104	0.81	57.7	1.01	8.4	4.8	0.085	3.5
5.0	384.1	79	1.08	73	0.89	69.3	0.49	6.5	4.5	0.032	2.0
6.0	464.3	80	1.08	74	0.87	71.8	0.53	6.5	4.6	0.034	1.8
7.0	509.5	45	1.08	42	0.99	76.0	0.31	4.1	3.1	0.013	1.0
8.0	523.2	14	1.08	13	1.06	79.8	0.26	1.3	1.1	0.004	0.3

Notes: LSR = linear sedimentation rate, MAR = mass accumulation rate. TOC = total organic carbon. This table is also available in **ASCII**.